



Non-Reciprocal Optical Amplification and Phase Shifts in a Nanofiber-Based Atom-Light Interface and a Precise Lifetime Measurement of the Cesium $5D_{5/2}$ State

D i s s e r t a t i o n

zur Erlangung des akademischen Grades

d o c t o r r e r u m n a t u r a l i u m
(Dr. rer. nat.)

im Fach Physik

eingereicht an der
Mathematisch-Naturwissenschaftlichen Fakultät I
der Humboldt-Universität zu Berlin

von

Dipl.-Ing. Sebastian Pucher

Präsident der Humboldt-Universität zu Berlin:
Prof. Dr. Peter Frensch

Dekanin der Mathematisch-Naturwissenschaftlichen Fakultät:
Prof. Dr. Caren Tischendorf

Gutachter/innen:
Prof. Arno Rauschenbeutel
Prof. Ruth Oulton
Prof. Chang-Ling Zou

Tag der mündlichen Prüfung: 26.09.2022

Abstract

Nanophotonic systems are a powerful platform for the study of light-matter interactions. In such systems, the common description of an electromagnetic wave as a wave that is transversely polarized with respect to its propagation direction breaks down. This is due to the tight confinement of the guided light fields, which leads to a longitudinal component of the electromagnetic fields. In this thesis, we use this in conjunction with different coupling strengths of cesium atoms to σ^- and σ^+ polarized light to provide proof-of-principle demonstrations of novel non-reciprocal optical devices. In an additional research project, we also contribute to the fundamental understanding of atoms by precisely measuring the lifetime of an excited cesium state.

Typically, one requires either the magneto-optical effect, a temporal modulation, or an optical nonlinearity to break reciprocity. By contrast, the non-reciprocal effect in our system originates from the propagation direction-dependent local polarization of a nanofiber-guided mode in conjunction with polarization-dependent atom-light coupling. In the first part of this thesis, we demonstrate non-reciprocal amplification of fiber-guided light using Raman gain provided by spin-polarized cesium atoms that are coupled to the nanofiber waist of a tapered fiber section. We show that our novel mechanism does not require an external magnetic field and that it allows us to fully control the direction of amplification via the atomic spin state.

Moreover, we use the chiral light-matter interaction in our system to implement a non-reciprocal antisymmetric optical phase shifter. These results contribute to establishing a new class of spin-controlled, non-reciprocal integrated optical devices and may simplify the construction of complex optical networks. Moreover, suitable solid-state-based quantum emitters provided, our schemes of amplification and phase shifting could be readily implemented in photonic integrated circuits.

Finally, in the last part of this thesis, we measure the lifetime of the cesium $5D_{5/2}$ state in free space. We find a lifetime of 1353(5) ns, in agreement with a recent theoretical prediction. Our measurement contributes to resolving a long-standing disagreement between several experimental and theoretical results.

Zusammenfassung

Nanophotonische Systeme sind eine leistungsfähige Plattform für die Untersuchung von Licht-Materie-Wechselwirkungen. In solchen Systemen bricht die übliche Beschreibung einer elektromagnetischen Welle als eine Welle, die in Bezug auf ihre Ausbreitungsrichtung transversal polarisiert ist, zusammen. Dies ist auf die Einengung der geführten Lichtfelder zurückzuführen, welche zu einer longitudinalen Komponente der elektromagnetischen Felder führt. In dieser Arbeit nutzen wir dies in Verbindung mit unterschiedlichen Kopplungsstärken von Cäsiumatomen an σ^- und σ^+ polarisiertes Licht, um das Prinzip neuartiger nicht-reziproker optischer Bauelemente zu demonstrieren. In einem weiteren Forschungsprojekt tragen wir zum grundlegenden Verständnis von Atomen bei, indem wir die Lebensdauer eines angeregten Cäsiumzustands präzise messen.

Normalerweise benötigt man entweder den magneto-optischen Effekt, eine zeitliche Modulation oder eine optische Nichtlinearität, um Reziprozität zu brechen. Im Gegensatz dazu entsteht der nicht-reziproke Effekt in unserem System durch die ausbreitungsrichtungsabhängige lokale Polarisation einer nanofasergeführten Mode in Verbindung mit polarisationsabhängiger Atom-Licht-Kopplung. Im ersten Teil dieser Arbeit demonstrieren wir die nicht-reziproke Verstärkung von fasergeführtem Licht mit Hilfe von Raman-Verstärkung durch spinpolarisierte Cäsiumatome, die an die Nanofasertaille eines verjüngten Faserabschnitts gekoppelt sind. Wir zeigen, dass unser neuartiger Mechanismus kein externes Magnetfeld benötigt und dass wir die Richtung der Verstärkung vollständig über den atomaren Spinzustand kontrollieren können.

Darüber hinaus nutzen wir die chirale Licht-Materie-Wechselwirkung in unserem System, um einen nicht-reziproken antisymmetrischen optischen Phasenschieber zu realisieren. Diese Ergebnisse tragen zur Etablierung einer neuen Klasse von spin-gesteuerten, nicht-reziproken integrierten optischen Bauelementen bei und können den Aufbau komplexer optischer Netzwerke vereinfachen. Darüber hinaus könnten unsere Verstärkungs- und Phasenverschiebungsschemata mit Hilfe geeigneter Quantenemitter

auf Festkörperbasis ohne weiteres in integrierten photonischen Schaltungen implementiert werden.

Im letzten Teil dieser Arbeit messen wir die Lebensdauer des Cäsium $5D_{5/2}$ Zustands im freien Raum. Wir finden eine Lebensdauer von $1353(5)$ ns, die mit einer aktuellen theoretischen Vorhersage übereinstimmt. Unsere Messung trägt dazu bei, eine seit langem bestehende Unstimmigkeit zwischen verschiedenen experimentellen und theoretischen Ergebnissen zu beseitigen.

Contents

Introduction	1
1 Atomic Spin-Controlled Non-Reciprocal Amplification of Fiber-Guided Light	5
1.1 Introduction	5
1.2 Working Principle	6
1.3 Theoretical Description	7
1.3.1 Gain Definitions	7
1.3.2 Analytical Equations and Calculations	9
1.3.3 Numerical Calculations of a Three-Level Λ -Type System	14
2 Experimental Setup for the Amplification Measurements	21
2.1 Nanofiber-Based Dipole Trap	21
2.2 Preparation of the Atomic Ensemble	24
2.3 Non-Reciprocal Amplification Setup	27
2.4 Beam Path of the Signal Laser	29
2.5 Data Analysis	31
2.6 Calibration of the Pump Field	32
2.6.1 Intensity and Polarisation Distribution of the Pump Laser Beam	32
2.6.2 EIT and Autler-Townes Splitting	35
2.6.3 One-photon Detuning	39
2.7 Signal Field Rabi Frequency	42
2.7.1 Theoretical Calculations	42
2.7.2 Experimental Exploration Using EIT	45
3 Experimental Demonstration of Non-Reciprocal Amplification	47
3.1 Non-Reciprocal Amplification	47
3.2 Spontaneous Raman Scattering of the Pump Field	50

3.3	Signal Transmission Dynamics	52
3.4	Reconfiguration of the Amplifier	53
3.5	Frequency Dependency of the Signal Transmission	54
3.5.1	Steady-State Absorption	54
3.5.2	Gain Spectrum and Amplifier Bandwidth	56
3.6	Simultaneously Probing from Both Directions	57
3.7	Scaling of the Gain with the Number of Atoms	58
3.7.1	Linear Regime	58
3.7.2	Demonstration of Superlinear Scaling	59
3.8	Measurements of Gains up to 10	61
4	Magnetic-Field Free Operation of the Non-Reciprocal Amplifier	63
4.1	Experimental Setup and Method	63
4.1.1	Atomic Level Scheme	63
4.1.2	Calculation of the Tensor Light Shift	65
4.1.3	Experimental Setup	68
4.1.4	Experimental Sequence	70
4.2	Experimental Results	70
4.2.1	Transmission Spectrum	70
4.2.2	Demonstration of Magnetic-Field Free Non-Reciprocal Amplification	72
4.2.3	Evolution of the Signal Transmission	74
4.3	Outlook	75
5	Antisymmetric Non-Reciprocal Phase Shifts based on Chiral Light-Matter Coupling	77
5.1	Introduction and Motivation	77
5.2	Experimental Setup and Method	79
5.2.1	Atomic Structure	79
5.2.2	Phase Shift around an Atomic Resonance	81
5.2.3	Experimental Setup	82
5.2.4	Experimental Sequence	85
5.3	Experimental Demonstration of Non-Reciprocal Phase Shifts	86
5.4	Summary and Outlook	88

6	Lifetime Measurement of the Cesium $5D_{5/2}$ State	91
6.1	Introduction and Motivation	92
6.2	Experimental Method and Setup	93
6.2.1	Atomic Level Structure	94
6.2.2	Decay Model of a Three-Level System	96
6.2.3	Laser Setup	97
6.2.4	Fluorescence Setup	99
6.2.5	Experimental Sequence	100
6.3	Results	101
6.3.1	Fit Method	102
6.3.2	Goodness of the Fit	102
6.3.3	Fit Results and Statistical Fluctuations	103
6.4	Systematic Errors	105
6.4.1	Effect of Atomic Collisions	105
6.4.2	Truncation Error	108
6.5	Final Lifetime with Total Error Budget	109
6.6	Summary and Outlook	110
7	Conclusion and Outlook	113
	Appendices	117
A	Derivation of the Frequency Dependence of the Phase Shift	119
B	Theoretical Aspects of Lifetimes	123
C	Spectrally Resolved Fluorescence Measurement	125
D	Other Systematic Errors of the Lifetime Measurement	127
E	Open Access to the Experimental Data	133
	Bibliography	139

Introduction

The interactions between light and matter play a fundamental role in science and technology. The study of these interactions has already led to numerous scientific advances. Nowadays, an open challenge is to make the light-matter interaction even for single, point-like emitters directional or non-reciprocal and, based on that, to construct useful devices. Here, we experimentally study non-reciprocal effects based on nanophotonic atom-light coupling.

In the past few centuries, the investigation of atoms has undergone tremendous development, and the structure of atoms has become better and better understood. The first atomic models go back to Democritus (about 400 BC), who postulated the existence of various solid, indivisible particles, which in different combinations form the known substances. In the year 1808, this idea was taken up by J. Dalton, who stated that atoms are distinguished by their masses [1]. Soon after the discovery of the electron, the Dalton model was replaced by the plum pudding model. First proposed by J. J. Thomson in 1904, it became the widely accepted atomic theory [2]. It postulates that the atom is made out of evenly distributed, positively charged mass in which the negatively charged electrons move. However, in 1911, E. Rutherford could experimentally show that the atom consists of a small positively charged nucleus surrounded by negatively charged electrons [3]. Later, this model was improved by N. Bohr, who postulated that the electrons orbit around the nucleus [4]. It successfully described many properties of atoms, in particular, the experimentally observed spectral emission lines of atomic hydrogen. However, the model breaks down for non-hydrogen-like atoms and could not explain the spectral emission line shapes as well as their fine structure. Eventually, the theory was replaced by quantum mechanical models, where the electrons are not on well-defined orbits but in an electron cloud that is extended in space. This idea was pioneered by L. de Broglie, who postulated in 1924 that matter has wave properties [5]. This inspired E. Schrödinger to describe an electron as a wave function instead of a point particle [6]. The resulting atomic orbitals describe the location and wave-like behavior of an electron in an atom.

The quantum mechanical description of the atom has been and is still constantly further improving. In the last few decades, alkali metal atoms turned out to be an ideal source for our fundamental understanding of nature. They feature a simple electron structure because the outermost electron is in an s-orbital [7]. This makes them a perfect test bench where measurements and calculations have reached the highest precision [8]. Alkali metal atoms also enjoy high popularity in cold atom physics. For example, the first magneto-optical trap (MOT) was experimentally demonstrated with sodium atoms [9]. Cold atoms are often used to study light-matter interaction in the quantum regime [10]. Mastering this, powerful platforms can be constructed for quantum simulations and quantum computation [11–14].

Nowadays, science and technology are striving to make light-matter devices smaller and more portable. In this vein, the field of nanophotonics is receiving a lot of attention. Here, the behavior of light is studied on the subwavelength scale, and the interaction of nanometer-scale objects with light is investigated. Recently, many nanophotonics-based cold atom systems were constructed, which often use alkali metals [15–22]. In such subwavelength-scale optical systems, the light fields are strongly confined [23]. Due to the strong confinement, the light fields exhibit strong transversal field gradients on the order of the wavelength. Therefore, a longitudinal electric field component can arise [24]. This leads to a propagation direction-dependent local polarization of the light field known as spin-momentum locking of light [25–27]. Recently, this effect was experimentally studied in various systems, e.g., with a plane dielectric interface [28, 29], a plane metasurface [30], as well as in free space [31–33]. In conjunction with polarization-dependent light-matter coupling, spin-momentum locking of light enables directional emission in a waveguide [34–53] as well as chiral interfaces [54–58]. Such interfaces have different effects on the light depending on the direction in which the light propagates through them. In general, the propagation through the interface is called non-reciprocal if the field created by a source at an observation point is not the same compared to the case when the source and the observation point are interchanged [59].

The first known theoretical works on non-reciprocity were performed for light waves in 1849 by G. G. Stokes [60] and in 1856 by H. v. Helmholtz [61]. This inspired H. A. Lorentz to postulate his famous electromagnetic reciprocity theorem in 1896 [62]. It is formulated with current densities that create electric fields. Specifically, the theorem states that the relationship between an oscillating current and the resulting electric field is unchanged if one interchanges the points where the current flows and where the field is measured. To break the Lorentz reciprocity is one of the fundamental concepts of optics [59, 62–65]. The textbook methods for achieving this non-reciprocity

are magneto-optics, temporal modulation, or optical nonlinearities [59, 66]. In contrast, recently, non-reciprocity was studied with the propagation direction-dependent local polarization of confined light in conjunction with polarization-dependent atom-light coupling. A new class of such nanophotonic non-reciprocal optical devices was implemented [54] that comprises, so far, an optical isolator [67] and a circulator [68]. Moreover, in free space, atomic spin-controlled isolation has been presented [69, 70]. However, optical non-reciprocal amplifiers and phase shifters based on this principle are so far missing.

In this thesis, we will use a nanofiber-based cold atoms system to investigate non-reciprocal effects. These systems offer high coupling strengths, which are beneficial when implementing light-matter interfaces for photonic quantum technologies [21, 71, 72]. The atoms can be trapped next to the nanofiber to improve control over the system. This can be realized with two-color dipole traps, as first proposed in 2004 by Fam Le Kien *et al.* [73]. The first experimental implementation was demonstrated by E. Vetsch *et al.* in 2010 [15]. This led to much attention, and, nowadays, various setups which trap atoms close to nanofibers are in operation [74–78]. These systems were used to perform several novel experiments. For example, quantum state-controlled directional spontaneous emission was detected [79], ultra-strong spin-motion coupling was observed [80], the storage of fiber-guided light in an atomic ensemble was experimentally demonstrated [81, 82], and non-reciprocal effects were investigated and used to construct directional devices [67, 83]. Moreover, collective light-matter interaction can be readily studied experimentally [84]. These effects comprise the coherent backscattering of light [85, 86], a single collective excitation of the atomic array [87], and collectively enhanced nonlinearities that results in antibunching [88], squeezing of the transmitted light field [89], and super- and subradiance [90–92].

The thesis is organized as follows. First, we discuss the principles of our implementation of non-reciprocal amplification of light using Raman gain. The non-reciprocal response originates from spin-polarized atoms chirally coupled to a nanophotonic waveguide. Here, we use a novel method to break reciprocity [59]. As discussed, the non-reciprocal response is based on the propagation direction-dependent local polarization of the nanofiber-guided light in conjunction with polarization-dependent atom-light coupling. In the second chapter, we will present our experimental setup and corresponding calibration measurements. We experimentally demonstrate non-reciprocal amplification in our system in the third chapter. We analyze important features of the amplifier, such as the maximal gain, the bandwidth, and the noise originating from the

spontaneous scattering of the laser fields. In the fourth chapter, we show that our system remains non-reciprocal even without an externally applied magnetic field and that the atomic spin state is controlling the direction of amplification. In the fifth chapter, we use the chiral light-matter interaction in our system to implement a non-reciprocal antisymmetric phase shift of the guided light field. In contrast to the longitudinal Faraday effect [93], we will show that the non-reciprocal phase shift is based on linear birefringence rather than circular birefringence. Finally, in the last chapter, we will present the results of a separate research project and make a contribution to the fundamental understanding of atoms by measuring the lifetime of the cesium $5D_{5/2}$ state in free space. The results are consistent with a recent theoretical prediction and help resolving a long-standing disagreement between several experimental and theoretical works.

Chapter 1

Atomic Spin-Controlled Non-Reciprocal Amplification of Fiber-Guided Light

In this and the following three chapters, we demonstrate non-reciprocal amplification of light using Raman gain. The non-reciprocal response originates from spin-polarized atoms chirally coupled to an optical nanofiber. We show that in this novel mechanism, the direction of amplification is fully controlled via the atomic spin state. The discussion in these chapters closely follows the published manuscript [83].

1.1 Introduction

Non-reciprocal devices are of crucial practical value and indispensable in optical technologies. They treat light differently depending on the propagation direction of the light in the device [59, 64, 65, 94], thereby enabling, e.g., optical diodes and circulators. The established ways to break reciprocity are based on the magneto-optical effect [66], temporal modulation [95, 96], or optical nonlinearities [59, 97, 98]. Recently, a new way to realize non-reciprocity was discovered. Here, the internal spin state of quantum emitters that are coupled to spin-momentum locked nanophotonic modes [25] enable direction-dependent effects [54]. A novel class of non-reciprocal elements emerged that, by now, comprises experimental realizations of optical isolators [67, 69] and circulators [68]. However, a non-reciprocal amplifier is hitherto missing.

Amplification enables the detection of weak signals while ideally only adding a minimal amount of noise. Particularly, for non-reciprocal amplifiers, the optical gain

depends on the propagation direction of the light through the gain medium. Therefore, such amplifiers can protect the source from amplified optical feedback, an important feature when working with sensitive quantum systems [99]. Moreover, they simplify the construction of complex optical networks [100, 101].

Recently, several non-reciprocal optical amplifiers were experimentally realized. Various schemes were investigated that are based on Doppler shifts as well as far-detuned four-wave mixing processes in hot atomic vapors [102, 103], on optomechanical effects [104–107], and on stimulated Brillouin scattering in silicon [108, 109]. Also, non-reciprocal optical Raman amplifiers are of particular importance for technical applications [110]. In this context, non-reciprocal amplification using the propagation direction-dependent polarization overlap of Raman light fields guided in nanophotonic waveguides has been demonstrated [111]. On the theoretical side, non-reciprocal amplification via spin selective photon-phonon interactions enabled by stimulated Raman scattering was studied recently [112].

1.2 Working Principle

In this chapter, we experimentally demonstrate the non-reciprocal amplification of a fiber-guided laser field. We make use of laser-trapped, spin-polarized cesium atoms that are coupled to a mode of a nanophotonic waveguide. The waveguide is realized as a single-mode, tapered silica fiber with a nanofiber waist. We take advantage of the inherent link between the local polarization and the propagation direction of the guided light field [37, 79]. This effect is also known as spin-momentum locking, i.e., the spin and orbital angular momentum of the light properties become coupled with each other [25]. This enables a direction-dependent light-matter coupling that is also referred to as chiral coupling [39, 42, 54, 56, 113, 114]. When the guided-light field is quasi-linearly polarized [115], σ^- (σ^+) polarized cesium transitions couple to the forward (backward) propagating mode. Together with an external pump field, this allows us to address separate Λ -type atomic energy level schemes in a two-photon Raman configuration.

Recently, Λ systems coupled to spin-momentum locked evanescent fields were theoretically studied [39, 116–122]. We use such a system to realize a novel amplification scheme. By a suitable preparation of the atomic spin state, we arrange a population inversion such that Raman gain occurs for only one of the Λ -systems. We experimentally observe a directional gain for the guided field that is much larger in one direction

than in the opposite direction. We experimentally show that the direction in which amplification occurs can be controlled by flipping the spin-polarization of the atoms.

We demonstrate that no magnetic field is required for non-reciprocal operation. While such a field was necessary in previous works [67] to prevent spin depolarization due to, e.g., stray magnetic fields, here we achieve this via a suitable tensor light shift. In contrast to non-linear schemes, our scheme can handle signal fields that simultaneously propagate in both directions through the device, as we also show experimentally. Moreover, it does not involve temporal modulation induced, e.g., by an optical pump field that shares the same spatial mode as the signal field. Hence, our approach is qualitatively different from the textbook examples of non-reciprocal effects insofar as we control the direction of amplification via the spin state of nanofiber-coupled atoms.

1.3 Theoretical Description

In this section, we discuss the theory of our gain mechanism. First, we define the gain. Then, we study the transmission through an atomic ensemble analytically. Finally, we perform numerical calculations of the evolution of the transmission.

1.3.1 Gain Definitions

An optical amplifier is a device that increases the amplitude of an optical field. The input field is increased by a factor known as the amplifier gain. Around an atomic resonance, this gain can be defined with the power transmission coefficient [63, 123]

$$T(\delta) = \exp[g(\delta)d] , \tag{1.1}$$

where d is the total length of the interaction region, $\delta = \omega - \omega_{\text{at}}$ is the detuning of a laser with a frequency ω from the atomic resonance frequency ω_{at} , and $g(\delta)$ is the gain coefficient. A positive $g(\delta)$ leads to amplification and a negative $g(\delta)$ to attenuation of the input field. If $g(\delta) = 0$, the device is transparent and shows neither gain nor absorption.

The amplifier gain depends on multiple factors [94]. Apart from the gain coefficient, the noise and the bandwidth are important parameters in the following. In optical amplifiers that are based on stimulated emission, a fundamental source of noise is spontaneous emission. In contrast to stimulated emission, the spontaneously emitted light is usually broadband, emitted in many directions, and can have a different

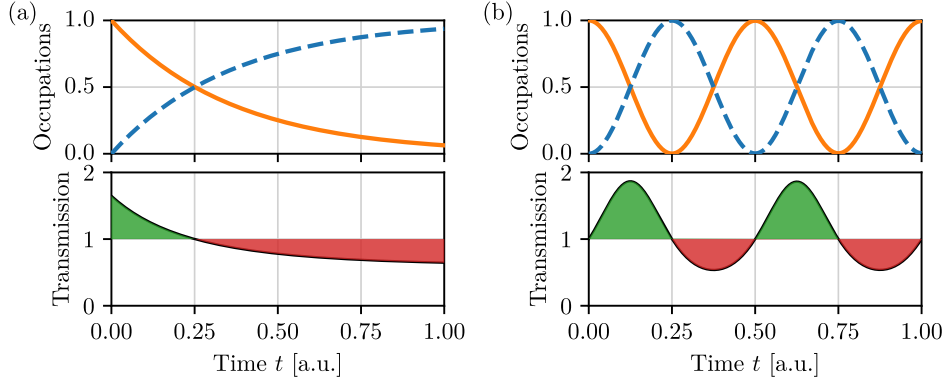


FIGURE 1.1: Illustration of the evolution of gain and attenuation in the incoherent and coherent regime. Upper panels: occupations in the ground state N_g (dashed blue line) and the excited state N_e (solid orange line). Lower panels: Power transmission of a light field interacting with the two-level system. We refer to a transmission over 1 as gain (green area) and below 1 as absorption or attenuation (red area). (a) In the incoherent regime, the gain coefficient and the transmission are proportional to the population inversion $N_e - N_g$. (b) In the coherent regime, Rabi oscillations occur. Stimulated emission leads to population transfer from $|e\rangle$ to $|g\rangle$, and as a result, the light field experiences gain. Conversely, while population is transferred from $|g\rangle$ to $|e\rangle$, the light field is attenuated. Here, the gain coefficient is proportional to \dot{N}_g . See text for the parameters of the simulations.

polarization than the input field [94]. Thus, it is possible to filter out some of the noise with, e.g., bandpass filters, apertures, and polarizers, but it is fundamentally impossible to filter the spontaneous emission completely. The bandwidth depends on an atomic transition, which has one well-defined resonance frequency and a Lorentzian lineshape, i.e., we do not take possible inhomogeneous broadening of the transition into account. Then, the amplifier bandwidth is determined by the linewidth of the transition.

We now discuss the gain for a medium that consists of atoms with the ground state $|g\rangle$ and the excited state $|e\rangle$. We study the interaction of this two-level system with a light field tuned on resonance with the $|g\rangle \rightarrow |e\rangle$ transition, i.e., $\delta = 0$. We distinguish two different regimes, the incoherent and the coherent regime (see Fig. 1.1). In the incoherent regime, the Rabi frequency Ω is much smaller than the decoherence rates. In the illustration in Fig. 1.1(a), we use a excited state population decay rate of

1.3. Theoretical Description

$\Gamma = 2\pi \times 0.441$ arb.unit and $\Omega \ll \Gamma$. In this regime, we can define the time-dependent on-resonance gain coefficient as [63, 123]

$$g_0(t) = N(t)\sigma_0 , \quad (1.2)$$

where σ_0 is the on-resonance transition cross-section and $N(t) = N_e(t) - N_g(t)$ is the time-dependent difference between the population number densities in $|e\rangle$ and $|g\rangle$. If $N_e > N_g$, a population inversion exists, and the medium can act as an amplifier. The responsible effect is stimulated emission, where an incident photon induces the transition of an atom from $|e\rangle$ to $|g\rangle$ under the emission of a stimulated photon. In an ensemble of atoms, the emitted photon can stimulate further emissions leading to an exponential increase of the output power with the length of the medium. However, when $N_e < N_g$, absorption occurs. We also note that there are no gain revivals as long as no repumping scheme is implemented.

In the coherent regime, the Rabi frequency is much larger than the decoherence rates. In Fig. 1.1(b), we use a Rabi frequency of $\Omega = 2\pi \times 2$ arb.unit and $\Omega \gg \Gamma$. We find Rabi oscillations of the population densities in $|g\rangle$ and $|e\rangle$. While population is transferred from $|e\rangle$ to $|g\rangle$, the light field is amplified via the stimulated emission of photons. In contrast, while population is transferred from $|g\rangle$ to $|e\rangle$, photons are absorbed and the light field is attenuated. Hence, the on-resonance gain coefficient is proportional to

$$g_0(t) \propto \dot{N}_g(t) , \quad (1.3)$$

where $\dot{N}_g(t)$ is the time derivative of the population in $|g\rangle$. In this coherent regime, gain and attenuation thus vary periodically with time, with a period given by

$$T = 2\pi/\Omega , \quad (1.4)$$

where Ω is the Rabi frequency.

1.3.2 Analytical Equations and Calculations

We consider a dielectric medium where the induced dielectric polarization density \mathbf{P} is linearly related to the applied electric field \mathbf{E} . The average induced polarization can be found with the expectation value of the dipole moments [124]

$$\mathbf{P}(\mathbf{r}) = \chi\epsilon_0\mathbf{E}(\mathbf{r}) = \frac{N}{V} \langle \hat{d} \rangle = \frac{N}{V} \text{Tr}(\hat{\rho}\hat{d}) , \quad (1.5)$$

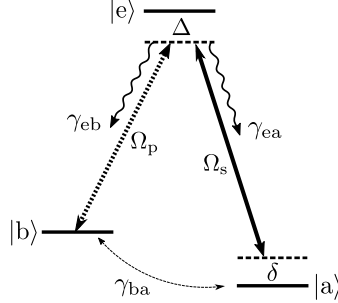


FIGURE 1.2: Energy level scheme considered in our theoretical calculations. Our theory is based on a three-level Λ -type system. The signal and pump laser fields couple the ground states $|a\rangle$ and $|b\rangle$ with the excited state $|e\rangle$, respectively. See main text for details.

where χ is the electric susceptibility, ϵ_0 is the electric permittivity of free space, $\frac{N}{V}$ is the atom number density, $\hat{\rho}$ is the density operator, and \hat{d} is the dipole operator. In matrix representation, \hat{d} only consists of off-diagonal dipole moments, i.e., $\mathbf{d}_{mm}(\mathbf{r}) = 0$ for $m = n$. Hence, the susceptibility depends on the off-diagonal elements of the density matrix, i.e., the coherences.

Here, we discuss the three-level Λ -type energy level scheme illustrated in Fig. 1.2. We term the excited state $|e\rangle$. Atoms in this state can decay to the two ground states $|a\rangle$ and $|b\rangle$ with population decay rates γ_{ea} and γ_{eb} , respectively. There are no dipole-allowed transitions between the two ground states. We assume a ground-state decoherence rate γ_{ab} and couple the system to two laser fields. The signal field couples $|a\rangle$ with $|e\rangle$, and the pump field couples $|b\rangle$ with $|e\rangle$. The lasers have a one-photon detuning Δ from $|e\rangle$ and a two-photon detuning δ from $|a\rangle$ (see Fig. 1.2). We assume that the signal field propagates along the y -axis and the pump field along the x -axis. The respective electric field components are

$$\mathbf{E}_s(\omega_s, \mathbf{k}_s) = \left[\mathbf{A}_s e^{i(\omega_s t - \mathbf{k}_s \mathbf{r})} + \text{c.c.} \right] / 2, \quad (1.6)$$

$$\mathbf{E}_p(\omega_p, \mathbf{k}_p) = \left[\mathbf{A}_p e^{i(\omega_p t - \mathbf{k}_p \mathbf{r})} + \text{c.c.} \right] / 2, \quad (1.7)$$

where ω_s (ω_p) is the frequency of the signal (pump) field. Here, the wave vector of the signal field is $\mathbf{k}_s = (0, k_s, 0)$, and the wave vector of the pump field is $\mathbf{k}_p = (k_p, 0, 0)$.

1.3. Theoretical Description

The corresponding Rabi frequencies are

$$\Omega_s = \frac{\mathbf{E}_s \cdot \mathbf{d}_{ae}}{\hbar} , \quad (1.8)$$

$$\Omega_p = \frac{\mathbf{E}_p \cdot \mathbf{d}_{be}}{\hbar} , \quad (1.9)$$

where \mathbf{d}_{ae} (\mathbf{d}_{be}) is the dipole moment of the $|a\rangle \rightarrow |e\rangle$ ($|b\rangle \rightarrow |e\rangle$) transition. The Rabi frequencies are defined for a laser in resonance with a two-level system. When there is no decoherence or spontaneous decay, they describe the frequency of the population oscillation between the ground state and the excited state. If, however, the light field is detuned from the excited state, Rabi flopping will occur at the generalized Rabi frequency

$$\tilde{\Omega}_{s(p)} = \sqrt{\Omega_{s(p)}^2 + \Delta^2} . \quad (1.10)$$

Since $\text{Tr}(\hat{\rho}\hat{d}) = 2d_{ae}\rho_{ae}$ [124], we can use Eq. 1.8 to replace \mathbf{E} in Eq. 1.5 and find [125]

$$\chi_{ae} = 2 \frac{N}{V} \frac{d_{ae}^2}{\Omega_s \hbar \epsilon_0} \rho_{ae} . \quad (1.11)$$

It is not straightforward to define an atom number density in our system. However, we can define the on-resonance optical depth for a cycling transition [7]

$$\text{OD}_0 = \sigma_0 \frac{N}{V} L = \frac{3\lambda^2}{2\pi} \frac{N}{V} L = \frac{N}{V} \frac{2d_0^2 k_s L}{\hbar \epsilon_0 \Gamma_r} , \quad (1.12)$$

where L is the length of the atomic medium and Γ_r is the population radiative decay rate of the excited state. Here, we used the following definition of the off-diagonal matrix element that describes the transition dipole element of the cycling transition

$$d_0^2 = \frac{\Gamma_r}{8\pi^2} 3\epsilon_0 \hbar \lambda^3 . \quad (1.13)$$

Using Eq. 1.11 and Eq. 1.12, we find

$$\chi_{ae} = \frac{d_{ae}^2 \text{OD}_0}{d_0^2} \frac{\Gamma_r}{kL\Omega_s} \rho_{ae} = \text{OD}_s \frac{\Gamma_r}{kL\Omega_s} \rho_{ae} , \quad (1.14)$$

where $\text{OD}_s = d_{\text{ae}}^2 \text{OD}_0 / d_0^2$ is the optical depth on the signal transition. We are interested in the power transmission T of the signal field past one atom or an atomic ensemble. We can model the transmission as

$$T = |h|^2, \quad (1.15)$$

where h is the amplitude transfer function [81, 125]

$$h = \exp \left[i \frac{k_s L}{2} \chi_{\text{ae}} \right] = \exp \left[i \frac{\text{OD}_s}{2} \chi_{\text{ae}} \right] = \exp \left[i \frac{\text{OD}_s}{2} \frac{\Gamma_r}{\Omega_s} \rho_{\text{ae}} \right]. \quad (1.16)$$

In our system, the individual atoms are coupled to the modes of a nanofiber with the directional coupling constants [126]

$$\beta^\pm = \frac{\Gamma^\pm}{\Gamma_{\text{tot}}}, \quad (1.17)$$

where the subscript \pm indicates the two propagation directions of the guided modes, Γ_\pm is the spontaneous emission rate into the nanofiber, Γ_{tot} is the total emission rate. If $\beta^\pm \ll 1$, then the emission rate is proportional to the optical depth

$$\beta^\pm = \frac{\text{OD}_s^\pm}{4N}, \quad (1.18)$$

where N is the number of atoms. Therefore, the transmission of a nanofiber-guided field through an ensemble of nanofiber-trapped atoms follows Beer-Lambert's law

$$T = \left| \exp[i2N\beta^\pm \chi_{\text{ae}}] \right|^2. \quad (1.19)$$

In particular, this shows that we expect an exponential scaling of the gain with the number of atoms.

In our system, we can usually assume that the signal field Rabi frequency is much smaller than the pump field Rabi frequency, i.e., $\Omega_s \ll \Omega_p$. Then, the incoherent scattering due to spontaneous decay from $|e\rangle$ transfers more atoms from $|b\rangle$ to $|a\rangle$ than vice versa until an equilibrium is reached. Then, the signal transmission is proportional

1.3. Theoretical Description

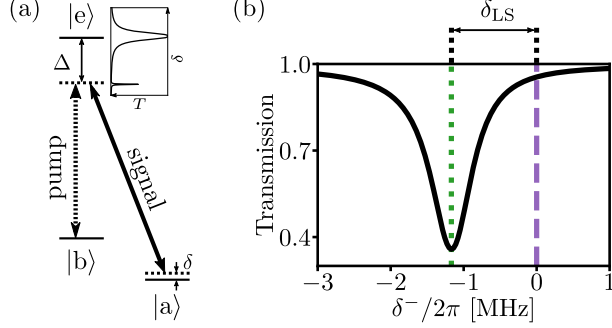


FIGURE 1.3: Illustration of the pump-field induced light shift. (a) Levels and transitions of our Λ -system. The inset shows schematically the theoretically expected steady-state signal transmission spectrum. (b) Zoom on the two-photon resonance in the signal transmission spectrum. Due to the light shift induced by the pump field, the dressed-atom two-photon resonance (dotted green line) is shifted by δ_{LS} with respect to the bare-atom two-photon resonance (purple dashed line).

to the steady-state $\tilde{\chi}_{\text{ae}}$, given by [81, 125]

$$\tilde{\chi}_{\text{ae}} = \frac{\gamma_e}{2} \times \left[\frac{4\delta^- (|\Omega_p|^2 - 4\delta^- \Delta) - 4\Delta\gamma_{\text{ab}}^2}{||\Omega_p|^2 + (\gamma_e + i2\Delta)(\gamma_{\text{ab}} + i2\delta^-)|^2} + i \frac{8(\delta^-)^2\gamma_e + 2\gamma_{\text{ab}} (|\Omega_p|^2 + \gamma_{\text{ab}}\gamma_e)}{||\Omega_p|^2 + (\gamma_e + i2\Delta)(\gamma_{\text{ab}} + i2\delta^-)|^2} \right]. \quad (1.20)$$

We use this equation to calculate the steady-state transmission spectrum of the signal field. Fig. 1.3 shows such a spectrum around the two-photon resonance. As illustrated in Fig. 1.3(a), we define δ with respect to the bare states of the atom. However, the pump field induces a light shift on the $|b\rangle \rightarrow |e\rangle$ transition, leading to a shift of the resonance condition at which two-photon Raman gain and absorption occur (see Fig. 1.3(b)). We can calculate this light shift with [127]

$$\delta_{\text{LS}} = \frac{1}{2} \left(\sqrt{\Omega_p^2 + \Delta^2} - |\Delta| \right). \quad (1.21)$$

For typical values of $\Delta = -2\pi \times 82$ MHz and $\Omega_p = 2\pi \times 20$ MHz, we find that the resonance of the dressed state is shifted by $\delta_{\text{LS}} \approx 2\pi \times 1.2$ MHz with respect to the bare state resonance.

We now discuss the case when the pump and the signal field fulfill the dressed-atom two-photon resonance and describe the dependence of the resulting dynamics on the Rabi frequencies and the decoherence rates. For such a Λ coupling, the population oscillation between the ground states depends on the two-photon Rabi frequency

$$\Omega_{2p} = \frac{\Omega_p \Omega_s}{2\Delta} . \quad (1.22)$$

If we can adiabatically eliminate the excited state [128] and if Ω_{2p} is much larger than the decoherence rates, the dynamics is coherent. In this regime, stimulated Raman scattering leads to energy transfer between the two laser fields. Similar to the two-level system discussed in Sec. 1.3.1, while population is transferred from $|b\rangle$ to $|a\rangle$, the signal field experiences gain. Conversely, when population is transferred from $|a\rangle$ to $|b\rangle$, the signal beam experiences attenuation. In the coherent regime, gain and loss vary periodically with time. The period of these oscillations is given by $2\pi/\Omega_{2p}$, resulting from the two-photon Rabi oscillations of the ground state populations. Here, the signal transmission and the populations oscillate 90° out of phase (see Fig. 1.1(b)). For nanofiber-trapped cold atoms, coherent Raman transfers were recently used to cool the atoms [129] and to measure the in-trap atomic motion [130].

If Ω_{2p} is much smaller than the decoherence rates, the dynamics is incoherent. In this regime, rate equations describe the population transfer and the corresponding signal gain and absorption. Here, signal gain is proportional to the population difference between $|a\rangle$ and $|b\rangle$. The small-signal gain is independent of the signal power, P_s . This is in contrast to the coherent regime, where the gain is proportional to $1/\Omega_{2p}$. There, the gain is thus proportional to $1/\sqrt{P_s}$.

1.3.3 Numerical Calculations of a Three-Level Λ -Type System

In this section, we discuss numerical calculations of the time evolution of the signal transmission. We use a cascaded model where we consecutively solve the master equation for every atom coupled to the signal and the pump field in a Λ configuration (see Fig. 1.2). We propagate the signal field through the array of atoms to find the total signal transmission.

Our theoretical model involves two classical laser fields, the signal and the pump field, and a three-level Λ -type system. The most relevant features are captured in the interaction Hamiltonian. Using the dipole and the rotating-wave approximation, the interaction Hamiltonian for the first atom in an appropriate rotating frame [128] is

1.3. Theoretical Description

given by [125, 131]

$$\hat{H} = -\frac{\hbar}{2} \begin{bmatrix} 0 & 0 & \Omega_s \\ 0 & 2\delta & \Omega_p \\ \Omega_s & \Omega_p & 2\Delta \end{bmatrix}. \quad (1.23)$$

Here, we consider real Rabi frequencies Ω_s and Ω_p . Using the operators $\hat{\sigma}_{ij} = |j\rangle\langle i|$ with $(i, j = a, b, e)$, we can rewrite the Hamiltonian, and find

$$H(t) = -\frac{\hbar}{2} \cdot \left[\Omega_s \cdot \hat{\sigma}_{ae} + 2\delta \cdot \hat{\sigma}_{bb} + \Omega_p \cdot \hat{\sigma}_{be} + \Omega_s \cdot \hat{\sigma}_{ae}^\dagger + \Omega_p \cdot \hat{\sigma}_{be}^\dagger + 2\Delta \cdot \hat{\sigma}_{ee} \right]. \quad (1.24)$$

Additionally, we define three collapse operators

$$\begin{aligned} \hat{c}_1 &= \sqrt{\gamma_{ea}} \cdot \hat{\sigma}_{ea}, \\ \hat{c}_2 &= \sqrt{\gamma_{eb}} \cdot \hat{\sigma}_{eb}, \\ \hat{c}_3 &= \sqrt{\gamma_{ba}} \cdot \hat{\sigma}_{bb}, \end{aligned} \quad (1.25)$$

where \hat{c}_1 describes the spontaneous population decay from $|e\rangle$ to $|a\rangle$, \hat{c}_2 the spontaneous population decay from $|e\rangle$ to $|b\rangle$, and \hat{c}_3 describes the decoherence between $|a\rangle$ and $|b\rangle$ [125]. In our system, the spontaneous decay rates of the excited state are $\gamma_{ea} = 5/12\gamma_e$ and $\gamma_{eb} = 7/15\gamma_e$, where γ_e is the total excited state population decay rate. In a realistic cesium level scheme, other decays are also possible. However, the rate to other Zeeman substates is $7/60\gamma_e$, i.e., much smaller. Therefore, we neglect it in the modeling of the Λ system.

To find the dynamics of the system, we use the master equation formalism. We find the evolution of the corresponding density operator, $\hat{\rho}$, with the Lindblad master equation [132–134]

$$\frac{d\hat{\rho}(t)}{dt} = -\frac{i}{\hbar} [\hat{H}(t), \hat{\rho}(t)] + \sum_n \frac{1}{2} \left[2\hat{c}_n \hat{\rho}(t) \hat{c}_n^\dagger - \hat{\rho}(t) \hat{c}_n^\dagger \hat{c}_n - \hat{c}_n^\dagger \hat{c}_n \hat{\rho}(t) \right]. \quad (1.26)$$

We use the Quantum Toolbox in Python (QuTiP) [135] to set up the Lindblad master equation and use the function “qutip.mesolve” to solve it. We compute the amplitude transfer function $h_1(t)$ and the signal transmission $T_1(t)$ past one atom with Eq. 1.15 and Eq. 1.16, respectively.

Now, we describe our cascaded model to compute the signal transmission through the atomic ensemble. For the first atom, we assume a signal Rabi frequency $\Omega_{s, 1}$ that

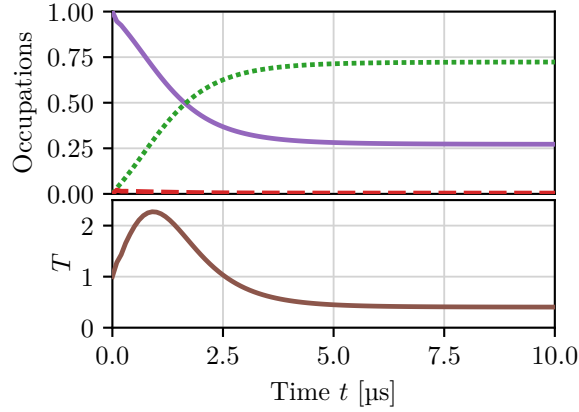


FIGURE 1.4: Evolution of the state populations and signal transmission. Upper panel: We start with all atoms in $|b\rangle$ (solid purple line). At $t = 0 \mu\text{s}$, we switch on the pump and the signal field. The two laser fields transfer population from $|b\rangle$ to $|a\rangle$ (dotted green line). The population in $|e\rangle$ (dashed red line) is always much less than the populations in the other states. lower panel: In the signal transmission T , we see amplification up to $t \approx 2.5 \mu\text{s}$. In this time interval, more atoms are transferred from $|b\rangle$ to $|a\rangle$ than in the other direction. At $t \approx 5 \mu\text{s}$, a steady-state of absorption is reached.

is constant in time. Since the first atom modulates the transmitted signal field, the second atom will be driven by a time-dependent signal Rabi frequency. To take this into account, we compute a cubic spline interpolation of $\Omega_{s,2}(t) = \Omega_{s,1}h_1(t)$ using the function “`qutip.interpolate.Cubic_Spline`”. Then, we replace Ω_s in Eq. 1.24 with $\Omega_{s,2}(t)$ and compute the amplitude transfer function $h_2(t)$ and the signal transmission $T_2(t)$ after the second atom. Subsequently, the third atom is driven by $\Omega_{s,3}(t) = \Omega_{s,2}h_2(t)$, and so on. That way, we numerically propagate the signal field through the atomic ensemble.

Figure 1.4 shows the results of the signal transmission after 1420 atoms, as well as the average state populations of the atoms. For this simulation, we use the parameters presented in Tab. 1.1. We start with all atoms in $|b\rangle$. At $t = 0 \mu\text{s}$, we switch on the pump and the signal field. The fields start to transfer population from $|b\rangle$ to $|a\rangle$ while the population in $|e\rangle$ always remains below 2.2%, which we consider negligible.

1.3. Theoretical Description

TABLE 1.1: Overview of the parameters of our system. We present the values used in our numerical model for computing the signal transmission (see Fig. 1.4 and dashed line in Fig. 3.1b). For comparison, we also list independent estimations of those parameters and from where we infer the estimation.

Parameter	Model parameters	Independent estimate	Inferred from
Ω_s	$2\pi \times 0.95$ MHz	$2\pi \times 1.6$ MHz	Measured transmitted signal power and atom–fiber distance (see Sec. 2.7)
Ω_p	$2\pi \times 20.7$ MHz	$2\pi \times 19.96(9)$ MHz	Measured Autler-Townes splitting (see Sec. 2.6.2)
Δ	$2\pi \times 82$ MHz	$2\pi \times 82.30(3)$ MHz	Measured signal transmission spectrum (see Sec. 2.6.3)
$\delta^- + \delta_{LS}$	$2\pi \times 0$ MHz	$2\pi \times 0.00(2)$ MHz	Gain spectrum (see Sec. 3.5)
N	1420	1412(168)	Measured transmission spectrum (see Sec. 2.2)
OD_s	0.00655	0.0122(15)	Saturation measurement (see Sec. 2.2)
γ_{ba}	$2\pi \times 0.29$ MHz	$2\pi \times 0.47(3)$ MHz	Gain spectrum (see Sec. 3.5)
γ_e	$2\pi \times 5.225$ MHz	$2\pi \times 5.225(8)$ MHz	Literature value [136]

As expected for the coherent regime, the signal transmission increases linearly in the beginning. In this regime, we would also expect that the maximum of the gain occurs when the populations in the ground states are equal at a quarter of a period of the two-photon Rabi frequency (c.f. Eq. 1.4 and Fig. 1.1)

$$T/4 = \frac{1}{4} \frac{2\pi}{\Omega_{2p}} = \frac{1}{4} \frac{2\pi}{2\pi \times 120 \text{ kHz}} \approx 2 \mu\text{s} . \quad (1.27)$$

However, the gain in the simulation reaches a maximum earlier at $t = 0.9 \mu\text{s}$ which is also before the population in the ground states are equal at $t \approx 1.5 \mu\text{s}$. We infer from these simulated results that the system is in a partially coherent regime. Amplification prevails for $\sim 2.5 \mu\text{s}$, and then, the signal field experiences loss due to two-photon absorption. After $t \approx 5 \mu\text{s}$, we start to reach a steady state of the populations and the signal transmission.

One of the main sources of decoherence in our system is the off-resonant scattering rate of the laser fields. We infer the scattering rate R_{sc} from the average excited state population ρ_{ee} by calculating the total photon scattering rate

$$R_{\text{sc}}(t) = \gamma_e \rho_{ee}(t) . \quad (1.28)$$

Fig. 1.5 shows the evolution of the scattering rate. After switching on the laser fields, the scattering rate reaches a maximum at $\sim 500 \text{ kHz}$ and then decreases to $\sim 100 \text{ kHz}$. About 1% of the photons are scattered into the guided modes of the nanofiber. For typical atom numbers of $N = 1500$, the scattering rate of photons into the nanofiber modes is less than 7.5 MHz , which is much less than typical signal photons rates of more than 35 MHz .

1.3. Theoretical Description

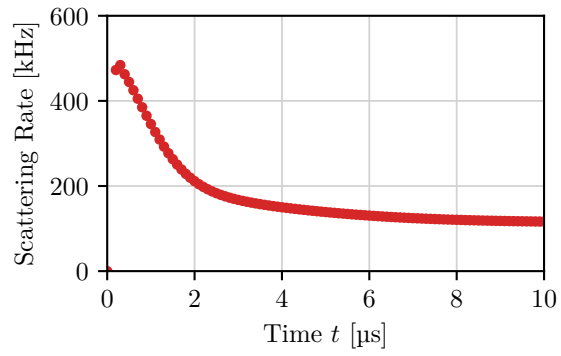


FIGURE 1.5: Off-resonant scattering rate of the laser fields. From the population in $|e\rangle$, we deduce the one-photon scattering rates of the laser fields. We ascertain scattering as one of the major sources of decoherence in our system. Initially, the scattering rate is ~ 500 kHz and then decreases to ~ 100 kHz.

Chapter 2

Experimental Setup for the Amplification Measurements

In this chapter, we present our experimental setup and method to measure atomic spin-controlled non-reciprocal Raman amplification. First, we discuss our optical two-color dipole trap and the preparation of the atomic ensemble. Then, we present the setup of the pump and the signal laser fields and discuss the data acquisition. Finally, we show how we calibrate the pump and signal Rabi frequencies theoretically and experimentally.

2.1 Nanofiber-Based Dipole Trap

As illustrated in Fig. 2.1, our implementation of non-reciprocal amplification is based on a nanofiber-based optical dipole trap [15]. The nanofiber is made out of a commercial single-mode fiber¹. After stretching the fiber, the tapered section has a length of 4 cm [15]. The weakly guided mode LP_{01} of the unstretched fiber is adiabatically transformed into the strongly nanofiber-guided HE_{11} mode [138, 139]. The nanofiber waist has a diameter of 500 nm over a length of 5 mm. After passing the nanofiber section, the guided mode is transformed back to the initial LP_{01} mode. The transmission through the entire tapered fiber was reported to be $\sim 97\%$ [15].

We couple the trapping light fields into the two ports of the tapered optical fiber. The blue-detuned trapping light field is derived from a laser² with a free-space wavelength of $\lambda = 760$ nm [140], and the power transmitted through the tapered optical fiber

¹Liekki 6/125 Passive [137]

²Toptica, TA pro, LD-0780-0080-AR-3 and TA-0765-2000-1

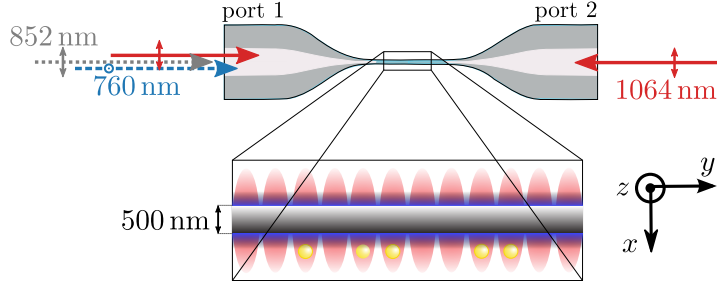


FIGURE 2.1: Illustration of our nanofiber-based dipole trap. The blue-detuned running wave at $\lambda = 760$ nm (dashed blue arrow) is quasi-linearly polarized along the z -axis. The red-detuned standing wave at $\lambda = 1064$ nm (solid red arrows) is quasi-linearly polarized along the x -axis. In combination, these fields create the trapping potential. We use a resonant laser field at $\lambda = 852$ nm (dotted gray arrow) that is quasi-linearly polarized along the x -axis to prepare the atoms on one side of the nanofiber and subsequently measure the number of trapped atoms (yellow balls).

is ~ 20.5 mW. We launch it as a running wave into the fiber. We send a red-detuned field with $\lambda = 1064$ nm provided by a Nd-YAG laser³ into both ports of the fiber. The fields have a total power of ~ 2.4 mW and form a standing wave. We choose the z axis as the quantization axis. All trapping light fields are quasi-linearly polarized [115]. The polarization plane of the blue-detuned trapping light field is orthogonal to the polarization plane of the red-detuned light field, where the latter defines the plane where the atoms are trapped.

The fields form two diametric arrays of optical trapping sites with a spatial period of 498 nm [115] along the nanofiber. In Fig. 2.2(a), we present the radial trapping potential depending on the radial distance r from the surface of the nanofiber. The potential results from optical dipole forces [115, 141–143] arising from the repulsive blue-detuned and attractive red-detuned trapping fields. We also take surface effects into account [143–145]. Specifically, we consider here the repulsive exchange interactions and the attractive Casimir-Polder interaction [146–148]. For our settings, we find a local radial trapping minimum at ~ 230 nm away from the nanofiber surface.

We now study the radial motional states. We calculate the eigenvalues E_ν and

³Spectra Physics, Excelsior 1064-650

2.1. Nanofiber-Based Dipole Trap

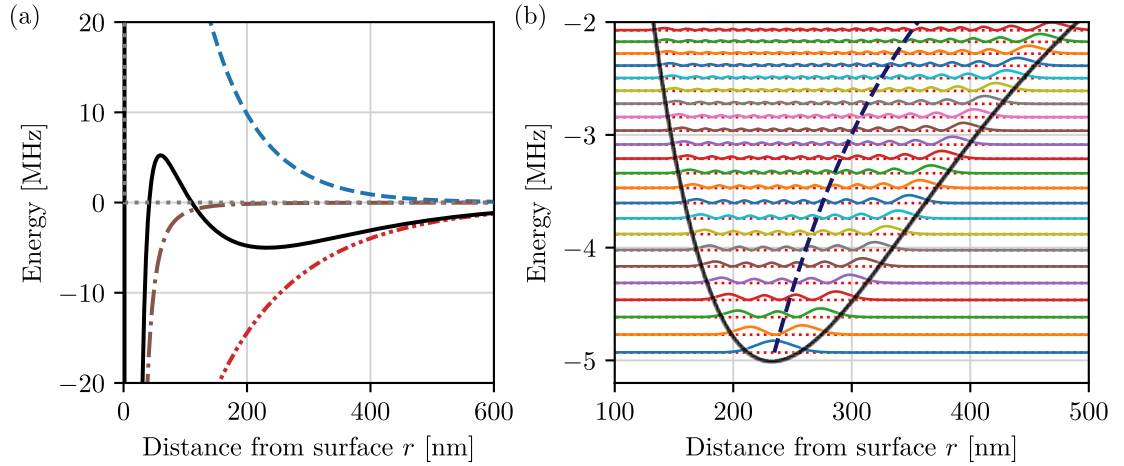


FIGURE 2.2: The radial trapping potential. (a) We consider four contributions to the total radial potential (solid black line): the potentials induced by the blue-detuned laser field (dashed blue line), by the red-detuned laser field (dash-dot-dotted red line), by the Casimir-Polder interaction (dash-dotted brown line), and by the exchange interaction (dotted gray line). (b) Radial motional states. We present the energy of the motional states (dotted red lines) and the corresponding probability densities of finding an atom as a function of the radial distance from the surface (solid colored lines) as well as the total radial potential. The dashed dark-blue line indicates the mean position of the atoms. Due to the anharmonicity of the potential, hotter atoms are, on average, further away from the nanofiber surface.

eigenvectors $\psi_\nu(r)$ close to the local minimum of the total radial trapping potential. Here, ν is the radial quantum number. In Fig. 2.2(b), we present the eigenvalues from $\nu = 1$ to $\nu = 23$ as dotted red lines. For every eigenvalue, we present the probability densities of the radial position of the atoms, inferred from the eigenvectors via

$$p_\nu(r) = r |\psi_\nu(r)|^2 . \quad (2.1)$$

The mean position of an atom in a motional state ν is given by

$$\bar{p}_\nu = \sum_i r_i p_\nu(r_i) , \quad (2.2)$$

where the index i runs over all discrete values of r used in the numerical calculation. We find that hotter atoms are, on average, further away from the surface of the nanofiber. Hence, the intensities of the fiber-guided laser fields at the mean position of the atoms changes with ν , resulting in variations of the corresponding Rabi frequencies. In an atomic ensemble, this effect can lead to a considerable dephasing of the Rabi oscillations [130].

2.2 Preparation of the Atomic Ensemble

We load the atoms from a MOT into the nanofiber-based trap via an optical molasses stage [15]. Due to the collisional blockade effect, we load at most one atom per trapping site [149]. The filling of the trapping sites is random, and the mean occupation number is at most 0.5 atoms per trapping site [150]. On one side of the nanofiber, there are about $5 \text{ mm}/498 \text{ nm} = 10040$ trapping sites. We trap up to 2000 atoms, corresponding to an average filling factor of $\sim 20\%$. Note that the atoms are probably not trapped over the entire 5 mm long nanofiber, but only in one section. In this case, the filling factor would be higher in this nanofiber segment. To investigate this, one would need to take fluorescence images, as has been done in the past [15, 137].

Next, we turn on a fiber-guided laser field that is tuned close to the cesium cycling transition $|6S_{1/2}, F = 4, m_F = -4\rangle \rightarrow |6P_{3/2}, F = 5, m_F = -5\rangle$ (see Fig. 2.3). The laser field selectively heats atoms on only one side of the nanofiber [155]. We apply this side-selective degenerate Raman heating for 40 ms, which is sufficiently long so that practically all hot atoms are lost from the trap. Simultaneously, the atoms in the opposite array experience degenerate Raman cooling and are optically pumped to the

2.2. Preparation of the Atomic Ensemble

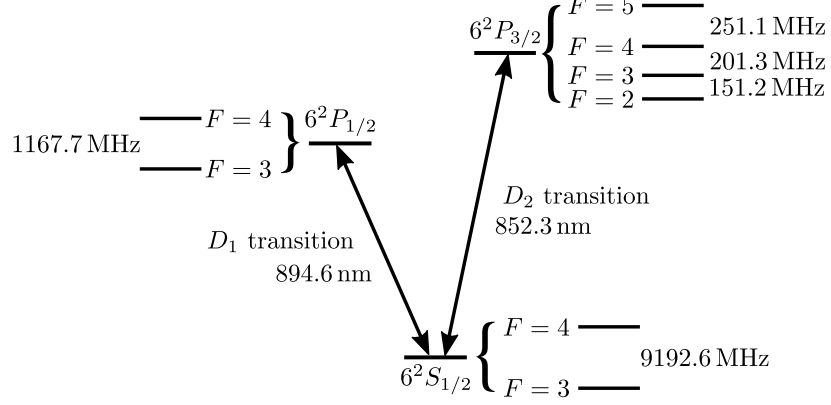


FIGURE 2.3: Energy levels of the cesium D lines. The two transitions are D_1 ($6S_{1/2} \rightarrow 6P_{1/2}$) and D_2 ($6S_{1/2} \rightarrow 6P_{3/2}$). We present the hyperfine structure (not to scale), with frequency splittings between the hyperfine energy levels. The values are taken from [151–154].

$|6S_{1/2}, F=4, m_F=-4\rangle$ state [155]. It turns out that the cooling is most efficient for an offset magnetic field of ~ 0.5 G, applied along $+z$. Here, the atoms are held close to their motional ground state, resulting in long trapping times of ~ 1 s compared to passive lifetimes of ~ 50 ms.

To infer the number of remaining trapped atoms, we measure the transmitted power of a fiber-guided probe laser field while sweeping its frequency across the cycling transition $|6S_{1/2}, F=4\rangle \rightarrow |6P_{3/2}, F'=5\rangle$. At the location of the atoms, the probe field is σ^- polarized, and, hence, the atoms stay in the $|F=4, m_F=-4\rangle$ state. From a fit of the transmission spectrum, we obtain the optical depth (OD) of the atomic ensemble. To convert that into the number of trapped atoms, N , we measure the saturation power of the atomic ensemble [15]. We tune the frequency of the probe laser on resonance and detect the absorbed power as a function of the input power (see Fig. 2.4). We perform a fit based on a saturation model [15, 137]. The atomic ensemble with N atoms absorbs at most $P_{\text{abs}} = 0.286(3)$ nW. A single cesium atom can at most scatter a power of [15, 137]

$$P_{\text{sat}} = \frac{hc \gamma_e}{\lambda} = 3.8 \text{ pW}, \quad (2.3)$$

where h is the Planck constant, c is the speed of light, and $\lambda = 852$ nm is the wavelength of the D_2 transition. Hence, we infer that $N = P_{\text{abs}}/P_{\text{sat}} = 75(1)$ atoms were

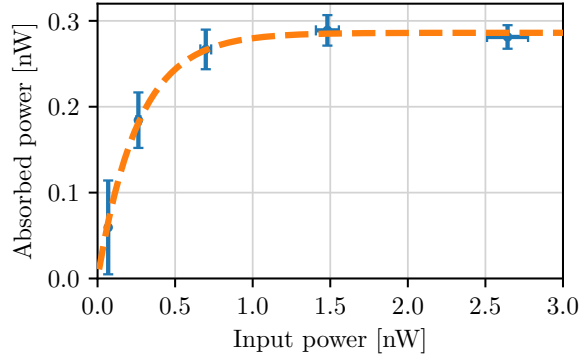


FIGURE 2.4: Calibration of the optical depth (OD) per atom. We measure the absorbed power of the atomic ensemble as a function of the input power (sots). We perform a fit to obtain the saturation power, which we use to infer the number of trapped atoms and the OD per atom.

trapped during this measurement. With a fit on the independent measurement of the transmission spectrum, we obtain $\text{OD}_0 = 2.2(3)$. Hence, we infer an OD per atom of ~ 0.03 .

In our cooling scheme, the atoms are optically prepared in the $|F = 4, m_F = -4\rangle$ state at an offset magnetic field of ~ 0.5 G. To demonstrate non-reciprocal amplification, we ramp the magnetic field up to ~ 7 G within 7 ms. This guiding offset magnetic field ensures that the atoms do not couple to other Zeeman substates due to, e.g., spin-motion coupling [80], i.e., they will stay in state $|F = 4, m_F = -4\rangle$. If the atoms are to be prepared in the $|F = 4, m_F = +4\rangle$ state, we subsequently apply an optical pumping scheme. We use a free-space preparation laser field that propagates in the $+z$ -direction (see Fig. 2.5). This field is σ^+ polarized and couples to the $|6S_{1/2}, F = 4\rangle \rightarrow |6P_{1/2}, F' = 4\rangle$ transition of the D_1 line (see Fig. 2.3). The preparation field, together with a repumper at the $|6S_{1/2}, F = 3\rangle \rightarrow |6P_{3/2}, F' = 4\rangle$ transition, pumps the atoms to the $|F = 4, m_F = +4\rangle$ dark state. We made sure that the number of atoms in other states is negligible. However, during this optical pumping step, we heat the atoms and lose $\sim 40\%$ of them. The amplification of the signal field is thus smaller in this case.

2.3. Non-Reciprocal Amplification Setup

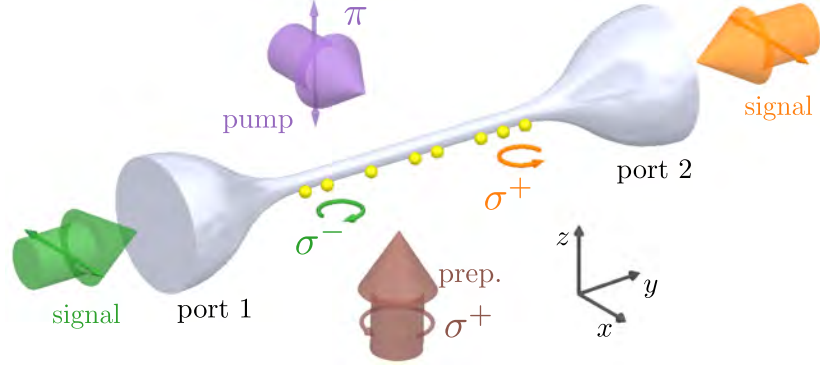


FIGURE 2.5: Individual cesium atoms (yellow balls) are trapped in one array parallel to the nanofiber. We launch the signal light into port 1 or port 2 and measure the transmitted power. We choose the quantization along $+z$. Then, depending on the propagation direction, the evanescent field of the signal mode in the nanofiber is predominantly σ^- -polarized (green circular arrow) or σ^+ -polarized (orange circular arrow) at the location of the atoms, enabling the directional light-matter coupling. The pump field is π -polarized and propagates in the $+x$ -direction. We use a free-space σ^+ polarized preparation laser field if the atoms are to be prepared in the $|F = 4, m_F = +4\rangle$ state (brown arrow).

2.3 Non-Reciprocal Amplification Setup

Fig. 2.5 shows the experimental setup schematically. We place the nanofiber along y in a Cartesian coordinate system (quantization axis: $+z$). The cesium atoms are trapped in one array in the x - y plane along the nanofiber.

The π -polarized free-space pump laser beam propagates in the $+x$ -direction, i.e., orthogonal to the probing direction. Hence, it cannot break reciprocity. We stabilize the intensity of the pump field. Then, we use an acousto-optic modulator⁴ (AOM) to switch the pump field on in a few tens of nanoseconds. At the position of the atoms, the beam has a cross-sectional area of $\sim 30 \text{ mm}^2$, and we assume that it illuminates the atoms with equal intensity.

We launch the quasi-linearly polarized signal field [115] into port 1, port 2, or into both ports simultaneously (see Fig. 2.5). Then, we measure the respective power

⁴AA Opto Electronic, MT110-B50A1-IR

transmissions $T_{1 \rightarrow 2}$ and $T_{2 \rightarrow 1}$. At the position of the atoms, the evanescent part of the nanofiber-guided signal field has a transverse component along the x -axis and a longitudinal component along the y -axis. When the signal field propagates in the $+y$ -direction, i.e., from port 1 to port 2, the electric field in the x - y plane is given by

$$\mathbf{E} = \begin{pmatrix} E_x \\ E_y \\ 0 \end{pmatrix} e^{iky} e^{-\eta x} , \quad (2.4)$$

where η is the decay constant and e^{iky} describes a wave that propagates along y with a wave vector k . This field has to fulfill Maxwell equations. For a charge- and current-free dielectric medium, Gauss's law yields

$$\text{div } \mathbf{E} = 0 . \quad (2.5)$$

When we apply that on Eq. 2.4, we find

$$E_y = -i \frac{\eta}{k} E_x . \quad (2.6)$$

Hence, the transverse and longitudinal components are proportional to each other. In our system, the factor η/k is on the order of 1 because $\eta \approx k = 2\pi/\lambda$, where λ is the optical wavelength. Hence, the transverse field component is approximately as large as the longitudinal component. The imaginary unit $-i$ in Eq. 2.6 acts as a phase factor, i.e., the transverse and longitudinal components oscillate 90° out of phase with respect to each other. The superposition of the two fields thus gives rise to elliptical polarization. For our parameters, the polarization is almost perfectly circular [79]. Therefore, an atom in the evanescent part of the guided light field sees almost perfect σ^- polarization. Specifically, for our parameters, the overlap of the signal field at the position of the atoms with σ^- (σ^+) was calculated to be 92 % (8 %) [79]. Note that this circular polarization is different from the circular polarization of, e.g., a weakly focused laser beam in free space because the electric field vector rotates in the x - y plane that contains the propagation direction.

When the signal field propagates in the opposite direction, i.e., in the $-y$ direction, the phase factor becomes

$$e^{iky} \rightarrow e^{-iky} . \quad (2.7)$$

Then, the electric field rotates in the other sense

$$E_y \approx +iE_x . \quad (2.8)$$

Hence, the sense of rotation changes with the direction of propagation [25]. Thus, an atom in the evanescent field is exposed to almost perfect σ^+ polarized light when the signal field propagates in the $-y$ direction. The overlap of the signal field at the position of the atoms with σ^- (σ^+) is now 8 % (92 %) [79].

2.4 Beam Path of the Signal Laser

Here, we discuss the beam path of the signal laser beam. We stabilize the relative frequency between the signal laser and the pump laser with a phase locked loop [156]. Then, we send the signal laser beam to its main setup. In Fig. 2.6, we illustrate the core elements. At first, a glass substrate⁵ reflects a fraction of the beam. A photodiode detects the power of the reflected beam. We use the photodiode signal in conjunction with a feedback loop to stabilize the initial power of the signal beam. We split the beam into two beams with equal power with a 50:50 beamsplitter⁶. We send the two beams in opposite directions through the nanofiber. If we want to launch light only in one direction, we block the other beam with an optical shutter⁷.

With Berek compensators⁸, i.e., variable retardation plates, we set the polarization of the signal beams at the nanofiber waist to quasi-linearly polarization in the x - y plane [115, 150]. Specifically, the Berek compensator that sets the polarization of the beam propagating from port 1 to port 2 is mounted in front of the 50:50 beamsplitter. A second Berek compensator after the 50:50 beamsplitters controls the polarization of the beam that propagates in the $2 \rightarrow 1$ direction. To verify the quasi-linear polarization, we rotate it in the $x - z$ plane in the nanofiber. Then, we measure the scattered light from the side with a CCD camera, similar to how it was reported by E. Vetsch *et al.* [150]. We observe a Michelson contrast modulation of the detected optical power of more than 70 % in both directions. This is in agreement with previously reported contrasts and, thus, we conclude that the polarization is quasi-linear.

⁵FOCtek, BK7 window

⁶Thorlabs, BS014

⁷Stanford Research Systems, SR474

⁸FOCtek, YVO4 crystal

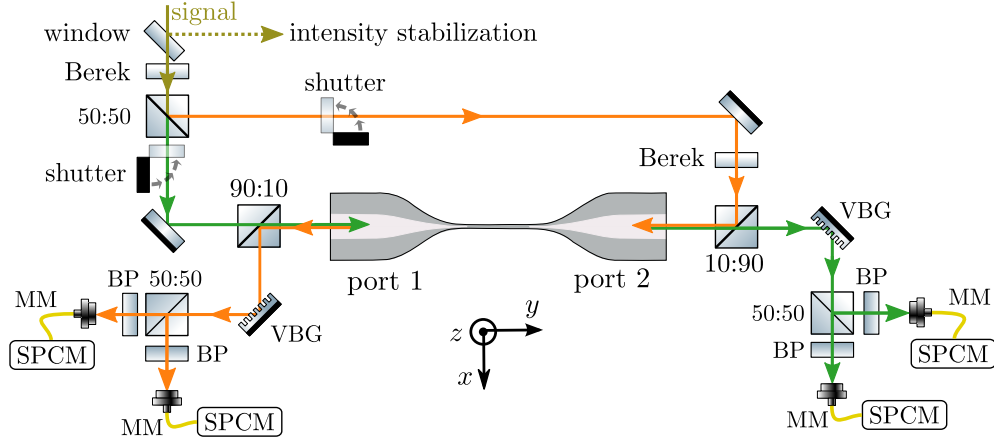


FIGURE 2.6: Main components of the signal laser’s beam path. We split the beam with a 50:50 beamsplitter and send it in both directions through the nanofiber (indicated by the green and orange beam paths). With shutters, we control the propagation direction of the beam. We use 90:10 and 10:90 beamsplitters to separate the transmitted beam from the incoming beam, and that way, we send 90% of the transmitted light to the detection setups. (BP, bandpass filter; MM, multi-mode fiber; VBG, volume Bragg grating; SPCM, single-photon counting module)

We use 90:10 and 10:90 beamsplitters to combine and separate the transmitted and impinging beams. The beam that is launched into port 1 passes a 90:10 beam splitter⁹ in front of the nanofiber, i.e., a beam power of 10% is transmitted through the beam splitter and launched into the nanofiber. The beam leaves the nanofiber via port 2 and hits a 10:90 beamsplitter¹⁰ where 90% of the beam power is transmitted to the detection setup. Similarly, 10% of the power of the second beam is reflected towards the nanofiber. After passing the nanofiber in the $2 \rightarrow 1$ direction, 90% of the beam power is reflected and guided to the detection setup.

The detection setups on both sides are identical. We use dichroic mirrors and a volume Bragg grating¹¹ centered around 852 nm to separate the signal field from

⁹Thorlabs, BS074

¹⁰Thorlabs, BS041

¹¹OptiGrate, RBG-852-94

the trapping light fields. To increase the detected signal without saturating our detectors, we split up the signal beam with a 50:50 beamsplitter¹². Then, a bandpass filter¹³ centered around 852 nm further reduces background photon counts. The filtered transmitted light of the signal field is then sent onto single-photon-counting modules¹⁴ (SPCM) via multi-mode optical fibers¹⁵. We made sure that all detectors are operated far below saturation.

2.5 Data Analysis

The SPCMs detect single transmitted signal photons, spontaneously scattered pump photons in the nanofiber, and background photons. We use a field-programmable gate array¹⁶ to store the arrival times of these photons. Additionally, we record the electronic signal triggering the pump laser switch-on. We compute the time delay between the arrival time of every detected photon and the electronic trigger signal of the respective measurement cycle.

We repeat the measurement cycle until good counting statistics are reached and generate a histogram out of the time delays (see e.g. Fig. 2.7). Here, we use a bin size of 25 ns. Next, we convert that to the transmission of the signal field. To do so, first, we calculate and subtract the average background detected at the end of the measurement cycle. Then, we divide the histogram by the average SPCM photon counts before switching on the pump laser. Here, the signal field is not interacting with the atoms, i.e., the signal transmission is unmodified. We end up with a histogram corresponding to the time evolution of the signal transmission. Strictly speaking, this histogram also contains the spontaneously scattered photons in the nanofiber by the pump laser field. However, the signal photon rate is much higher than the rate of spontaneously scattered pump photons. Thus, we neglect the latter and refer to the detected signal as signal transmission.

¹²Thorlabs, BS014

¹³Semrock, LL01-852-12.5

¹⁴Excelitas Technologies, SPCM-AQRH-14-FC

¹⁵Thorlabs, M69L02

¹⁶ID Quantique, ID800

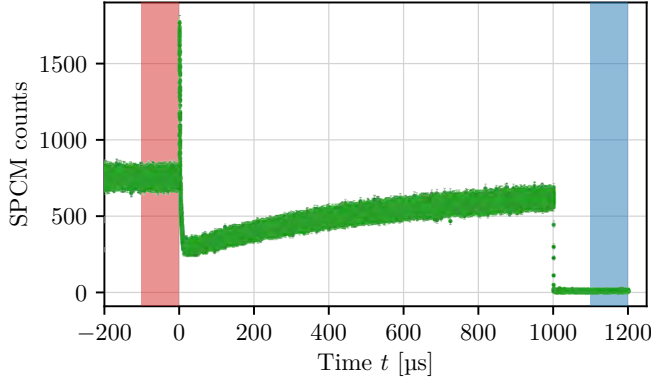


FIGURE 2.7: Histogram of the arrival times of the detected transmitted photons of the signal beam. To convert that to the transmission of the signal beam, we subtract the average background evaluated in the time interval indicated by the blue shaded area. Then, we divide that by the average SPCM counts in the time interval indicated by the red shaded area. In this interval, the signal field is not interacting with the atoms.

2.6 Calibration of the Pump Field

Here, we discuss how we calibrate the Rabi frequency and the detuning of the pump field. First, we present calculations of the intensity and polarization distribution of the pump field around the nanofiber. Then, we experimentally calibrate the pump field Rabi frequency using electromagnetically induced transparency (EIT) and Autler-Townes splitting. In the last section, we discuss the pump laser detuning and its impact on the signal-to-noise ratio of the signal gain. The discussion in this section closely follows the published manuscript [157].

2.6.1 Intensity and Polarisation Distribution of the Pump Laser Beam

In this section, we discuss analytical calculations of the intensity and polarization distribution of the pump field. We model the nanofiber as an infinite dielectric cylinder with a diameter of 500 nm. We approximate the impinging pump light field by a plane wave that has its wavevector perpendicular to the nanofiber axis. For such a situation, analytical solutions are available [158]. The pump field has a wavelength of

2.6. Calibration of the Pump Field

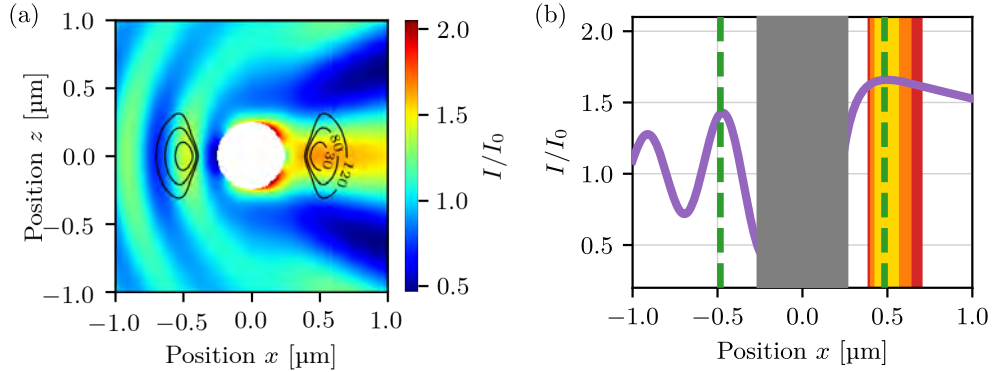


FIGURE 2.8: Pump field intensity around the nanofiber. We model the pump field as a π -polarized free-space plane wave that propagates in the $+x$ direction and impinges on an infinite dielectric cylinder along y . (a) The intensity distribution around the nanofiber is normalized to the incident intensity, I_0 . The black lines are the contours of the trapping potential with labels in microkelvin. At the atoms' location, the field's intensity is about $1.6I_0$. The gray-shaded region shows the extent of the nanofiber. (b) A horizontal cut at $z = 0$. We see that the gradient and curvature of the intensity are lower behind the fiber than in front of the fiber. The dashed green lines indicate the locations of the minima of the trapping potential. We also present the position of the atoms for temperatures of $30 \mu\text{K}$ (yellow area), $80 \mu\text{K}$ (orange area), $120 \mu\text{K}$ (red area).

$\lambda = 852.347 \text{ nm}$, an incident intensity I_0 , and it is s-polarized. This means that the electric field oscillates perpendicular to the fiber axis in the x - z plane, i.e., the pump field is π -polarization. Figure 2.8(a) shows the resulting intensity profile in the x - z plane and Fig. 2.8(b) a horizontal cut of the profile at $z = 0$. We see that the nanofiber acts as a cylindrical lens, creating an intensity maximum behind the nanofiber. In front of the nanofiber, we find intensity maxima and minima that arise from the interference of the impinging field with the field reflected by the nanofiber.

In Fig. 2.8(a), the black lines are the contours of the nanofiber-based two-color optical dipole trapping potential in the x - z plane with labels in microkelvin. We see that for typical temperatures of the atomic ensemble of $\sim 30 \mu\text{K}$, the pump intensity variations are negligible. The trap minima are located $\sim 234 \text{ nm}$ away from the surface

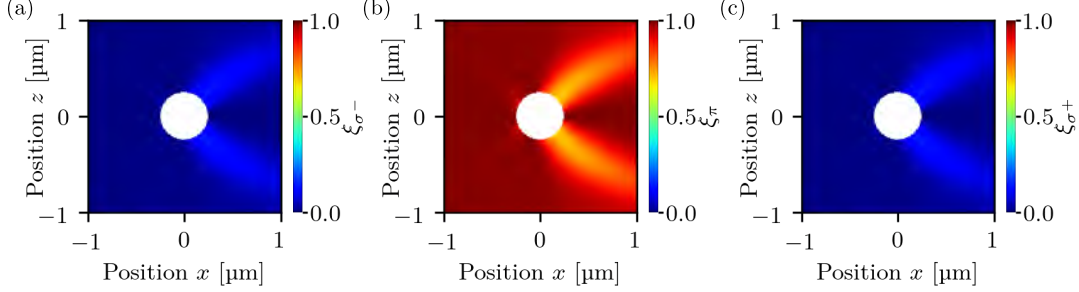


FIGURE 2.9: Polarization components of the pump field around the nanofiber. We model the pump field as a plan wave that propagates in the $+x$ direction. We present all three normalized polarization components (a) ξ_{σ^-} , (b) ξ_{π} , and (c) ξ_{σ^+} of the field around the nanofiber. In the trapping region, the deviations from a purely π -polarized laser beam are negligible.

of the nanofiber (dashed green lines in Fig. 2.8(b)). In our amplification scheme, we prepare atoms on only one side of the nanofiber. It turns out that the intensity gradient and the intensity curvature of the field are lower behind the fiber. Hence, we decided to heat out the atoms in front of the nanofiber and perform the experiment with atoms trapped behind the nanofiber. We find that the pump field's intensity is $I \approx 1.6I_0$ at the position of the atoms.

In Fig. 2.9(a)-(c), we depict the normalized polarization components ξ_{σ^-} , ξ_{π} , and ξ_{σ^+} of the pump field around the nanofiber. We find them by calculating the overlaps [79]

$$\xi_j = |\mathbf{u} \cdot \mathbf{e}_j|^2 \quad (2.9)$$

of the polarization vector \mathbf{u} , i.e., the electric field of the pump field, with the basis vectors

$$\mathbf{e}_{\sigma^+} = (\mathbf{e}_x - i\mathbf{e}_z) / \sqrt{2}, \quad (2.10)$$

$$\mathbf{e}_{\pi} = \mathbf{e}_y, \quad (2.11)$$

$$\mathbf{e}_{\sigma^-} = -(\mathbf{e}_x + i\mathbf{e}_z) / \sqrt{2}. \quad (2.12)$$

The polarization variations of the pump field can be, in general, significant. However, in the trapping region, the deviations from a purely π -polarized field are small, and it

is justified to neglect the σ^- and σ^+ components.

2.6.2 EIT and Autler-Townes Splitting

We use electromagnetically induced transparency (EIT) [125, 159] and the Autler-Townes effect [160] to experimentally ascertain the ground state decoherence rate and the pump field Rabi frequency, Ω_p . The distinction between these effects can be difficult. Both can produce a transparent window in an absorption band. However, EIT refers to a window that maintains transparency in a weak pump field and thus requires Fano interference [161]. Several recent publications studied the difference between EIT and Autler-Townes splitting theoretically [162–167] as well as experimentally [168–178]. Also, close to a nanofiber, both effects have been observed [81, 82, 179]. Here, we study EIT, the Autler-Townes splitting, and the transition between these effects with nanofiber-trapped atoms.

Electromagnetically Induced Transparency

We use a similar setup as it was employed by C. Sayrin *et al.* [81], where they stored light in a nanofiber-trapped ensemble of cold atoms using EIT. However, all light fields were fiber-guided. In contrast, our pump field is a free-space running wave with a wave vector that is perpendicular to the wave vector of the fiber-guided signal field. We implement a Λ system with these fields. The signal field propagates from port 1 to port 2 and is consequently σ^- polarized at the location of the atoms. It has a detuning δ from the $|6S_{1/2}, F = 3, m_F = -3\rangle \rightarrow |6P_{3/2}, F = 4, m_F = -4\rangle$ transition (see Fig. 2.10(a)). We tune the frequency of the π polarized pump field in resonance with the $|6S_{1/2}, F = 4, m_F = -4\rangle \rightarrow |6P_{3/2}, F = 4, m_F = -4\rangle$ transition, i.e., $\Delta = 0$ MHz.

We prepare the atoms in $|F = 4, m_F = -4\rangle$ on one side of the nanofiber using degenerate Raman cooling [155]. Then, we ramp up the magnetic field from ~ 0.5 G to ~ 13 G within 7 ms to suppress spin-motion coupling and stabilize the atomic spin state. We turn on the pump laser, which transfers the atoms to state $|F = 3, m_F = -3\rangle$. Subsequently, we switch on the signal laser, scan its frequency with a scanning speed of 120 MHz/ms over the atomic resonance, and measure the transmitted power using the SPCMs. The impinging intensity of the pump field is $I_0 \approx 0.36$ mW/cm², inferred from a measurement of the pump power and the beam diameter in front of the nanofiber. This corresponds to a calculated pump field Rabi frequency of $\Omega_p \approx 2\pi \times 1.4$ MHz. The nanofiber-guided power of the signal field is ~ 4 pW, resulting in a calculated $\Omega_s \approx$

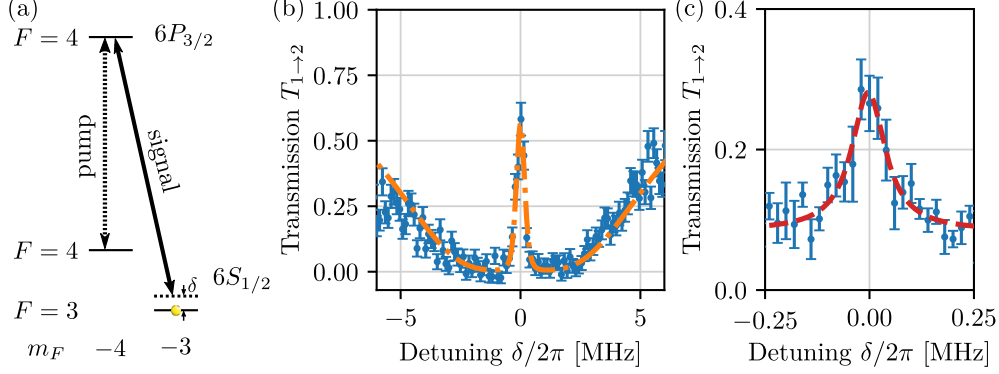


FIGURE 2.10: Transmission spectrum of the fiber-guided signal field in conjunction with a free-space pump field from the side under EIT conditions. (a) The Zeeman sublevels that we use to implement a Λ -system. Here, the pump laser is tuned on resonance, and the frequency of the signal laser is scanned over the respective resonance. (b) In the signal transmission spectrum (blue dots), we observe a transmission window with a full width at half maximum (FWHM) much narrower than the natural linewidth of 5.225(8) MHz [136]. We, thus, clearly observe EIT. The dash-dotted orange line is a fit (see text). (c) We decrease Ω_p and measure the transmission point-wise (blue dots). A Lorentzian fit unveils a FWHM of 30(4) kHz (dashed red line).

1 MHz. In Fig. 2.10, we present the signal transmission spectrum. At resonance, we observe a transmission window with a maximum detected transmission of 58(6) % on an optically dense background. It has a full width at half maximum (FWHM) of ~ 300 kHz, which is much narrower than the linewidth of the transition ($\gamma_e = 5.225(8)$ MHz [136]). Thus, we clearly observe EIT.

We fit the signal transmission spectrum by combining Eq. 1.15, Eq. 1.16, and Eq. 1.20. We fix $\Delta = 0$ MHz and $\gamma_e = 2\pi \times 5.225$ MHz. The fit agrees well with the experimental data (see dash-dotted orange line in Fig. 2.10). For the three free fit parameter, we find $\gamma_{ab} = 2\pi \times 113(19)$ kHz, $OD_s = 5.2(2)$, and $\Omega_p = 2\pi \times 2.2(1)$ MHz. The value of Ω_p is higher than inferred from the intensity of the incoming pump field. This provides evidence that the atoms are indeed trapped behind the nanofiber and are exposed to a focused pump field (cf. Fig. 2.8).

The transmission window is broader than previously reported [38, 81]. To study

2.6. Calibration of the Pump Field

this in more detail, we reduce the impinging pump field intensity to $\sim 42 \mu\text{W}/\text{cm}^2$ and perform a point-wise scan of the signal detuning. For every δ , we turn on the signal laser within tens of nanoseconds. Then, we wait for $10 \mu\text{s}$ until the signal intensity has stabilized and the atomic ensemble is pumped into a quasi-steady state. After that, we average the transmitted power for $50 \mu\text{s}$ to find the transmission spectrum shown in Fig. 2.10(c). Using a Lorentzian fit, we find a maximum transmission of ~ 0.3 and a FWHM of $30(4)$ kHz, in agreement with previous results [38, 81].

From EIT to Autler-Townes Splitting

We now measure signal transmission spectra for various pump field intensities. Here, we scan the frequency of the signal laser again with a scanning speed of 120 MHz/ms over the atomic resonance. We see a narrow EIT transmission window in the signal absorption spectrum for small pump intensities (see Fig. 2.11).

When we increase the pump intensity, we observe a crossover from EIT into a doublet structure in the signal absorption profile. For high pump intensities, we see a splitting that is larger than the natural linewidth. Specifically, for a pump intensity of $I_0 \approx 34 \text{ mW}/\text{cm}^2$, we find a splitting of about $4.5\gamma_e \approx 23 \text{ MHz}$. Thus, we are clearly in the Autler-Townes regime [160, 168].

Autler-Townes Splitting

In spectroscopy, the Autler-Townes effect is described by the AC Stark effect. It predicts that an oscillating electric field, tuned close to the resonance of a spectral line, modifies the absorption and emission spectra of that spectral line. The field can split the two bare states of the transition into doublets or “dressed states” that are separated by the Rabi frequency [180].

In order to theoretically describe this effect, we study the semi-classical interaction of the pump field with an atom. Since the pump field couples near-resonantly to two levels, we treat the atom as a two-level system. We derive the dependence of the splitting of the bare states on the detuning $\Delta = \omega_p - \omega_{eg}$. Here, ω_{eg} is the resonance frequency of a two-level atom and ω_p is the frequency of the pump field. The Hamiltonian can be divided into a bare atom Hamiltonian \hat{H}_A plus an interaction Hamiltonian \hat{H}_{int} describing the interaction with the pump field. We assume $\omega_p \approx \omega_{eg}$ and apply the rotating wave approximation, i.e., we neglect terms that oscillate with $\omega_p + \omega_{eg} \gg \Delta$ [181]. In a frame that rotates with a frequency ω_p , the Hamiltonian of

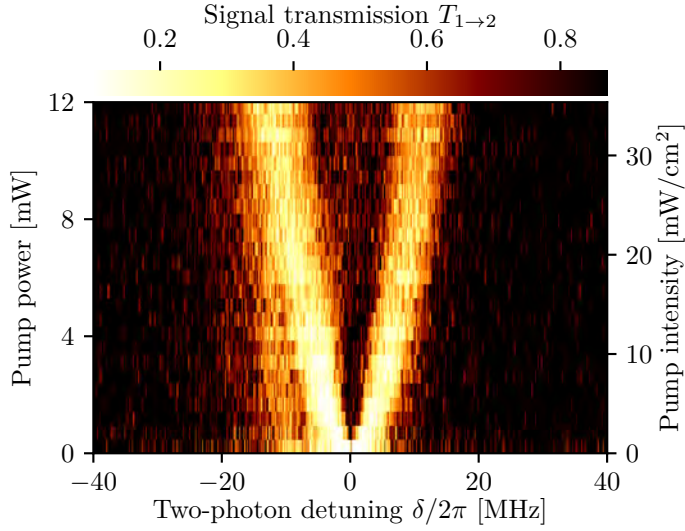


FIGURE 2.11: Signal transmission profiles as a function of δ and the pump intensity. For low pump intensities corresponding to low Ω_p , we observe a transmission window much smaller than the natural linewidth of $2\pi \times 5.225$ MHz, i.e., we see an EIT window. When we increase the pump intensity, we see a crossover to two clearly distinct dips that are split by more than the natural linewidth. Thus, we clearly observe the transition to the Autler-Townes regime.

the system is [7]

$$\hat{H} = \hat{H}_A + \hat{H}_{\text{int}} = -\hbar\Delta |e\rangle \langle e| + \frac{\hbar\Omega_p}{2} (|e\rangle \langle g| + |g\rangle \langle e|), \quad (2.13)$$

where $|g\rangle$ is the ground state and $|e\rangle$ is the excited state of the bare atom. Note that the Hamiltonian in Eq. 1.23 reduces to Eq. 2.13 when $\Omega_s = 0$ and $\delta = 0$. The energy eigenvalues of the Hamiltonian are [7]

$$E_{\pm} = -\frac{\hbar}{2} \cdot \left[\Delta \pm \sqrt{\Omega_p^2 + \Delta^2} \right]. \quad (2.14)$$

To probe the newly formed dressed states, we use a second laser, the signal laser. It

2.6. Calibration of the Pump Field

couples the split excited state to a third level, which is a ground state in our system. We scan the frequency of the second laser over the dressed state resonances while measuring its transmission. We now discuss two approximations of the eigenvalues. For small detunings, $\Delta \ll \Omega_p$, we find

$$E_{\pm} \approx \mp \frac{\hbar\Omega_p}{2} . \quad (2.15)$$

Here, the two dressed states are separated by $\hbar\Omega_p$, which we can use to calibrate Ω_p . For large detunings, $\Delta \gg \Omega_p$, we find

$$E_{\pm} \approx -\frac{\hbar}{2} \cdot [\Delta \pm \Delta] . \quad (2.16)$$

In this regime, we expect to find a one-photon resonance at $\delta \approx \Delta$, and a two-photon resonance at $\delta \approx 0$ MHz.

In the experiment, we set the pump intensity to $I_0 \approx 26$ mW/cm². The pump laser has a one-photon detuning Δ from the $|F = 4, m_F = -4\rangle \rightarrow |F' = 4, m_{F'} = -4\rangle$ transition and the signal laser a one-photon detuning Δ_s from the $|F = 3, m_F = -3\rangle \rightarrow |F' = 4, m_{F'} = -4\rangle$ transition (see Fig. 2.12(a)). We present the signal transmission $T_{1 \rightarrow 2}$ as a function of the detunings in Fig. 2.12(b). Specifically, we scan the one-photon detunings Δ and Δ_s around their respective resonances and measure the corresponding signal transmission. We find two clearly distinct absorption dips which shift with Δ . We want to ascertain Ω_p . First, we fit the two absorption peaks with Lorentzians and calculate the difference between the centers of the fits. Then, we fit this splitting with equation 2.14. The fit unveils $\Omega_p = 2\pi \times 16.35(11)$ MHz. Theoretically, based on the impinging pump intensity and neglecting the focusing effect of the nanofiber, we expect $\Omega_p \approx 2\pi \times 12$ MHz. Again, the detected Ω_p is significantly higher than expected from our simplified estimate. We conclude that the atoms are trapped behind the nanofiber, which has a focusing effect on the pump field (c.f. Fig. 2.8). To summarize, the Autler-Townes splitting provides us a tool to calibrate Ω_p , which we use in the following.

2.6.3 One-photon Detuning

Here, we discuss the influence of the one-photon detuning Δ on our system. First, we study with our numerical model the effect of Δ on the signal-to-noise ratio (SNR). We compare the maximal rate of the spontaneously Raman scattered photons in the

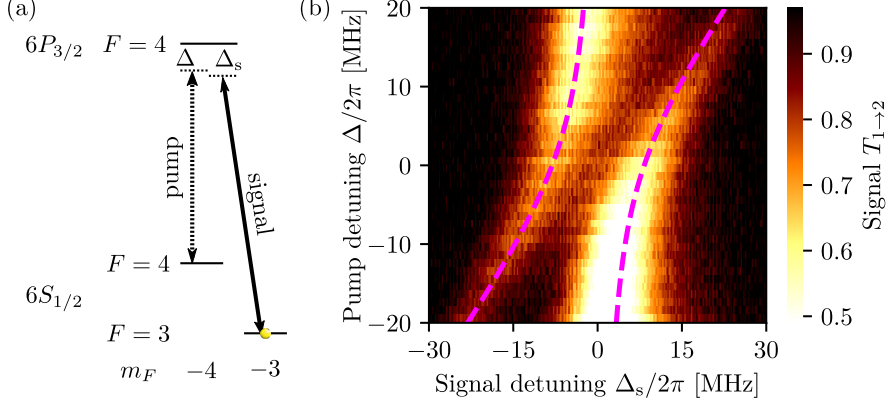


FIGURE 2.12: Autler-Townes splitting. (a) The pump laser and the signal laser are detuned by Δ and Δ_s from the excited state, respectively. (b) To calibrate the pump field Rabi frequency Ω_p , we record the signal transmission $T_{1 \rightarrow 2}$ as a function of Δ and Δ_s . We detect a doublet structure that shifts as expected for Autler-Townes splitting. A fit (magenta dashed lines) of the data yields $\Omega_p = 2\pi \times 16.4(1)$ MHz. This value is higher than expected for a plane wave, thus, evidencing the focusing effect of the nanofiber and that the atoms are trapped behind the nanofiber.

nanofiber-guided mode R_{sc} to the maximal rate of the photons that are coherently added to the signal field by the amplifier R_{coh} . Figure 2.13 shows the resulting

$$\text{SNR} = \frac{R_{coh}}{R_{sc}}. \quad (2.17)$$

As expected, this ratio increases with Δ . However, when increasing the detuning, the gain decreases and, eventually, is indistinguishable from the background noise. To take this into account, we compute

$$\text{SNR} = \frac{R_{coh}}{R_{sc} + R_b}, \quad (2.18)$$

where $R_b \approx 560$ kHz is the technical background count rate. This SNR reaches a maximum at $\Delta \approx 2\pi \times 100$ MHz.

We experimentally calibrate the one-photon detuning Δ . We red-detune the pump

2.6. Calibration of the Pump Field

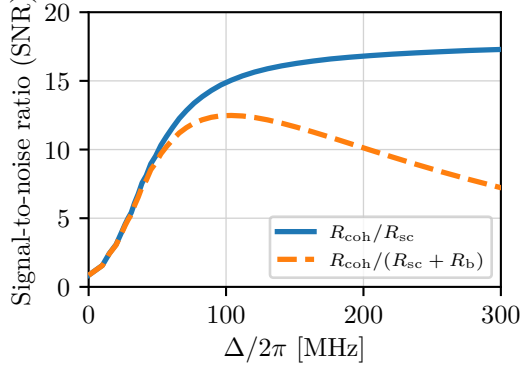


FIGURE 2.13: Model prediction for the signal-to-noise ratio (SNR) of the amplifier. We present the $\text{SNR} = R_{\text{coh}}/R_{\text{sc}}$, which increases monotonously with the one-photon detuning Δ (solid blue line). When also considering the technical background count rate, R_{b} , the SNR has its maximum at $\Delta \approx 2\pi \times 100$ MHz (dashed orange line).

laser from the $|6S_{1/2}, F = 4\rangle \rightarrow |6P_{3/2}, F' = 4\rangle$ transition, i.e., $\Delta < 0$. Then, we sweep the frequency of the signal laser over the one-photon and the two-photon resonance and detect the transmitted power (see Fig. 2.14(a)). We perform a fit using Eq. 1.15, Eq. 1.16, and Eq. 1.20. The fit works well when using γ_{ab} , OD_{s} , and Δ as free fit parameters. We find $\Delta = -2\pi \times 82.30(3)$ MHz, which fits our expectations based on the frequency difference we chose for the pump laser compared to the measurements in Fig. 2.10. The absolute value of the one-photon detuning $|\Delta|$ is close to 100 MHz and, therefore, a good compromise between a high SNR and a high signal gain.

Note that we define Δ with respect to the $|F = 4, m_F = -4\rangle \rightarrow |F' = 4, m_{F'} = -4\rangle$ -transition frequency (see Fig. 2.14(b)). Strictly speaking, the latter differs from the transition frequency of the $|F = 4, m_F = +4\rangle \rightarrow |F' = 4, m_{F'} = +4\rangle$ transition and, thus, the one-photon detuning Δ^+ from this transition frequency is not equal to Δ . However, the Zeeman splittings between adjacent magnetic sublevels of the ground state ($2\pi \times 0.35$ MHz/G) and the excited state ($2\pi \times 0.37$ MHz/G) are almost the same [154]. For the magnetic field strengths used in our experiment, we calculate a difference of the Zeeman shifted transition frequencies of at most $2\pi \times 1.1$ MHz, which is much smaller than $|\Delta| \approx 2\pi \times 82$ MHz. We can therefore make the approximation $\Delta^+ \approx \Delta$.

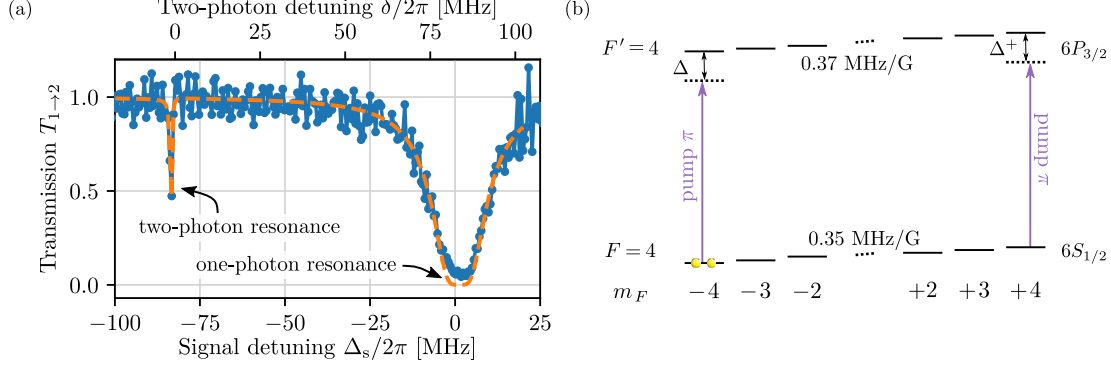


FIGURE 2.14: Calibration of the one-photon detuning Δ . (a) We sweep the frequency of the signal laser over the one-photon and the two-photon resonance and measure the transmitted signal power (blue dots). From a fit (dashed orange line), we infer a one-photon detuning of $\Delta = -2\pi \times 82.30(3)$ MHz. (b) Level scheme of the $|6S_{1/2}, F=4\rangle \rightarrow |6P_{3/2}, F'=4\rangle$ transition. The Zeeman splittings between adjacent magnetic sublevels of the ground state (0.35 MHz/G) and the excited state (0.37 MHz/G) are almost the same [154]. Hence, for the magnetic field strengths used in our experiment, we can make the approximation $\Delta^+ \approx \Delta$.

2.7 Signal Field Rabi Frequency

In this section, we discuss the signal field Rabi frequency Ω_s . The signal field is fiber-guided and has an evanescent field around the nanofiber. Atoms trapped close to the nanofiber have a finite temperature. Hence, they move in the trap and, thus, within the evanescent field. Therefore, we have to consider a distribution of Rabi frequencies Ω_s . First, we discuss theoretical calculations of Ω_s , and then, we present measurements of the effective Ω_s of the atomic ensemble.

2.7.1 Theoretical Calculations

Here, we study the radial dependency of Ω_s theoretically. We model the signal field as an evanescent field around the nanofiber. The atoms are trapped in the radial potential shown in Fig. 2.2. Already in the motional ground state, the atomic wavefunction has a significant radial extent. Consequently, the atoms “see” a substantial distribution of various Ω_s . Moreover, hotter atoms are further away from the surface of the nanofiber

2.7. Signal Field Rabi Frequency

and, therefore, for them Ω_s is lower. Note that this is a simplified model because, e.g., we neglect the coupling between the atomic spin and the motion of the atom in the trap [80].

For our study, we compute the first $\nu = 50$ eigenvalues E_ν and the corresponding eigenvectors $\psi_\nu(r)$ of the radial trapping potential. We assume that the atomic distribution over the eigenvalues E_ν follows a Boltzmann distribution [182]

$$p(E_\nu) = Z_c^{-1} e^{-E_\nu/k_B T}, \quad Z_c := \sum_\nu e^{-E_\nu/k_B T}, \quad (2.19)$$

where T is the temperature of the atomic ensemble, k_B is the Boltzmann constant, and p is the probability of finding an atom in a state with energy E_ν . First, we assume a typical temperature of $T = 30 \mu\text{K}$ [150] and study Ω_s for various nanofiber-guided signal field powers P_s . For every P_s , we compute the radial intensity distribution of the signal field around the nanofiber, from which we infer $\Omega_s(r)$. The probability that $\Omega_s(r)$ occurs is given by the probability to find an atom at a distance r . We use Eq. 2.1 to calculate the probability densities of the radial position of the atoms $p_\nu(r)$. The probability density of Ω_s is given by

$$p(\Omega_s(r)) = \sum_\nu p_\nu(r) p(E_\nu). \quad (2.20)$$

For various P_s , we present these probability densities in Fig. 2.15. As expected, for higher P_s , the most probable signal Rabi frequency $\Omega_{s,0}$ is shifting to higher Ω_s . The width of the distribution $\Delta\Omega_s$ is getting broader, but the factor $\Omega_{s,0}/\Delta\Omega_s$ is constant.

Next, we discuss the influence of T on the distribution of Ω_s . In Fig. 2.16(a), we present the occupation probabilities $p(E_\nu)$ of atoms in states with energies E_ν . We consider various temperatures between $T = 1 \mu\text{K}$ and $T = 100 \mu\text{K}$. For $T = 1 \mu\text{K}$, the occupation of the ground state $\nu = 1$ is more than three orders of magnitude higher than for state $\nu = 2$, i.e., almost all atoms are in the motional ground state. For higher temperatures, the probability of finding atoms in higher states increases. In Fig. 2.16(b), we present the corresponding distributions of Ω_s for $P_s = 10 \text{ pW}$. For $T = 1 \mu\text{K}$, we essentially find the same spread of Ω_s around $2\pi \times 1.6 \text{ MHz}$ as for 10 pW in panel (a) because the position and the momentum in the motional ground state are not fixed and have a variance. For higher temperatures of the atomic ensemble, the distribution of Ω_s gets significantly broader.

In our three level system, the two-photon Rabi frequency Ω_{2p} is a crucial parameter.

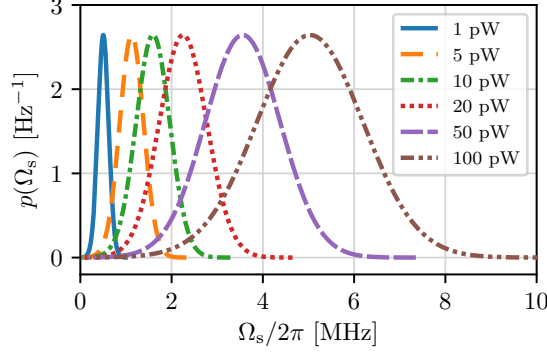


FIGURE 2.15: Probability densities of Ω_s for various nanofiber-guided signal field powers P_s . We assume a temperature of the atomic ensemble of $T = 30 \mu\text{K}$. For higher P_s , the most probable signal Rabi frequency $\Omega_{s,0}$ is higher, and the width of the distribution $\Delta\Omega_s$ gets broader. However, the factor $\Omega_{s,0}/\Delta\Omega_s$ is constant.

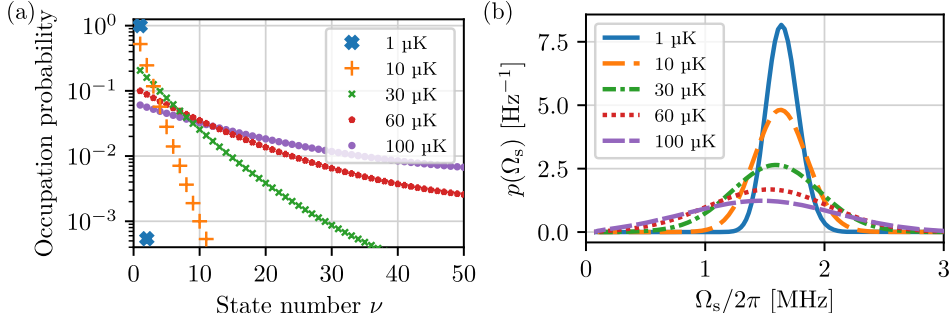


FIGURE 2.16: Dependence of Ω_s on the temperature of the atomic ensemble T . (a) Occupation probabilities of the eigenvalues E_ν in the radial trapping potential. For $T = 1 \mu\text{K}$, almost all atoms are in the motional ground state. For higher temperatures, we find more atoms also in higher states of the trapping potential. (b) Probability densities of Ω_s for various temperatures for $P_s = 10 \text{ pW}$. As expected, for higher T , the most probable Ω_s is lower, and the distribution of Ω_s gets broader.

Since Ω_{2p} is proportional to Ω_s , also Ω_{2p} has a distribution (c.f. Eq. 1.22). When we turn on the pump laser, all Rabi oscillations start with the same phase. Then, the hotter

2.7. Signal Field Rabi Frequency

the atomic ensemble, the broader the distribution of Ω_s and the faster the dephasing of the oscillations. Moreover, the most probable Ω_s is lower because hotter atoms are, on average, further away from the surface of the nanofiber. We can neglect these effects if the distribution of Ω_s is sufficiently narrow, i.e., $\Omega_{s,0}/\Delta\Omega_s \gg 1$. However, for $T = 1 \mu\text{K}$, we find in our system $\Omega_{s,0}/\Delta\Omega_s \approx 5$, which we consider not much larger than one. Hence, even for atoms in the motional ground state, we expect a damping of optical Rabi oscillations with a fiber-guided light field.

2.7.2 Experimental Exploration Using EIT

Now, we discuss our experimental attempts to measure the signal field Rabi frequency Ω_s of the atomic ensemble. We can only measure the mean signal field Rabi frequency $\overline{\Omega}_s$. Our theoretical calculations show that $\overline{\Omega}_s$ is ~ 1.07 times smaller than $\Omega_{s,0}$, which we discussed in the last section. We note that $\overline{\Omega}_s$ and $\Omega_{s,0}$ show the same scaling with the power of the signal field and the temperature of the atomic ensemble.

Here, we use a similar setup as presented in [81]. However, here we create dressed states with the signal field and probe them with the pump field. The signal and pump field propagate as running waves from port 1 to port 2 through the nanofiber. They have orthogonal polarizations. At the location of the atoms, the signal field is σ^- polarized and the pump field is π polarized. After the nanofiber, a polarization filter suppresses the signal field. We measure the transmitted power of the pump field with the SPCMs. We tune the signal laser on resonance and measure the absorption of the pump field under EIT conditions. Hence, compared to Sec. 2.6.2, we interchanged the roles of the laser fields.

We measure the transmission spectrum of the pump field and perform a fit with Eq. 1.20. In Fig. 2.17, we present the results for $\overline{\Omega}_s$ as a function of P_s . We see that $\overline{\Omega}_s$ increases with P_s . However, the data is noisy, and we find large error bars. We attribute this to a high background level resulting from insufficient suppression of the signal field. From Eq. 1.8, we infer our fit function

$$\overline{\Omega}_s = A\sqrt{P_s}, \quad (2.21)$$

where A is an amplitude that we use as a free fit parameter. We find an acceptable agreement of the fit with the experimental data for $A = 2\pi \times 143(5) \text{ kHz/pW}^{1/2}$.

For typical signal field powers of $P_s \approx 10 \text{ pW}$, no EIT window is visible in the pump transmission spectrum. However, from the fit in Fig. 2.17, we infer $\overline{\Omega}_s = 2\pi \times$

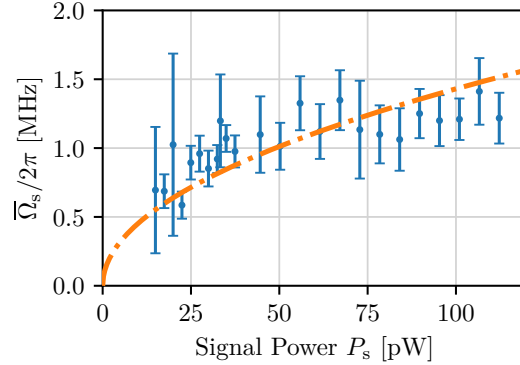


FIGURE 2.17: Effective signal field Rabi frequency $\bar{\Omega}_s$ of the atomic ensemble. We tune the signal laser on resonance and measure transmission spectra of the pump field under EIT conditions. We infer $\bar{\Omega}_s$ for various signal field powers P_s , and perform a fit that agrees with the experimental data. However, due to the large error bars, clear statements on $\bar{\Omega}_s$ are difficult.

0.45(2) MHz at this power. This is significantly lower than our expectation of $\bar{\Omega}_s \approx 2\pi \times 1.6$ MHz, which is based on the theoretical calculations of the last section. The divergence could arise because of heating of the atoms by the two laser fields or repulsive light-induced dipole forces exerted by the laser fields onto the nanofiber-trapped atoms. We also note that the calibration of the signal power in the nanofiber is challenging and we cannot rule out high systematic errors. In conclusion, based on the results of the theoretical calculations and the experimental investigation, we expect that the mean signal field Rabi frequency $\bar{\Omega}_s$ is between $2\pi \times 0.45$ MHz and $2\pi \times 1.6$ MHz for $P_s = 10$ pW.

Chapter 3

Experimental Demonstration of Non-Reciprocal Amplification

In this chapter, we experimentally study non-reciprocal Raman amplification in our system. First, we discuss the evolution of the amplification. In particular, we experimentally analyze the amplifier noise as well as the amplifier bandwidth. Furthermore, we show that the non-reciprocity is maintained when the signal field propagates simultaneously in both directions through the nanofiber. Finally, we study the scaling of the gain with the number of atoms and present measurements of gains up to 10.

3.1 Non-Reciprocal Amplification

Here, we experimentally investigate the evolution and the directionality of Raman amplification in our system. We prepare atoms on only one side of the nanofiber using degenerate Raman cooling (see Sec. 2.2). In this step, we apply an offset magnetic field of ~ 0.5 G along the quantization axis $+z$. The remaining atoms are cooled close to the motional ground state and pumped to the state $|6S_{1/2}, F=4, m_F=-4\rangle$ [155] (see Fig. 3.1(a)). Then, we ramp the offset magnetic field to ~ 7 G to stabilize the m_F -state [80]. As shown in Sec. 2.6.3, the one-photon detuning of the pump laser is $\Delta \approx -2\pi \times 82$ MHz. We tune the frequency of the signal laser to the light-shifted two-photon resonance

$$\delta^- + \delta_{\text{LS}} = 0 . \quad (3.1)$$

From the analysis presented in Sec. 2.6, we infer a pump field Rabi frequency of $\Omega_p \approx 2\pi \times 20$ MHz, and, therefore, $\delta_{\text{LS}} \approx 2\pi \times 1.2$ MHz (see Eq. 1.21). We estimate a signal

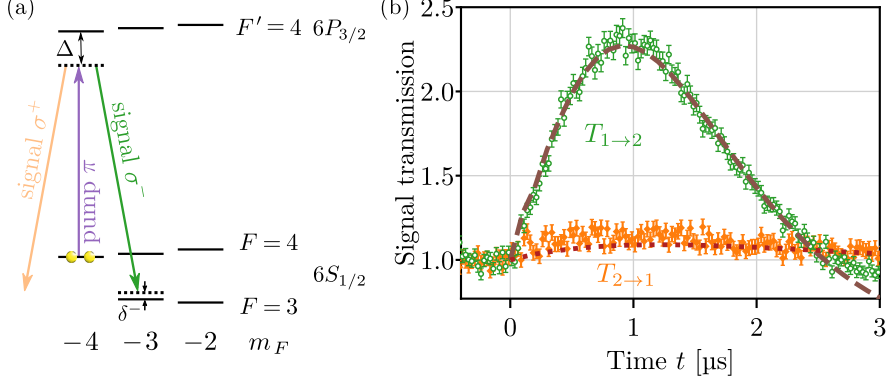


FIGURE 3.1: Non-reciprocal amplification. (a) Relevant energy levels in the presence of a magnetic offset field, applied along $+z$. We prepare the atoms in $|6S_{1/2}, F = 4, m_F = -4\rangle$. The pump field and the σ^- polarized signal field couple to a Λ -type scheme and drive two-photon Raman transitions. In contrast, the σ^+ probe field that propagates in the $2 \rightarrow 1$ direction does not couple to this system and, therefore, is not amplified. (b) Measured signal transmissions $T_{1 \rightarrow 2}$ (green circles) and $T_{2 \rightarrow 1}$ (orange diamonds) as a function of time t . At $t = 0 \mu\text{s}$, we switch on the pump field. Then, $T_{1 \rightarrow 2}$ increases up to $2.38(6)$. In contrast, $T_{2 \rightarrow 1}$ is always less than $1.20(5)$. The experimental data agrees with theoretical calculations (dashed brown line and red dotted line, see main text for details). The signal gain persists up to $t \approx 2.5 \mu\text{s}$. In this time interval, we clearly see non-reciprocal amplification.

field Rabi frequency of $\Omega_s \approx 2\pi \times 1.6 \text{ MHz}$ for atoms in the minimum of the trapping potential (see Sec. 2.7.1).

First, we only switch on the signal field, which does not couple to the atoms in state $|6S_{1/2}, F = 4, m_F = -4\rangle$ (see Fig. 3.1(a)). We take a reference measurement of the optical power transmitted through the waveguide, yielding $P_s \approx 9 \text{ pW}$. At a time $t = 0 \mu\text{s}$, we switch on the pump field. In conjunction with the signal field, this establishes the Raman coupling. In Fig. 3.1(b), we present the signal transmission when the signal beam propagates from port 1 to port 2 (green circles). Here, about ~ 1400 atoms were trapped and coupled to the guided mode of the nanofiber. Initially, the signal transmission increases linearly. Then, it reaches a maximum of $2.38(6)$ after $t = 0.9 \mu\text{s}$. This is only slightly less than a quarter of a period of the two-photon Rabi

3.1. Non-Reciprocal Amplification

oscillations at a frequency of

$$\Omega_{2p} = \frac{\Omega_p \Omega_s}{2\Delta} \approx 2\pi \times 200 \text{ kHz} . \quad (3.2)$$

In total, we detect a transmission above one for about 2.5 μs . From $t \approx 2.5 \mu\text{s}$ onwards, we observe two-photon loss, i.e., $T_{1 \rightarrow 2} < 1$. We infer from these observations that our system operates in a partially coherent regime.

We compare the evolution of the signal transmission to numerical calculations (c.f. Sec. 1.3.3). We find a good agreement between the experimental data and the theoretical computations for the parameters presented in Tab. 1.1, see dashed brown line in Fig. 3.1(b). In this table, we also show that these values are in reasonable agreement with independent estimates.

When measuring in the other direction, i.e., in the $2 \rightarrow 1$ direction, we only observe a small signal transmission increase (see orange diamonds in Fig. 3.1(b)). The maximal transmission is $T_{2 \rightarrow 1} = 1.20(5)$, which is clearly smaller than the maximal transmission in the $1 \rightarrow 2$ direction. The residual increase predominantly arises from a small coupling of the signal field to the $|F = -3, m_F = -3\rangle \rightarrow |F' = 4, m_{F'} = -4\rangle$ transition due to its $\sim 8\%$ overlap with σ^- polarization. In the simulations, we change OD_s and Ω_s by a factor of $0.08/0.92 \approx 0.087$ to account for the weaker coupling of the signal field to the atoms, see dotted red line in Fig. 3.1(b). This also results in a lower Ω_s and, therefore, we detect gain in the $2 \rightarrow 1$ direction for slightly longer times than in the $1 \rightarrow 2$ direction.

As shown in Fig. 3.1(b), the theoretical calculations agree well with the measured transmission. The residual deviations might arise because of the multi-level structure of cesium. Moreover, strictly speaking, the output field is a sum of the transmitted signal light and the spontaneously scattered light of the pump field. We have investigated this effect theoretically by adding the spontaneously scattered light to the signal output field. Then, the calculations still qualitatively reflect the measurement of the evolution of the signal transmission. If we also change the parameters (e.g., the number of atoms) by less than 5%, we again get a good agreement. Thus, we usually neglect the spontaneously scattered light and refer to the output field as signal transmission. This assumption is also motivated by the fact that the scattering of the pump field into the nanofiber is more than 10 times weaker than the signal gain in the $1 \rightarrow 2$ direction (see also next section). In the $2 \rightarrow 1$ direction it is about 5 times weaker. Hence, in both directions it is justified to refer to the output field as signal transmission. We conclude

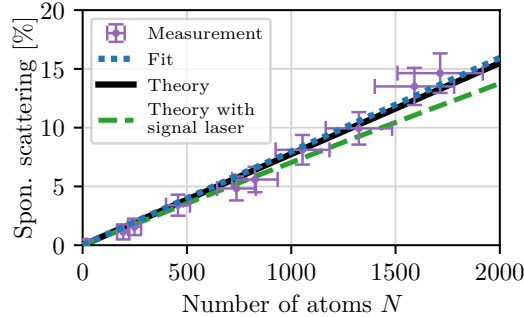


FIGURE 3.2: Spontaneous Raman scattering of the pump field into the $1 \rightarrow 2$ mode of the nanofiber as a function of the number of atoms N . We use the bare signal transmission for the normalization. The measured data (purple dots) agrees well with the theoretical prediction (solid black line). With a linear fit (dotted blue line), we find that the spontaneous Raman scattering changes the measured gain by at most 12%. When we perform the theoretical calculations with a signal laser tuned to the two-photon resonance, we find less spontaneous scattering into the nanofiber (dashed green line).

that we clearly observe non-reciprocal Raman gain.

3.2 Spontaneous Raman Scattering of the Pump Field

Noise is an important characteristic of any amplifier [63]. In our system, this noise is dominated by the spontaneous Raman scattering of the pump field. We explore this experimentally without the signal field. In Fig. 3.2, we present a measurement of the pump photons that are scattered in the nanofiber and guided to port 2 as a function of the number of atoms N . Here, we average the detected photon count rate \bar{R}_{sc} between $t = 0.7 - 1.2 \mu\text{s}$ after switching on the pump field. Although the signal laser was off during the measurement, we use the photon count rate of the bare signal transmission, detected at times $t < 0 \mu\text{s}$ in Fig. 3.1(b), for the normalization of the measurement. Hence, we see how many photons the spontaneous scattering can add to the signal photons without any two-photon coupling.

3.2. Spontaneous Raman Scattering of the Pump Field

We compare the experimental data with a theoretical estimate. We use our numerical model without a signal laser ($\Omega_s = 0$) to calculate the population of the excited state. With Eq. 1.28, we calculate the average one-photon scattering rate $\gamma_e \bar{\rho}_{ee}$ between $t = 0.7 - 1.2 \mu\text{s}$. Then, the photon detection rate is given by

$$\bar{R}_{\text{sc}} = \alpha \beta^+ \gamma_e \bar{\rho}_{ee} , \quad (3.3)$$

where $\beta^+ = 0.01 \cdot (7/15 \cdot 0.5 + 8/15 \cdot 0.92) \approx 0.7\%$ is the fraction of light that is scattered in the guided $1 \rightarrow 2$ mode and $\alpha = 0.225$ is an attenuation factor describing the losses in the detection setup and the detector efficiency. We have experimentally verified that the scattering of the pump field due to, e.g., imperfections of the nanofiber into the nanofiber mode is much smaller than the other photon rates in the nanofiber. Therefore we neglect it. The photon detection rate of the guided signal field is given by

$$R_s = \alpha \frac{P_s}{E_{\text{photon}}} = \alpha \frac{P_s \lambda}{hc} , \quad (3.4)$$

where $P_s = 9 \text{ pW}$ is the power of the signal field, E_{photon} is the energy of one photon, and $\lambda = 852 \text{ nm}$ is the wavelength of the signal field. In Fig. 3.2, we present the ratio \bar{R}_{sc}/R_s , which agrees well with the experimental data.

Next, we perform a fit of the experimental data with a linear function and find a slope of $0.0080(2)\%$. The theory predicts a slope of $\sim 0.0078\%$, which is in agreement with the experimental data within the error bars. We conclude that for 1400 atoms, the spontaneous Raman scattering of the pump field can increase the output photon rate at port 2 with a signal laser propagating in the $1 \rightarrow 2$ direction by at most 12% even without any signal gain. We repeat our numerical calculations with a signal laser tuned to the two-photon resonance, i.e., with the settings we use to measure non-reciprocal amplification.. Here, atoms can make two-photon transitions, and fewer atoms contribute to the spontaneous Raman scattering signal. The slope for these settings is only $\sim 0.0070\%$ (see dashed green line in Fig. 3.2). Based on this analysis, we conclude that the directional gain discussed in the last section does not arise from spontaneous Raman scattering but originates from a directional two-photon light-matter coupling.

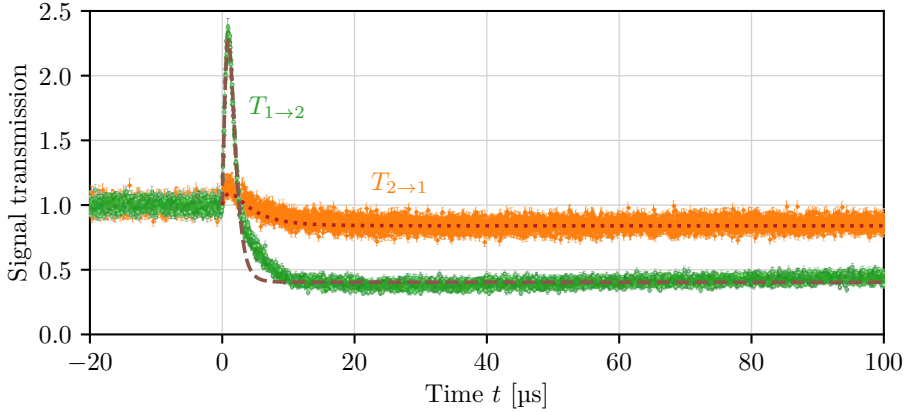


FIGURE 3.3: Measured signal transmissions $T_{1 \rightarrow 2}$ (green circles) and $T_{2 \rightarrow 1}$ (orange diamonds) as a function of time. We switch the pump field on at $t = 0 \mu\text{s}$. Then, $T_{1 \rightarrow 2}$ increases while $T_{2 \rightarrow 1}$ remains nearly unchanged. At $t \approx 2.5 \mu\text{s}$, the signal gain turns into two-photon absorption. This agrees well with our theoretical calculations (lines). Then, at even longer times, the signal transmission increases again because atoms are lost from the Λ system.

3.3 Signal Transmission Dynamics

In this section, we discuss the evolution of the signal transmission in a larger time interval. In Fig. 3.3, we present the measured signal transmissions $T_{1 \rightarrow 2}$ and $T_{2 \rightarrow 1}$ between $t = -20 \mu\text{s}$ and $t = 100 \mu\text{s}$. Before switching on the pump laser ($t < 0 \mu\text{s}$), the transmitted signal powers are constant. We use this bare transmission signal as a reference, i.e., we set $T_{1 \rightarrow 2} = T_{2 \rightarrow 1} = 1$ for $t < 0 \mu\text{s}$. At $t = 0 \mu\text{s}$, we switch on the pump field. Then, we observe non-reciprocal amplification up to $t \approx 2.5 \mu\text{s}$. Subsequently, the signal field is attenuated due to two-photon absorption, and we detect a transmission < 1 in both directions. After $t \approx 10 \mu\text{s}$, we reach a quasi-steady state. At much longer times, the signal transmission increases again because atoms are pumped to uncoupled states or heated out of the trap. Between $t = 20 - 50 \mu\text{s}$, we detect an average quasi-steady-state transmission in the $1 \rightarrow 2$ direction of $T_{1 \rightarrow 2}^{\text{ss}} = 0.39(2)$, which corresponds to $\text{OD} = -\ln(T_{1 \rightarrow 2}^{\text{ss}}) = 0.95(6)$. In the $2 \rightarrow 1$ direction, we see much less absorption in the signal transmission. Specifically, we find $T_{2 \rightarrow 1}^{\text{ss}} = 0.85(4)$

3.4. Reconfiguration of the Amplifier

corresponding to $\text{OD} = -\ln(T_{2 \rightarrow 1}^{\text{ss}}) = 0.17(5)$.

We now discuss the agreement between the measured transmissions and our theoretical model. We manually optimize the model parameters to match the theory to the experimentally obtained transmissions. Theory and experiment agree excellently for short time intervals where we see amplification. For larger time intervals, the match is still reasonable but less good. These deviations might arise because our theory ignores the full multilevel structure of cesium. Hence, we neglect the loss of population out of the Λ -system due to excitation and decay to other cesium levels. Also, we do not consider light-induced dipole forces exerted by the pump laser field onto the nanofiber-trapped atoms. These forces may excite a center-of-mass oscillation of the atomic ensemble with a period of $6 \mu\text{s}$, estimated from the inverse of the calculated radial trap frequency of $2\pi \times 160 \text{ kHz}$. Finally, we neglect the Zeeman-state dependence of the trapping potential [183]. This effect could lead to excess heating and a concomitant change in the coupling strength of the atom to the nanofiber-guided mode.

3.4 Reconfiguration of the Amplifier

In order to reverse the direction in which the light is amplified, we optically pump the atoms from state $|6S_{1/2}, F = 4, m_F = -4\rangle$ to state $|6S_{1/2}, F = 4, m_F = +4\rangle$. We lose $\sim 40\%$ of the atoms at this pumping stage (see Sec. 2.2). As illustrated in Fig. 3.4, now only the σ^+ polarized laser field propagating in the $2 \rightarrow 1$ directions in conjunction with the pump field form a relevant Λ system. Due to dipole selection rules, the Λ coupling of the σ^- polarized signal field that propagates in the $1 \rightarrow 2$ direction is negligible.

We tune the frequency of the signal laser to the light-shifted two-photon resonance ($\delta^+ = -\delta_{\text{LS}}$). At $t = 0 \mu\text{s}$, we turn on the pump field and measure the evolution of the signal transmission. Now, we see a clear amplification of the signal field in the $2 \rightarrow 1$ directions. In the $1 \rightarrow 2$ directions, we observe almost no amplification. We compare the measured transmissions to theoretical computations with our model parameters presented in Tab. 1.1. However, to account for the atom loss in the preparation of state $|F = 4, m_F = +4\rangle$, we perform the calculations with the experimentally obtained atom number of $N = 852$. We find a good agreement between the experimental data and the theoretical expectation. This demonstrates the reconfigurability of our amplifier by preparing the atoms in another spin state.

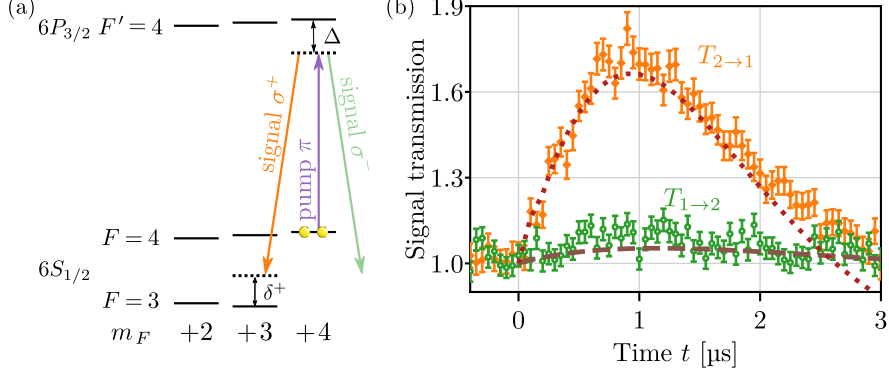


FIGURE 3.4: Reconfiguration of the non-reciprocal amplification direction. (a) Relevant energy levels in the presence of a magnetic offset field, applied along $+z$. We prepare the atoms in state $|6S_{1/2}, F=4, m_F=+4\rangle$. The pump field and the σ^+ polarized signal field couple to a Λ -type scheme. No Λ coupling occurs for the σ^- polarized signal field. (b) The signal transmissions $T_{1\rightarrow 2}$ (green circles) and $T_{2\rightarrow 1}$ (orange diamonds) as a function of time t . At $t=0\ \mu\text{s}$, we turn on the pump field. In contrast to the measurement shown in Fig. 3.1(b), now $T_{2\rightarrow 1}$ is amplified, whereas the gain of $T_{1\rightarrow 2}$ is almost negligible. This confirms the atomic spin-controlled reconfiguration of the non-reciprocal amplifier.

3.5 Frequency Dependency of the Signal Transmission

Here, we study the frequency dependence of the Raman coupling. We measure the signal transmission and, first, analyze the spectrum in the regime of quasi-steady-state two-photon absorption. Then, we also investigate the gain spectrum and infer the amplifier bandwidth.

3.5.1 Steady-State Absorption

In Fig. 3.5, we present the detected quasi-steady-state signal transmission T^{ss} , averaged between $t=20-50\ \mu\text{s}$, as a function of the two-photon detuning δ^- . In this time interval, the signal field is attenuated due to two-photon absorption.

When we prepare the atoms initially in state $|6S_{1/2}, F=4, m_F=-4\rangle$, we see a clear absorption dip in the transmission spectrum of the signal field that propagates

3.5. Frequency Dependency of the Signal Transmission

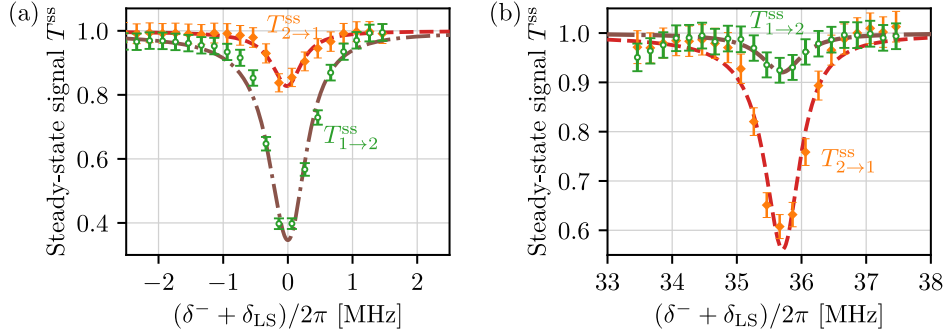


FIGURE 3.5: Measured quasi-steady-state signal transmissions, averaged between $t = 20 - 50 \mu\text{s}$, as a function of the two-photon detuning δ^- . (a) When we prepare the atoms in $|F = 4, m_F = -4\rangle$, we observe a strong two-photon absorption resonance in $T_{1 \rightarrow 2}^{\text{ss}}$ (green circles). A fit using steady-state equations yields $\gamma_{\text{ab}}^{1 \rightarrow 2} = 2 \times 0.47(3)$ MHz and $\delta^- + \delta_{\text{LS}} = 2\pi \times 0.00(1)$ MHz (dash-dotted brown line). For $T_{2 \rightarrow 1}^{\text{ss}}$, we see much less absorption (orange diamonds and dashed red line). (b) When we prepare the atoms in $|F = 4, m_F = +4\rangle$, the absorption reverses, and we observe more absorption in the $2 \rightarrow 1$ direction than in the $1 \rightarrow 2$ direction. A fit yields $\gamma_{\text{ab}}^{2 \rightarrow 1} = 2 \times 0.51(8)$ MHz and $\delta^- + \delta_{\text{LS}} = 2\pi \times 35.71(3)$ MHz (dashed red line). The two-photon resonance condition occurs at different values of δ^- , due to the presence of an offset magnetic field.

in the $1 \rightarrow 2$ direction (see green circles in Fig. 3.5(a)). This dip indicates the two-photon resonance of the atoms that are dressed by the pump field. We fit the spectrum using the steady-state Eq. 1.20 in combination with Eq. 1.15 and Eq. 1.16. Our free fit parameters are OD, γ_{ab} , and Δ . The fit agrees well with the detected transmission spectrum. We obtain $\gamma_{\text{ab}}^{1 \rightarrow 2} = 2 \times 0.47(3)$ MHz and find the strongest absorption at $\delta^- + \delta_{\text{LS}} = 2\pi \times 0.00(1)$ MHz. When we send the signal field in the $2 \rightarrow 1$ direction, we also observe a faint resonance. However, the steady-state absorption is much weaker (see orange diamonds in Fig. 3.5(a)). The residual absorption results from the $\sim 8\%$ overlap of the signal field with σ^- polarization.

Next, we prepare the atoms in state $|6S_{1/2}, F = 4, m_F = +4\rangle$ and measure signal transmission spectra in both directions. Now, the ratio of the absorptions reverses (see Fig. 3.5(b)). We detect much more absorption in the $2 \rightarrow 1$ direction than in the $1 \rightarrow 2$ direction. We perform a fit of the $2 \rightarrow 1$ signal transmission spectrum and find

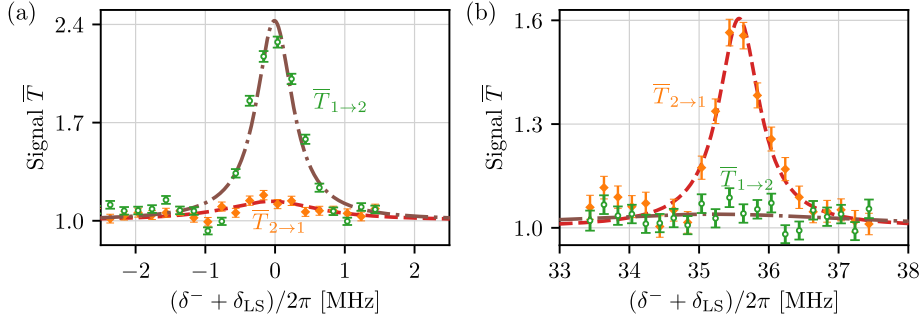


FIGURE 3.6: Signal gain spectrum. (a) We prepare the atoms in state $|F = 4, m_F = -4\rangle$ and measure \bar{T} in both directions. We find a clear gain peak only in the $1 \rightarrow 2$ direction (green circles). A fit yields a width of $\gamma_{1 \rightarrow 2} = 2\pi \times 0.78(6)$ MHz (dash-dotted brown line). In the $2 \rightarrow 1$ direction, the signal transmission is almost unchanged (orange diamonds and dashed red line). (b) We prepare the atoms in $|F = 4, m_F = +4\rangle$. Now we find a clear gain peak only in the $2 \rightarrow 1$ direction (orange diamonds). Here, a fit (dashed red line) shows that $\gamma_{2 \rightarrow 1} \approx \gamma_{1 \rightarrow 2}$, confirming that the bandwidth of the amplifier is the same in both directions.

$\gamma_{ab}^{2 \rightarrow 1} = 2 \times 0.51(8)$ MHz, which agrees with $\gamma_{ab}^{1 \rightarrow 2}$ within the error bars. Due to the magnetic field induced Zeeman shifts of the energy levels, the two-photon resonance condition is met at another detuning δ^- . We detect the strongest absorption at $\delta^- + \delta_{LS} = 2\pi \times 35.71(3)$ MHz. From the frequency difference of the dressed state resonances, we infer an offset magnetic field of $7.29(1)$ G, which is in reasonable agreement with our expectations.

3.5.2 Gain Spectrum and Amplifier Bandwidth

In this section, we study the gain bandwidth, which is one of the key amplifier features [94]. We scan the two-photon detuning δ^- over the light shifted two-photon resonance and detect the signal transmission. First, we prepare the atoms in state $|F = 4, m_F = -4\rangle$ and detect the signal gain, defined as the mean signal transmission \bar{T} between $t = 0.7 - 1.2$ μ s (see Fig. 3.6(a)). In the $1 \rightarrow 2$ direction, we find a clear gain peak, whereas, in the $2 \rightarrow 1$ direction, we see almost no amplification.

The gain bandwidth is given by the dependence of the gain coefficient $g(\delta)$ on the frequency detuning δ of the incident light from an atomic resonance (cf. Eq. 1.1). In

3.6. Simultaneously Probing from Both Directions

the case of atoms, $g(\delta)$ is proportional to the spectral line shape of a transition [94]. We treat the atoms as effective two-level systems and, thus, fit the gain peaks in both directions with a Lorentzian function as exponent [128, 184]

$$\bar{T} = \exp \left[\frac{A}{(\delta^- + \delta_{\text{LS}})^2 + (\gamma/2)^2} \right], \quad (3.5)$$

where γ is the width of the two-photon resonance. Here, the amplitude A is proportional to the optical depth and positive if the transmission is above 1, i.e., the transmitted field is amplified. We find a good agreement of the fit with the measured data and obtain a width of the gain peak in the $1 \rightarrow 2$ direction of $\gamma_{1 \rightarrow 2} = 2\pi \times 0.78(6)$ MHz (see Fig. 3.6). The ratio of the amplitudes of the gain in the $2 \rightarrow 1$ direction and in the $1 \rightarrow 2$ direction $A_{2 \rightarrow 1}/A_{1 \rightarrow 2} \approx 0.087$ fits to our expectations based on the impurities of the polarizations of the signal field.

Now, we prepare the atoms in state $|F = 4, m_F = +4\rangle$ and detect \bar{T} as a function of δ^- . In the $1 \rightarrow 2$ direction, we observe no gain peak (see Fig. 3.6(b)). In the $2 \rightarrow 1$ direction, gain is evident at the light shifted resonance at $\delta^- \approx 2\pi \times 35.5$ MHz. We perform a fit using Eq. 3.5 and find $\gamma_{2 \rightarrow 1} = 2\pi \times 0.8(1)$ MHz. We conclude that within the error bars, the widths of the resonances agree with each other, and we infer that the bandwidth of the amplifier is ~ 800 kHz

3.6 Simultaneously Probing from Both Directions

Following the discussion in [97, 98], we study if our amplifier is a non-reciprocal device or if it falls in the category of a non-reciprocal-controlled device. As stated in [97], in the latter device, a forward propagating field controls the propagation of the forward as well as the backward propagating fields, whereas the backward propagating field controls neither direction. This is usually the case in non-reciprocal schemes that are based on non-linearities. Such devices only work as, e.g., an isolator for forward and backward propagating fields that are not coincident in time. When the fields simultaneously propagate through the device, the transmission is reciprocal.

We experimentally explore whether the non-reciprocal amplification prevails when simultaneously sending the signal fields into both directions through the nanofiber. We prepare the atoms in $|F = 4, m_F = -4\rangle$ and follow the same procedure as for the experiment presented in Sec. 3.1. In Fig. 3.7, we plot the resulting evolution of the signal transmissions. Qualitatively, we observe the same non-reciprocal amplification

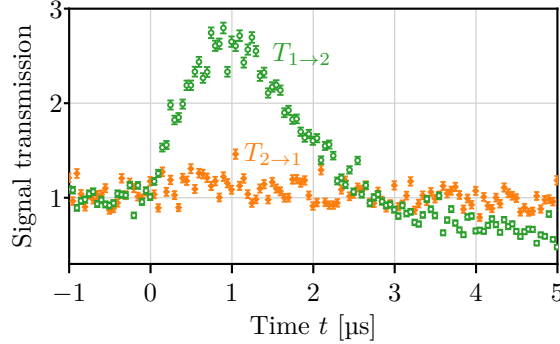


FIGURE 3.7: Non-reciprocal Raman amplification when simultaneously probing from both directions. We send signal fields in both directions at the same time through the amplifier and detect the transmissions simultaneously. We see much more gain in $T_{1 \rightarrow 2}$ (green circles) than in $T_{2 \rightarrow 1}$ (orange diamonds). Hence, we clearly observe non-reciprocal amplification also under these conditions.

as shown in Fig. 3.1. We measure a maximal signal transmission of ~ 2.6 in the $1 \rightarrow 2$ direction. In the $2 \rightarrow 1$ direction, the signal transmission is almost unchanged. Since non-reciprocity also prevails when sending the signal fields simultaneously in both directions, we conclude that our amplifier is not only non-reciprocally controlled but a fully functional non-reciprocal device.

3.7 Scaling of the Gain with the Number of Atoms

We discuss the scaling of the signal gain with the number of atoms N that are trapped in the nanofiber-based optical dipole trap. We study two regimes, the linear and the superlinear regime. In the linear regime, a photon, on average, stimulates the emission of only one additional photon. In contrast, in the superlinear regime, one photon can induce the emission of several stimulated photons.

3.7.1 Linear Regime

Here, we measure the evolution of the signal transmission in the $1 \rightarrow 2$ direction $T_{1 \rightarrow 2}(t)$ with the same settings as in Sec. 3.1. In Fig. 3.8, we present the signal gain for

3.7. Scaling of the Gain with the Number of Atoms

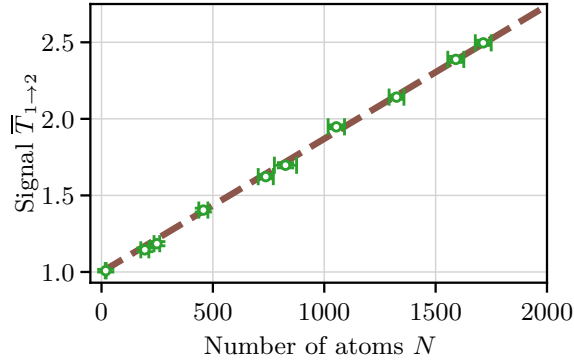


FIGURE 3.8: Scaling of the signal gain with the number of atoms N . The maximal gain, defined as the average transmission $\bar{T}_{1 \rightarrow 2}$ between $t = 0.7 - 1.2 \mu\text{s}$, is on the order of 2. Hence, on average, every photon only induces the emission of one stimulated photon, and we can approximate the scaling with a linear function. A fit agrees well with the data, confirming this approximation.

various N , where the signal gain is defined as the average transmission $\bar{T}_{1 \rightarrow 2}$ between $t = 0.7 - 1.2 \mu\text{s}$.

The maximum signal transmission is on the order of 2. Thus, upon the passage through the atomic ensemble, a signal photon will, on average, only induce the emission of one stimulated photon. We, therefore, assume that the gain scales linearly with the number of atoms. A fit with a linear function agrees with the data confirming this assumption. From the slope of the fit, we infer a gain per atom of $0.87(1) \%$.

3.7.2 Demonstration of Superlinear Scaling

We investigate the scaling of the signal gain with N for the regime where the maximal total signal transmission is much larger than 2. Here, upon the passage through the atomic ensemble, an incident signal photon can induce the emission of several stimulated photons. Moreover, stimulated photons can induce the emission of additional stimulated photons. This can be interpreted as collective interaction, and linear approximations are no longer valid. An exponential scaling with N should then become apparent as long as the power of the probe field stays below saturation upon its passage through the atomic ensemble.

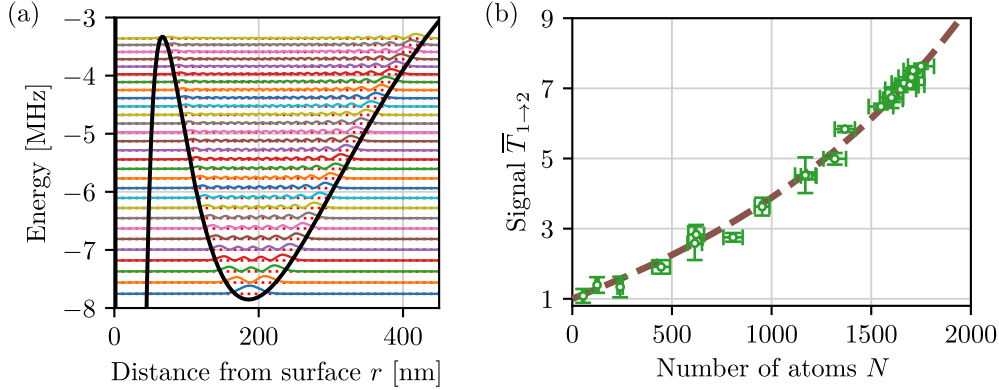


FIGURE 3.9: Superlinear scaling of the gain with the number of atoms. (a) Total radial trapping potential for the changed powers of the trapping light fields (black line). We find a local trapping minimum at $r \approx 185$ nm. We also show the energy of the motional states (dotted red lines) and the corresponding probabilities of finding an atom at a given radial distance from the surface (solid colored lines). (b) Signal gain as a function of the number of trapped atoms N . A fit (dashed brown line) agrees very well with the data (green circles). This confirms that the gain grows superlinearly with N .

To increase the signal gain, we increase the OD on the two-photon transition by using a higher pump field Rabi frequency of $\Omega_p \approx 2\pi \times 36$ MHz. Furthermore, after loading the atoms into the nanofiber-based dipole trap, we ramp the total power of the red-trapping light field from ~ 2.4 mW up to ~ 2.9 mW. As a consequence, the atoms are attracted closer to the nanofiber, and the optical depth per atom, OD_s , is higher compared to the parameters discussed in Tab. 1.1. Specifically, for the present trapping powers, we calculate a local radial trapping minimum at a distance of ~ 185 nm away from the nanofiber surface (see Fig. 3.9(a)).

We prepare the atoms in state $|F = 4, m_F = -4\rangle$ and measure $T_{1 \rightarrow 2}(t)$. In Fig. 3.9(b), we present the signal gain for various N , where the signal gain is given by the average transmission $\bar{T}_{1 \rightarrow 2}$ between $t = 0.285 - 0.405$ μs . Theoretically, we infer from Eq. 1.19 that the number of stimulated emitted photons grows exponentially with N . Such a scaling can also be found in topological frameworks where the non-reciprocal gain can

3.8. Measurements of Gains up to 10

grow exponentially with the number of cavities [185]. We fit the data using

$$\bar{T}_{1 \rightarrow 2}(N) = e^{\lambda N} + kN, \quad (3.6)$$

where λ is the growth rate of the exponential function and k takes the spontaneous Raman scattering into account. We assume that the latter grows linearly with N , which is fulfilled for sufficiently low OD. With an independent measurement, we find $k \approx 0.00126$ for the current settings. The fit agrees excellently with the measured gain, and we obtain $\lambda \approx 1 \%$ for our only fit parameter. This confirms that the gain grows superlinearly with N . In particular, we infer that the number of stimulated photons grows exponentially with the number of atoms N . This indicates collective light-matter interaction in the present setting.

3.8 Measurements of Gains up to 10

We use the same settings as in the previous section, i.e., we prepare the atoms at a radial distance of ~ 185 nm away from the nanofiber surface (see Fig. 3.9(a)). We trap $N \approx 1700$ atoms in state $|F = 4, m_F = -4\rangle$ and measure the transmission in both directions (see Fig. 3.10). Also for these settings, we observe much more gain in the $1 \rightarrow 2$ direction than in the $2 \rightarrow 1$ direction. Specifically, between $t = 0.285 - 0.405$ μ s, we detect an average signal transmission of $\bar{T}_{1 \rightarrow 2} = 7.2(3)$ in the $1 \rightarrow 2$ direction, and only $\bar{T}_{2 \rightarrow 1} = 1.55(1)$ in the $2 \rightarrow 1$ direction. We conclude that also in the regime of superlinear scaling with N , the amplifier is non-reciprocal.

To further increase the gain, we reduce the power of the signal field to $P_s \approx 4$ pW. Then, we observe signal transmissions up to ~ 10 (see Fig. 3.11). The transmission remains above 1 for about 2 μ s. Subsequently, the signal field is absorbed, and we measure a quasi-steady-state transmission of $T_{2 \rightarrow 1}^{\text{ss}} = 0.11(7)$ between $t = 20 - 40$ μ s. This corresponds to an OD on the light shifted two-photon resonance of $\text{OD} = 2.2(9)$.

We conclude that the non-reciprocal amplification of the signal field is scalable to larger gains. We can increase the gain by increasing the OD or reducing the signal field power. In our experiment, the total OD on the $|6S_{1/2}, F = 4\rangle \rightarrow |6P_{3/2}, F' = 5\rangle$ cycling transition was ~ 100 , but in similar systems, much higher ODs of up to ~ 1000 have been reported [186, 187], which would allow the realization of much higher gains.

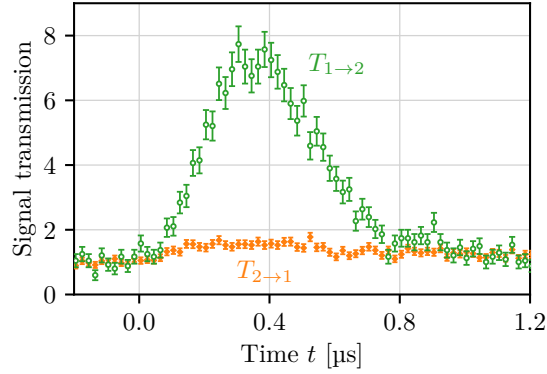


FIGURE 3.10: Non-reciprocal signal field transmission in the regime of multiple stimulated emission of photons. We find gains up to 7 in one direction, whereas in the other direction, the transmission is only about 1.55. Therefore, we conclude that also in this regime, the amplifier is non-reciprocal.

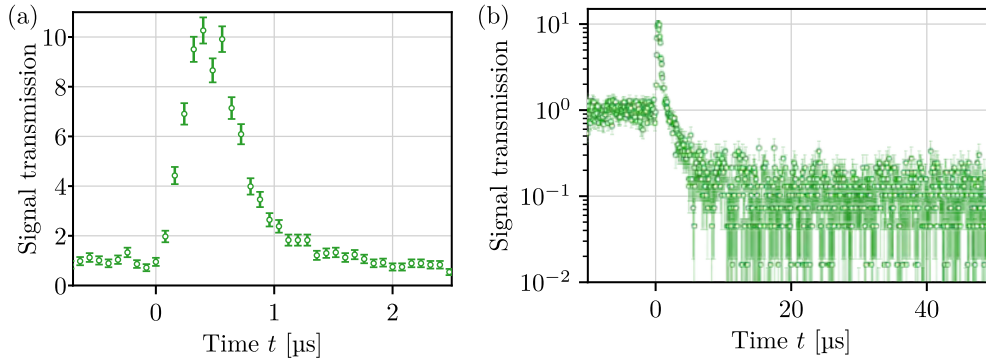


FIGURE 3.11: Signal gains of up to ~ 10 . By reducing the signal field power and increasing the OD, we can increase the signal gain. (a) We measure a maximal signal field transmission of $T_{1 \rightarrow 2} = 10.3(5)$. (b) From the quasi-steady-state transmission between $t = 20 - 40 \mu\text{s}$, we infer $\text{OD} = 2.2(9)$

Chapter 4

Magnetic-Field Free Operation of the Non-Reciprocal Amplifier

Magnetic-field free non-reciprocal amplifiers are highly sought devices [188], e.g., because they can be operated close to superconducting qubits [189] and they are compatible with semiconductor integrated-circuits [190]. In this chapter, we demonstrate that non-reciprocity is maintained in our system without an externally applied magnetic field. In this case, we have to stabilize the initial atomic spin states with another mechanism against depopulation and dephasing due to spin-motion coupling [80] and stray magnetic fields. We discuss our method and the corresponding setup to achieve this stabilization in the following. Also, we present our experimental results of magnetic-field free non-reciprocal amplification.

4.1 Experimental Setup and Method

Here, we discuss our method to stabilize the atomic spin state using tensor light shifts (TLS). First, we discuss the relevant atomic level scheme and calculate the energy shifts of the m_F states when we apply TLSs using a π -polarized light field. Then, we present the experimental setup and the measurement sequence.

4.1.1 Atomic Level Scheme

We use an additional laser that we term TLS laser to stabilize the atomic spin state. The TLS laser field is π -polarized at the location of the atoms and has a detuning Δ_{TLS} from the $|6S_{1/2}, F = 4\rangle \rightarrow |6P_{1/2}, F'' = 3\rangle$ transition at a wavelength of 894 nm (see Fig. 4.1(a)). As outlined in the next section, the laser field induces scalar and

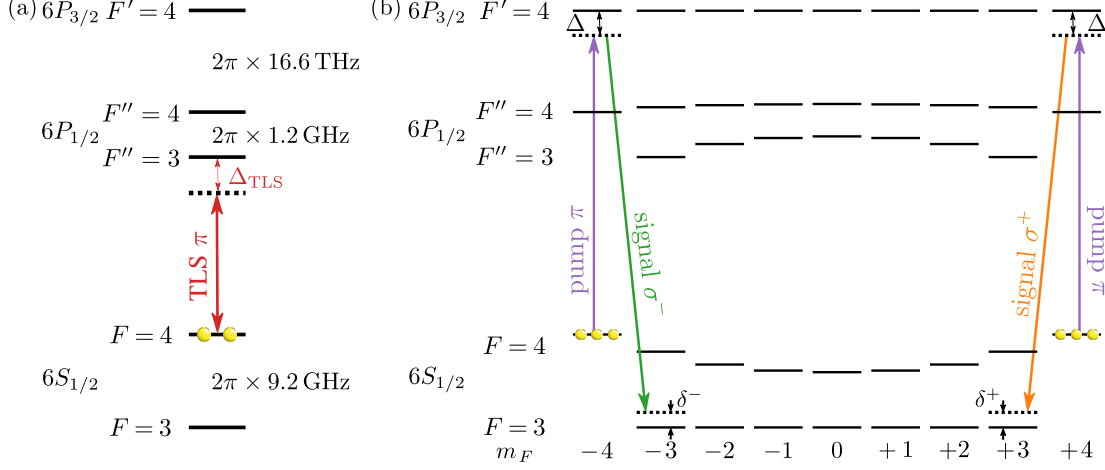


FIGURE 4.1: Relevant energy levels without applied offset magnetic field. (a) Hyperfine structure of the $|6S_{1/2}\rangle \rightarrow |6P_{1/2}\rangle$ transition. The π -polarized tensor light shift (TLS) beam is detuned by Δ_{TLS} from the $|6S_{1/2}, F=4\rangle \rightarrow |6P_{1/2}, F''=3\rangle$ transition. (b) The TLS beam induces TLS to the $|6S_{1/2}, F=4\rangle$ manifold and the $|6P_{1/2}\rangle$ manifold. Moreover, it prepares the atoms in a statistical mixture of the $|6S_{1/2}, F=4, m_F = \pm 4\rangle$ levels. When we implement our Λ systems, we see that the two-photon detunings, δ^+ and δ^- , coincide.

tensor light shifts to the Zeeman sublevels.

For detunings $\Delta_{\text{TLS}} \ll 2\pi \times 9.2$ GHz, the light shifts of the Zeeman substates of the $|6S_{1/2}, F=4\rangle$ state and the $|6P_{1/2}\rangle$ state are much larger than the light shifts of other states. In particular, we neglect the light shifts of the Zeeman substates of the $|6S_{1/2}, F=3\rangle$ state as well as the $|6P_{3/2}\rangle$ state. Crucially, the TLS is proportional to m_F^2 . When implementing our Λ systems, we see that the two-photon resonances now coincide, $\delta^+ = \delta^-$ (see Fig. 4.1(b)). During the state preparation, we pump the atoms from state $|6S_{1/2}, F=3\rangle$ to state $|6S_{1/2}, F=4\rangle$ with a repumping laser field tuned close to the $|6S_{1/2}, F=3\rangle \rightarrow |6P_{3/2}, F'=4\rangle$ transition. In combination with the TLS laser field, this pumps the atoms to the dark states $|6S_{1/2}, F=4, m_F = -4\rangle$ and $|6S_{1/2}, F=4, m_F = +4\rangle$. Note that the atoms are not in a superposition but in a statistical mixture of the levels $|6S_{1/2}, F=4, m_F = \pm 4\rangle$.

4.1.2 Calculation of the Tensor Light Shift

In this section, we discuss the calculations of the light shifts induced by the TLS laser field on the $|6S_{1/2}, F = 4\rangle$ manifold. This field has an amplitude \mathcal{E} and an angular frequency ω . We decompose the induced light shift into three components: the scalar, vector, and tensor light shift. Then, the total light shift is [191, 192]

$$\begin{aligned} \Delta E(F, m_F) = & -\alpha_F^S(\omega) |\mathcal{E}|^2 \\ & -\alpha_F^V(\omega) (i\mathcal{E}^* \times \mathcal{E})_z \frac{m_F}{F} \\ & -\alpha_F^T(\omega) \frac{(3|\mathcal{E}_z|^2 - |\mathcal{E}|^2)}{2} \left(\frac{3m_F^2 - F(F+1)}{F(2F-1)} \right). \end{aligned} \quad (4.1)$$

Here, α_F^S , α_F^V , and α_F^T are the scalar, vector, and tensor polarizabilities, respectively. These polarizabilities are independent of m_F and given by [192, 193]

$$\begin{aligned} \alpha_F^S(\omega) &= \sum_{F'} \frac{2\omega_{F'F} \left| \langle F || \hat{d} || F' \rangle \right|^2}{3\hbar (\omega_{F'F}^2 - \omega^2)}, \\ \alpha_F^V(\omega) &= \sum_{F'} (-1)^{F+F'+1} \sqrt{\frac{6F(2F+1)}{F+1}} \left\{ \begin{matrix} 1 & 1 & 1 \\ F & F & F' \end{matrix} \right\} \frac{\omega_{F'F} \left| \langle F || \hat{d} || F' \rangle \right|^2}{\hbar (\omega_{F'F}^2 - \omega^2)}, \\ \alpha_F^T(\omega) &= \sum_{F'} (-1)^{F+F'} \sqrt{\frac{40F(2F+1)(2F-1)}{3(F+1)(2F+3)}} \left\{ \begin{matrix} 1 & 1 & 2 \\ F & F & F' \end{matrix} \right\} \frac{\omega_{F'F} \left| \langle F || \hat{d} || F' \rangle \right|^2}{\hbar (\omega_{F'F}^2 - \omega^2)}, \end{aligned} \quad (4.2)$$

where the curly brackets are the Wigner 6-j symbols, $\omega_{F'F}$ is the frequency of a transition between a ground state F and an excited state F' , and $\langle F || \hat{d} || F' \rangle$ are the respective reduced dipole matrix elements.

We note that the equations for the dressed states discussed in Sec. 2.6.2 can also be used to calculate the total light shift. From Eq. 2.14, it follows that this shift is [7]

$$\Delta E(F, m_F) = - \sum_{F'} \frac{1}{2} \left[\Delta_{\text{TLS}} - \sqrt{\Omega_{F'F m_F' m_F}^2 + \Delta_{\text{TLS}}^2} \right], \quad (4.3)$$

where $\Omega_{F'Fm_{F'}m_F}$ is the Rabi frequency between the two sublevels $|F, m_F\rangle$ and $|F', m_{F'}\rangle$. In the case $|\Delta_{\text{TLS}}| \gg \Omega_{F'Fm_{F'}m_F}$, we can make the approximation [7]

$$\Delta E(F, m_F) \approx - \sum_{F'} \frac{1}{2} \left[\Delta_{\text{TLS}} - \Delta_{\text{TLS}} - \frac{\Omega_{F'Fm_{F'}m_F}^2}{2\Delta_{\text{TLS}}} \right], \quad (4.4)$$

$$= \sum_{F'} \frac{\Omega_{F'Fm_{F'}m_F}^2}{4\Delta_{\text{TLS}}}. \quad (4.5)$$

In our theoretical calculations of the total light shift, we obtain the same results with Eq. 4.1 and Eq. 4.5.

We use π polarization. Hence, the vector light shift vanishes, and because of dipole selection rules, the excited state magnetic quantum number is $m_{F'} = m_F$. In Fig. 4.2(a), we present the remaining total light shifts of the $|6S_{1/2}, F = 4\rangle$ manifold. We performed the calculations with $\Delta_{\text{TLS}} = -2\pi \times 90$ MHz and a TLS field intensity of $I_{\text{TLS}} = 380$ mW/cm² as employed in the experiment. We see that the $\pm m_F$ levels experience the same light shift and find the expected m_F^2 dependence.

We now study the dependence of the light shift on the detuning Δ_{TLS} . In Fig. 4.2(b), we present the results for the $|6S_{1/2}, F = 4, m_F = \pm 3\rangle$ levels and the $|6S_{1/2}, F = 4, m_F = \pm 4\rangle$ levels. Close to $\Delta_{\text{TLS}} = 0$ MHz, the $|m_F = \pm 4\rangle$ levels shift much less than the $|m_F = \pm 3\rangle$ levels. In our experiments, we red-detune the TLS laser to minimize the scattering rate of the TLS laser field. Specifically, at $\Delta_{\text{TLS}} = -2\pi \times 90$ MHz, we estimate that the difference of the light shifts between the $m_F = \pm 3$ levels and the $m_F = \pm 4$ levels is $\sim 2\pi \times 2$ MHz. This is sufficient to stabilize the m_F states against depopulation and dephasing due to spin-motion coupling [80] and spurious magnetic fields.

Next, we study the additional decoherence induced by the TLS laser field. Especially, the scattering of TLS laser field photons can lead to decoherence. We calculate the scattering rate of the TLS field for atoms in state $|F, m_F\rangle$ using [192]

$$R_{\text{sc}}^{\text{TLS}}(\omega) = \sum_{F''} \frac{\Gamma'' S_{F''Fm_{F''}m_F}^2}{1 + 4([\omega_{F''F} - \omega]/\Gamma)^2 + 2S_{F''Fm_{F''}m_F}^2}, \quad (4.6)$$

4.1. Experimental Setup and Method

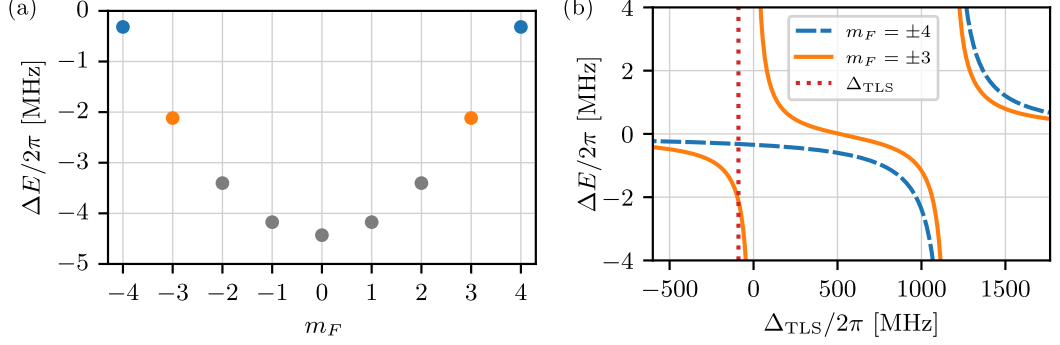


FIGURE 4.2: Total light shift of the Zeeman substates of the $|6S_{1/2}, F = 4\rangle$ manifold. We calculate the light shift for a π polarized laser field with an intensity of $I_{\text{TLS}} = 380 \text{ mW/cm}^2$. (a) Like in the experiment, we use $\Delta_{\text{TLS}} = -2\pi \times 90 \text{ MHz}$. The Zeeman substates shift proportional to m_F^2 . Consequently, $\pm m_F$ levels experience the same light shift. (b) Frequency dependence of the total light shift of the relevant Zeeman sublevels. Close to $\Delta_{\text{TLS}} = 0 \text{ MHz}$, the total light shifts ΔE of the $|6S_{1/2}, F = 4, m_F = \pm 3\rangle$ levels (solid orange line) are much larger than the light shifts of the $|6S_{1/2}, F = 4, m_F = \pm 4\rangle$ levels (dashed blue line). The dotted red line indicates the experimentally used detuning $\Delta_{\text{TLS}} \approx -2\pi \times 90 \text{ MHz}$.

where $\Gamma'' = 2\pi \times 4.561(6) \text{ MHz}$ [154] is the decay rate of the $6P_{1/2}$ state. Here, S is given by

$$S_{F''Fm_{F''}m_F} = \frac{\Omega_{F''Fm_{F''}m_F}}{\Gamma}. \quad (4.7)$$

In Fig. 4.3, we present the scattering rate of the TLS field as a function of Δ_{TLS} for $I_{\text{TLS}} = 380 \text{ mW/cm}^2$ and π polarization. We find one peak for atoms in state $|4, \pm 4\rangle$ and two peaks for atoms in state $|3, \pm 3\rangle$. At $\Delta_{\text{TLS}} \approx 0 \text{ MHz}$, the scattering rate for atoms in $|4, \pm 3\rangle$ is much larger than for atoms in $|4, \pm 4\rangle$ because in the case of π polarization, the $|4, \pm 4\rangle \rightarrow |3, \pm 3\rangle$ transition is a dipole-forbidden transition. For our detuning $\Delta_{\text{TLS}} = -2\pi \times 90 \text{ MHz}$, we estimate a residual scattering rate for atoms in state $|4, \pm 4\rangle$ of $R_{\text{sc}}^{\text{TLS}} \approx 2\pi \times 2 \text{ kHz}$. This is small enough not to perturb the amplification measurements significantly.

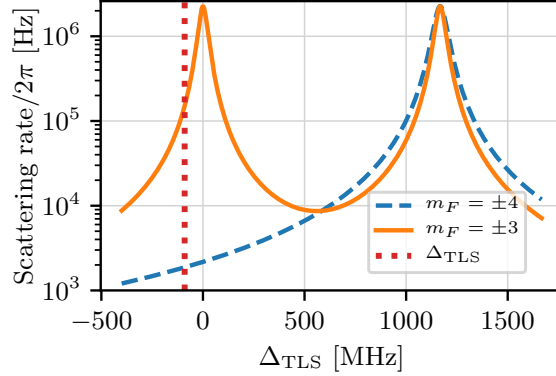


FIGURE 4.3: Scattering rate of the TLS laser field as a function of Δ_{TLS} . We present the scattering rate for atoms in the relevant states $|F = 4, m_F = \pm 4\rangle$ (dashed blue line) and $|F = 3, m_F = \pm 3\rangle$ (solid orange line). At $\Delta_{\text{TLS}} = -2\pi \times 90$ MHz (dotted red line), we expect that the decoherence due to scattering of photons at a rate of ~ 2 kHz for atoms in state $|4, \pm 4\rangle$ is negligible.

4.1.3 Experimental Setup

Here, we discuss the relevant setup of the TLS laser field. We lock the frequency of the TLS laser to the cesium $|6S_{1/2}, F = 4\rangle \rightarrow |6P_{1/2}, F'' = 3\rangle$ transition using saturation spectroscopy. Then, we red-detune the frequency of the laser beam by ~ 90 MHz with an AOM and send it to the main setup. Before and after each measurement, we check the power of the TLS beam. At a time scale of three hours, i.e., the typical duration of a measurement, the power of the TLS field stays constant.

As illustrated in Fig. 4.4, we use a quarter-wave plate and a half-wave plate for a wavelength of 894 nm to set the polarization of the TLS field to π polarization in front of the nanofiber. We expect that the deviations from π polarization at the location of the atoms are negligible (cf. Sec. 2.6.1). We use a lens¹ to control the beam diameter. At the location of the atoms, it is ~ 2 mm. We superimpose the TLS beam with the pump beam using a bandpass filter² with a center wavelength of 852 nm. The TLS field has a wavelength of 894 nm and is, therefore, reflected by the filter. Due to

¹Thorlabs, LA1509-B

²Thorlabs, FB850-40

4.1. Experimental Setup and Method

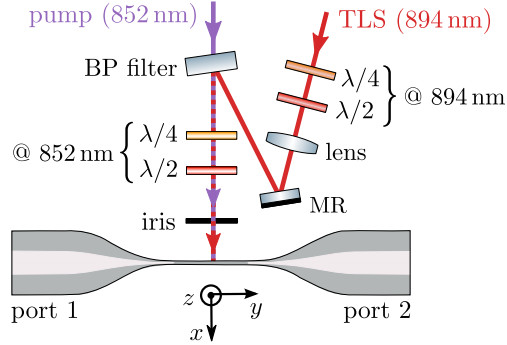


FIGURE 4.4: Overlap of the TLS beam with the Raman pump beam. We use a BP filter with a center wavelength of ~ 852 nm to superimpose the TLS beam with the pump field. Waveplates and a lens in front of this filter control the polarization and the beam size of the TLS beam at the location of the atoms. (BP filter, bandpass filter; $\lambda/2$, half-wave plate; $\lambda/4$, quarter-wave plate; MR, mirror)

interference effects, the filter modifies the beam shape. Consequently, the shape is no longer perfectly Gaussian. Moreover, the beam shape of the pump field is slightly modified because we use the filter under an angle. These beam shapes lead to varying intensities of the fields at the location of the atoms, resulting in a variation of light shifts and pump field Rabi frequencies along the atom array. Eventually, this could yield higher dephasing rates in the gain measurements. A suitable notch filter might solve these problems.

After the bandpass filter, the superimposed pump and TLS beams propagate through a quarter-wave plate and a half-wave plate for a wavelength of 852 nm, which we use to control the pump polarization. In front of the chamber, an iris blocks unwanted stray light. Then, the beams impinge on the atoms from the side. We note that we can tune the polarization of the pump field and the TLS field to π polarization in front of the chamber better than 99%. However, the polarizations at the location of the atoms may differ slightly from π polarization, e.g., due to a possible birefringence of the window of the vacuum chamber and the presence of the nanofiber.

4.1.4 Experimental Sequence

Here, we discuss the experimental sequence that we employ in our magnetic-field free amplification measurements. First, we prepare the atoms in state $|6S_{1/2}, F = 4, m_F = -4\rangle$ on one side of the nanofiber (see Sec. 2.2). After the preparation, the magnetic field is ~ 0.5 G. Within 7 ms, we ramp the magnetic field to ~ 0 G. Residual magnetic stray fields and spin-motion coupling [80] lead to a distribution of the atomic population over all Zeeman states of the $|6S_{1/2}, F = 4\rangle$ manifold.

We turn on the signal laser, which does not couple to the atoms in state $|6S_{1/2}, F = 4\rangle$. We wait until its transmitted power has stabilized. Then, we detect the bare transmission of the signal field through the nanofiber. Subsequently, we turn on the TLS laser and the repumper. This pumps the atoms within 100 μ s into an incoherent mixture of the states $|6S_{1/2}, F = 4, m_F = -4\rangle$ and $|6S_{1/2}, F = 4, m_F = +4\rangle$ because those are dark states for the TLS laser. To prepare the atoms exclusively in either state $|m_F = -4\rangle$ or state $|m_F = +4\rangle$, we apply the external preparation laser field that propagates in the $+z$ direction simultaneously with the TLS beam (see Fig. 2.5). When the preparation laser field is σ^\pm polarized, the dark-state condition for atoms in $m_F = \mp 4$ is lifted. The atoms experience strong recoil heating and are removed from the trap. Meanwhile, the atoms in $|F = 4, m_F = \pm 4\rangle$ are nearly unaffected.

After the atomic state preparation, within tens of nanoseconds, we switch off the preparation laser and the repumping laser, and switch on the pump laser. Note that the TLS laser is still on. Then, we detect the dynamics of the transmitted power of the signal field. After that, we turn off all lasers and take a background measurement.

4.2 Experimental Results

Here, we experimentally study the signal transmission in the magnetic-field free case while stabilizing the atomic spin state with the TLS laser field. First, we discuss the steady-state signal transmission spectra and analyze the two-photon resonances. Then, we investigate the time interval where the signal field is amplified. Specifically, we show that we can control the direction of amplification by manipulating the atomic spin state.

4.2.1 Transmission Spectrum

We now measure the signal field transmission spectra without an externally applied offset magnetic field while stabilizing the spin-polarization of the atoms using TLSs.

4.2. Experimental Results

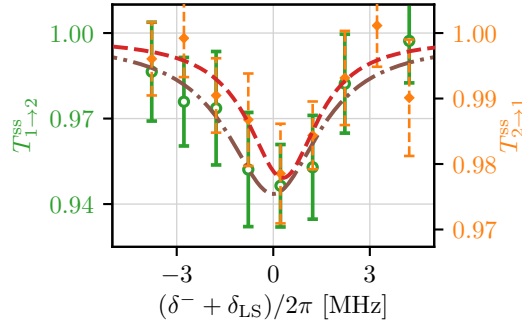


FIGURE 4.5: Measured quasi-steady-state signal transmission in the magnetic-field free scheme. In both propagation directions, we observe the two-photon resonance at the same value of δ^- . From a fit, we infer $\delta^- + \delta_{\text{LS}} = 2\pi \times 0.0(2)$ MHz for $T_{1 \rightarrow 2}^{\text{ss}}$ (dash-dotted brown line and green circles). For $T_{2 \rightarrow 1}^{\text{ss}}$, we find $\delta^- + \delta_{\text{LS}} = 2\pi \times 0.3(2)$ MHz (dashed red line and orange diamonds). The resonances are separated by much less than their respective linewidths. From the difference in the resonance frequencies, we infer a residual magnetic field of $0.06(6)$ G.

In Fig. 4.5, we present the quasi-steady-state signal transmissions $T_{1 \rightarrow 2}^{\text{ss}}$ and $T_{2 \rightarrow 1}^{\text{ss}}$, averaged between $t = 20 \mu\text{s}$ and $t = 50 \mu\text{s}$, as a function of $\delta^- + \delta_{\text{LS}}$. This corresponds to a time interval in which the signal field is attenuated due to two-photon absorption.

In both directions, we see clear dips in the transmission spectrum, unveiling the two-photon resonances of the atoms. We perform a fit using the steady-state Eq. 1.20 in combination with Eq. 1.15 and Eq. 1.16. In the $1 \rightarrow 2$ direction, we find a two-photon resonance at $\delta_{1 \rightarrow 2}^- + \delta_{\text{LS}} = 2\pi \times 0.0(2)$ MHz and infer a decoherence rate of $\gamma_{\text{ab}} = 2\pi \times 3.4(5)$ MHz from the fit. In the $2 \rightarrow 1$ direction, the resonance occurs at $\delta_{2 \rightarrow 1}^- + \delta_{\text{LS}} = 2\pi \times 0.3(2)$ MHz, and the decoherence rate is $\gamma_{\text{ab}} = 2\pi \times 2.6(6)$ MHz. Crucially, the resonances coincide within their linewidths.

We calculate the residual magnetic field using

$$B_z^{\text{res}} = \frac{\delta_{2 \rightarrow 1}^- - \delta_{1 \rightarrow 2}^-}{\delta E_4 - \delta E_3} = \frac{0.3(3) \text{ MHz}}{8 \cdot 0.35 \text{ MHz/G} + 6 \cdot 0.35 \text{ MHz/G}} = 0.06(6) \text{ G} , \quad (4.8)$$

where δE_4 is the difference of the Zeeman shifts of the $|6S_{1/2}, F = 4, m_F = \pm 4\rangle$ states and δE_3 is the difference of the Zeeman shifts of the $|6S_{1/2}, F = 4, m_F = \pm 3\rangle$ states.

The residual magnetic field of 0.06(6) G is negligible in that it cannot explain the observed non-reciprocal amplification. The ground state decoherence rates are larger than those obtained in the measurements with offset magnetic fields. This might result from the laser system, which was exchanged between the measurements of non-magnetic and magnetic directional amplification. Moreover, spurious scattering of the TLS laser can lead to more decoherence. Theoretically, the scattering rate of the TLS laser is negligible, but a significant scattering rate can arise when the TLS field is not perfectly π polarized. Also, the beam profiles of the TLS field and the pump field are not Gaussian due to the bandpass filter that we use to combine the two fields. These inhomogeneities lead to a distribution of TLSs and pump field Rabi frequencies. Consequently, the two-photon resonance is broader, and the dephasing of the two-photon Rabi oscillations is faster.

4.2.2 Demonstration of Magnetic-Field Free Non-Reciprocal Amplification

Here, we study the dynamics of the signal transmission in a time interval where we expect to detect Raman amplification. We use TLSs to stabilize the atomic spin state and tune the frequency of the signal laser to the light-shifted two-photon resonance at $\delta_{1 \rightarrow 2}^- + \delta_{\text{LS}} = 2\pi \times 0.0$ MHz. First, we prepare atoms in a statistical mixture of the states $|6S_{1/2}, F=4, m_F=+4\rangle$ and $|6S_{1/2}, F=4, m_F=-4\rangle$. We measure the evolution of the signal transmission and present the mean signal transmissions, $\bar{T}_{1 \rightarrow 2}$ and $\bar{T}_{2 \rightarrow 1}$, averaged from $t = 0.15 - 0.9$ μs in Fig. 4.6 (grey bars). In these measurements, the average gain is smaller than $\sim 10\%$, limited by the smaller number of atoms due to a less efficient state preparation as well as by the $\sim 5\times$ larger width of the two-photon resonance (see above). Within the error bars, we find the same signal gain in both directions. Thus, the amplification is reciprocal.

To restore the non-reciprocal gain, we now prepare atoms selectively in only one of the two outermost Zeeman states, i.e., either state $|F=4, m_F=-4\rangle$ or state $|F=4, m_F=+4\rangle$. When we prepare the atoms in state $|F=4, m_F=-4\rangle$, we only observe gain in the $1 \rightarrow 2$ direction (red bars). In contrast, when we prepare the atoms only in state $|F=4, m_F=+4\rangle$, we see gain only in the $2 \rightarrow 1$ direction (blue bars). This confirms that the atomic spin rather than an applied magnetic field breaks the reciprocity. By preparing the atomic spin state, we can control the direction of amplification.

4.2. Experimental Results

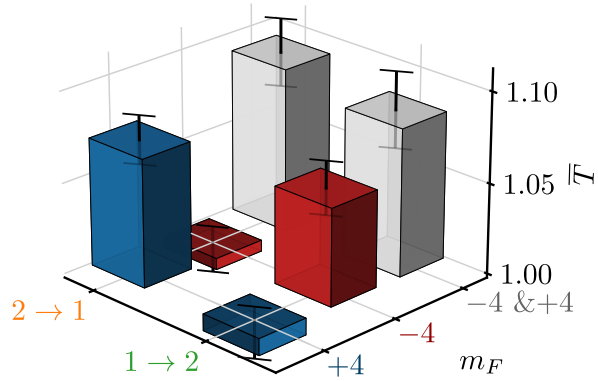


FIGURE 4.6: Spin-controlled magnetic field-free amplification. First, we prepare the atoms in a statistical mixture of the states $|F = 4, m_F = -4\rangle$ and $|F = 4, m_F = +4\rangle$ of the $6S_{1/2}$ manifold (grey bars). Here, signal gain occurs in both directions, and the amplification is reciprocal. If the atoms populate only state $|F = 4, m_F = -4\rangle$, we observe gain exclusively in the $1 \rightarrow 2$ direction (red bars). When we prepare the atoms in state $|F = 4, m_F = +4\rangle$, signal amplification occurs only in the $2 \rightarrow 1$ direction (blue bars).

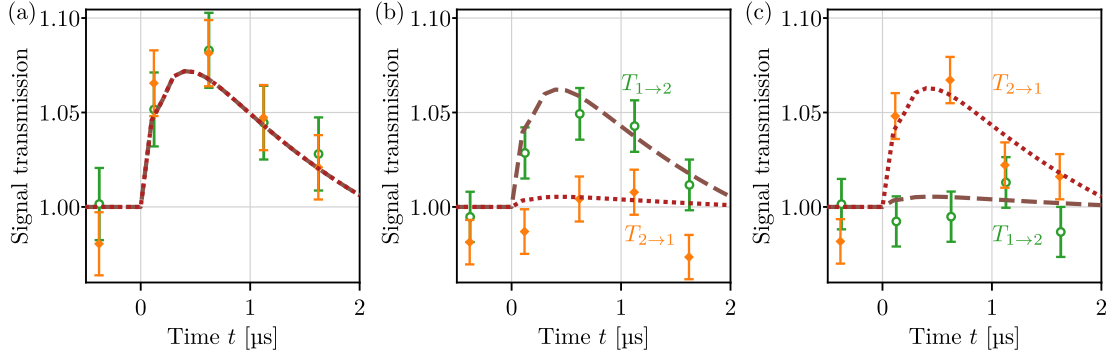


FIGURE 4.7: Evolution of the signal transmission in the magnetic field-free case. (a) We prepare the atoms in a statistical mixture of the states $|F = 4, m_F = +4\rangle$ and $|F = 4, m_F = -4\rangle$. We observe the same signal gain in the $1 \rightarrow 2$ direction (green circles) and in the $2 \rightarrow 1$ direction (orange diamonds). (b) We prepare the atom exclusively in state $|F = 4, m_F = -4\rangle$. Gain occurs only in the $1 \rightarrow 2$ direction. (c) The atoms are prepared only in $|F = 4, m_F = +4\rangle$. Now, we observe signal gain only in the $2 \rightarrow 1$ direction. Within the error bars, all measured signal transmissions agree with the theoretical predictions for the $1 \rightarrow 2$ direction (dashed brown line) as well as in the $2 \rightarrow 1$ direction (dotted red line).

4.2.3 Evolution of the Signal Transmission

In this section, we analyze the evolution of the signal transmission and compare it to theoretical calculations (see Fig. 4.7). For the calculations, we use the same parameters as presented in Tab. 1.1. However, here the ground state decoherence rate, γ_{ba} , is different, and we adapt the number of atoms, N , to the detected values. As for the measurements with an externally applied magnetic field, we chose the employed value of $\gamma_{\text{ba}} = 2\pi \times 1.6 \text{ MHz}$ to be about 40 % lower than the value obtained from the fits of the absorption spectra in Fig. 4.5.

In Fig. 4.7(a), we present the evolution of the signal transmission when the atoms are prepared in a statistical mixture of the states $|6S_{1/2}, F = 4, m_F = +4\rangle$ and $|6S_{1/2}, F = 4, m_F = -4\rangle$. Within the error bars, we see the same signal transmissions in both directions. We compare the signal transmission to theoretical calculations with $N \approx 310$ atoms in each state, as obtained from an independent measurement. In both directions, the signals agree with the theoretical expectations. We, therefore, infer that

the observed reciprocal gain is in agreement with the theory.

We now prepare the atoms in either of the two outermost Zeeman substates. In Fig. 4.7(b), we present a measurement where $N \approx 270$ atoms were prepared in state $|F = 4, m_F = -4\rangle$, and the atoms in state $|F = 4, m_F = +4\rangle$ were removed from the trap. We only observe a signal gain in the $1 \rightarrow 2$ direction in agreement with the theoretical calculations. In the measurement shown in Fig. 4.7(c), $N \approx 270$ atoms were exclusively prepared in $|F = 4, m_F = +4\rangle$. Signal gain occurs only in the $2 \rightarrow 1$ direction. Within the error bars, the experimental data agree with our theoretical calculations. Thus, we conclude that signal gain can be controlled with the atomic spin state, in agreement with the theoretical predictions.

4.3 Outlook

In the last chapters, we demonstrated atomic spin-controlled non-reciprocal amplification of a fiber-guided light field. Our realization was based on Raman gain provided by spin-polarized cesium atoms that are trapped close to an optical nanofiber. We showed that the non-reciprocal response originates from the propagation direction-dependent local polarization of the nanofiber-guided mode in conjunction with a polarization-dependent atom-light coupling. We observed a clear non-reciprocal gain in one direction, in agreement with our theoretical calculations. Moreover, we experimentally demonstrated the reconfiguration of the directional amplifier by modifying the atomic spin state. This non-reciprocity prevails when sending the signal field simultaneously in both directions. We investigated key amplifier properties such as e.g., the bandwidth and the noise characteristics, where the latter are mainly given by the spontaneous scattering background of the pump field. As discussed, our scheme remains non-reciprocal even without an offset magnetic field. We conclude that we successfully developed a non-reciprocal amplifier that is controlled by the atomic spin state.

Our scheme can be implemented using other quantum emitters with a suitable level scheme coupled to nanophotonic waveguides [54]. In that way, it could enable applications in various domains of the electromagnetic spectrum. For example, suited emitters could allow realizations in the microwave domain where non-reciprocal magnetic field-free amplification is a highly sought capability [188, 189]. Also at telecom wavelengths the construction of a similar system would be possible by using rubidium atoms. They feature a transition at a wavelength of 1529 nm, and trapping next to a nanofiber was experimentally demonstrated in two-color dipole

traps similar to the present system [76, 78]. Specifically, one could implement our scheme with two pump fields at the wavelengths of 795 nm and 1476 nm that drive the two-photon $|5S_{1/2}, F = 3, m_F = 3\rangle \rightarrow |4D_{3/2}, F = 3, m_F = 3\rangle$ transition of ^{85}Rb , and a signal field at a wavelength of 1529 nm that drives the $|5P_{3/2}, F = 2, m_F = 2\rangle \rightarrow |4D_{3/2}, F = 3, m_F = 3\rangle$ transition.

Our results may simplify the construction of complex optical networks [100, 101]. Moreover, the high level of control in our platform enables the study of quantum thermodynamics in the presence of non-reciprocal interactions [194, 195]. We demonstrated pulsed operation, but we might implement a suitable repumping scheme to study continuous-wave operation. This could allow the study of lasing with cold atoms [184, 196] with spin-controlled directionality, possibly requiring the use of a ring resonator. In future works, we might study various unidirectional lasing mechanisms. Currently, our system would require a cavity, but a higher β factor could also enable random lasing [197, 198]. Another potential future topic is the investigation of coherent Raman manipulation [129, 130] of quantum emitters unidirectionally coupled to a waveguide.

Chapter 5

Antisymmetric Non-Reciprocal Phase Shifts based on Chiral Light-Matter Coupling

5.1 Introduction and Motivation

In an optical non-reciprocal phase shifter, the phase shift depends on the propagation direction of light through the device. This effect is frequently used to design other, more advanced non-reciprocal devices, for example, isolators and circulators [95]. Nowadays, most optical isolators are based on non-reciprocal phase shifts in magneto-optical materials [199, 200]. However, such Faraday isolators are typically bulky, costly, and are hard to integrate [201, 202].

In circularly polarized light fields, the direction of the electric field rotates in a plane perpendicular to the propagation direction of the wave. In materials, a rotating electric field causes a force on charged particles. The resulting movement of the particles creates a magnetic field. If we apply a magnetic field along the propagation direction of the light, the effective magnetic field in the material depends on the direction of rotation of the electric field. As a result, the dynamics of the interaction of the fields with the material changes. This effect, known as the longitudinal Faraday effect [93], is used in Faraday rotators where left and right circularly polarized waves propagate at different speeds. This circular birefringence leads to a phase difference that depends on the propagation direction of the light through the Faraday rotator. The sign of the relative phase shift between the circular eigenmodes is reversed when the propagation direction is reversed, leading to an antisymmetric phase shift. In particular, if the input light

field is linearly polarized, the Faraday effect causes a polarization rotation proportional to the projection of the magnetic field along the direction of the light propagation. The output light field is, then, also linearly polarized but its plane of polarization is rotated. Here, we report on a new method for generating an antisymmetric phase shift based on a substantially different origin. In contrast to the longitudinal Faraday effect, it uses linear instead of circular birefringence. Here, the phase velocity of light of two orthogonal linear polarizations of the same propagation direction is different. If one component is unchanged and one is delayed by a phase ϕ , we can describe the system by the Jones matrix [94]

$$\mathbf{T} = \begin{pmatrix} 1 & 0 \\ 0 & e^{-i\phi} \end{pmatrix}. \quad (5.1)$$

Such a system is known as a waveplate or wave retarder. Two common types of waveplates are the half-wave plate ($\phi = \pi$) and the quarter-wave plate ($\phi = \pi/2$). However, waveplates are reciprocal devices, whereas our system is non-reciprocal because, as we will see, the sign of the phase shift flips with the propagation direction of the light field through the device.

Our scheme is based on emitters that are chirally coupled to spin-momentum locked nanophotonic modes [25, 54]. Specifically, we utilize spin-polarized cesium atoms that are trapped close to the surface of an optical nanofiber. The tight confinement of the guided light in the nanofiber leads to a propagation direction-dependent polarization of the light at the location of the atoms [115]. The resulting σ^- and σ^+ polarizations selectively couple to two different cesium transitions, generating a V-type level scheme. Recently, V-type atoms trapped close to an optical nanofiber were experimentally investigated [203]. Moreover, V-type atoms coupled to a spin-momentum locked waveguide were theoretically studied [204]. When suitably preparing the atomic spin state, the transition strength of the two transitions is equal, and thus, the phase shift is the same for the two propagation directions. However, when we induce a Zeeman shift to the excited levels, the transition frequencies shift with a different sign, and the phase shift gets, in general, non-reciprocal. Notably, for a laser with a frequency that is tuned right between the two transitions frequencies, the phase shift is antisymmetric, i.e., it has the same magnitude but opposite sign for the two propagation directions. In this chapter, we detect this phase shift and demonstrate that it scales linearly with the number of trapped atoms.

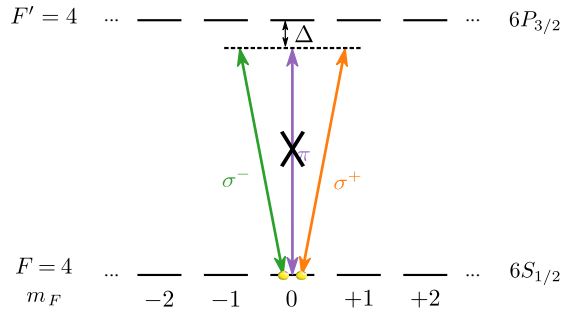


FIGURE 5.1: Relevant cesium energy levels. We prepare the atoms in state $|6S_{1/2}, F = 4, m_F = 0\rangle$. The σ^\pm -polarized probe fields couple to the $|6S_{1/2}, F = 4, m_F = 0\rangle \rightarrow |6P_{3/2}, F' = 4, m_{F'} = \pm 1\rangle$ transitions. The probe laser is detuned by Δ from the dipole-forbidden $|F = 4, m_F = 0\rangle \rightarrow |F' = 4, m_{F'} = 0\rangle$ transition.

5.2 Experimental Setup and Method

With cold atoms in a nanofiber-based optical dipole trap, the phase shift and polarization rotation induced on the guided light was measured [75, 205] and studied theoretically [206]. Here, we extend the experimental setup and the employed methods. First, we present the relevant cesium level scheme and discuss the phase shift around an atomic resonance. Then, we describe the setup of the probe laser and how we detect the probe phase shift. Finally, we present the experimental sequence.

5.2.1 Atomic Structure

In Fig. 5.1, we present the relevant cesium level scheme. We prepare the atoms in the initial state $|6S_{1/2}, F = 4, m_F = 0\rangle$. The probe laser has a detuning of Δ from the dipole-forbidden $|6S_{1/2}, F = 4, m_F = 0\rangle \rightarrow |6P_{3/2}, F' = 4, m_{F'} = 0\rangle$ transition. Between this initial state and the states of the $|6P_{3/2}, F' = 4\rangle$ manifold, a light field can couple to two dipole-allowed transitions. If the field is σ^- polarized, it couples to the $|m_F = 0\rangle \rightarrow |m_{F'} = -1\rangle$ transition; if it is σ^+ polarized, it couples to the $|m_F = 0\rangle \rightarrow |m_{F'} = +1\rangle$ transition. The dipole matrix elements of these transitions have the same absolute value, i.e., both transitions feature the same transition strength [154].

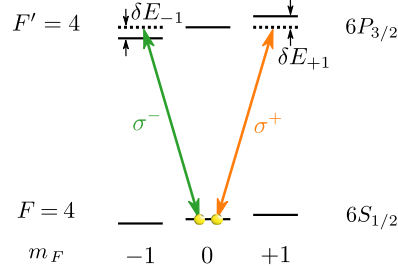


FIGURE 5.2: Illustration of the Zeeman energy shifts. We use Zeeman shifts to modify the transition frequencies in the V-type level scheme. Two different resonances emerge at $\Delta = \delta E_{\pm 1}$. At $\Delta = 0$, we expect an antisymmetric non-reciprocal phase shift for a quasilinearly polarized fiber-guided light field.

In order to modify the transition frequencies, we induce energy shifts to the Zeeman substates by applying a magnetic field (see Fig. 5.2). This also stabilizes the m_F state against depopulation and dephasing due to stray magnetic fields and spin-motion coupling [80]. We can calculate the Zeeman shifts using [207]

$$\delta E_{m_F} = \mu_B g_F m_F B_z, \quad (5.2)$$

where μ_B is the Bohr magneton, B_z is the magnitude of the offset magnetic field along the quantization axis $+z$, and g_F is the Landé g -factor. Specifically, for the $|6P_{3/2}, F' = 4\rangle$ manifold, $g_{F'}$ is 4/15 corresponding to a Zeeman splitting between adjacent magnetic sublevels of 0.37 MHz/G [154]. From Eq. 5.2 follows that the initial state $|6S_{1/2}, F = 4, m_F = 0\rangle$ does not shift with the magnetic field and that the shift of the $|m_F = 0\rangle \rightarrow |m_{F'} = -1\rangle$ transition frequency is proportional to $-B_z$. The shift of the $|m_F = 0\rangle \rightarrow |m_{F'} = +1\rangle$ transition frequency has the same magnitude but the opposite sign, i.e., it is proportional to $+B_z$.

Thus, for a finite magnetic field, two resonances emerge at $\Delta = \pm B_z \cdot 0.37$ MHz/G. Spin-momentum locking in our system leads to a probe field that is either σ^+ or σ^- polarized at the location of the atoms [25, 37, 79] (see also Sec. 2.3). Depending on the propagation direction of the probe field in the nanofiber, this allows us to observe one of the resonances when probing in one direction and the other resonance when probing in the other direction. Interestingly, the phase shift around the resonances is non-reciprocal. Specifically, at $\Delta = 0$, we expect an antisymmetric phase shift, i.e., a phase

5.2. Experimental Setup and Method

shift with the same absolute value but with a different sign. The maximal phase shifts of the probe field occur at a detuning of $\Delta = \pm\gamma/2$ [205], where $\gamma \approx 2\pi \times 5.2$ MHz [136] is the excited state decay rate. Thus, we expect the maximal relative phase shift between the σ^+ -polarized field and the σ^- -polarized field at a magnetic field of

$$B_z = \pm \frac{\gamma/2}{0.37 \text{ MHz/G}} \approx \pm 7 \text{ G} . \quad (5.3)$$

5.2.2 Phase Shift around an Atomic Resonance

When the probe light passes the atomic ensemble, the acquired phase shift is detuning-dependent. As we show in Appendix Sec. A, around an atomic resonance, the detuning dependence of the phase shift is given by [75, 205]

$$\phi(\tilde{\Delta}) = -2\phi_{\max} \frac{\tilde{\Delta}}{1 + \tilde{\Delta}^2} , \quad (5.4)$$

where $\tilde{\Delta} = 2(\omega_1 - \omega_a)/\gamma$ is the detuning of the probe laser with frequency ω_1 from the atomic resonance at a frequency of ω_a , normalized to half the natural linewidth of the atomic transition, $\gamma/2$. The maximal absolute phase shift ϕ_{\max} occurs at a detuning $\tilde{\Delta} = \pm 1$ which corresponds to $\omega_1 - \omega_a = \pm\gamma/2$. We use $\phi_{\max} = \text{OD}/4$ [208] to rewrite Eq. 5.4 as

$$\phi(\tilde{\Delta}) = -\frac{\text{OD}}{2} \frac{\tilde{\Delta}}{1 + \tilde{\Delta}^2} , \quad (5.5)$$

where OD is the optical depth of the atomic ensemble at $\tilde{\Delta} = 0$. In our relevant level scheme, we have two transitions. Thus, the total phase shift is

$$\begin{aligned} \phi(\Delta) &= -\text{OD}_{-1} \frac{\gamma(\Delta - \delta E_{-1})}{\gamma^2 + 4(\Delta - \delta E_{-1})^2} - \text{OD}_{+1} \frac{\gamma(\Delta - \delta E_{+1})}{\gamma^2 + 4(\Delta - \delta E_{+1})^2} , \\ &= -\text{OD}_{-1} \frac{\gamma(\Delta + B_z \cdot 0.37 \text{ MHz/G})}{\gamma^2 + 4(\Delta + B_z \cdot 0.37 \text{ MHz/G})^2} - \text{OD}_{+1} \frac{\gamma(\Delta - B_z \cdot 0.37 \text{ MHz/G})}{\gamma^2 + 4(\Delta - B_z \cdot 0.37 \text{ MHz/G})^2} , \end{aligned} \quad (5.6)$$

where $\text{OD}_{\pm 1}$ is the maximal optical depth of the ensemble for a σ^{\pm} polarized light field.

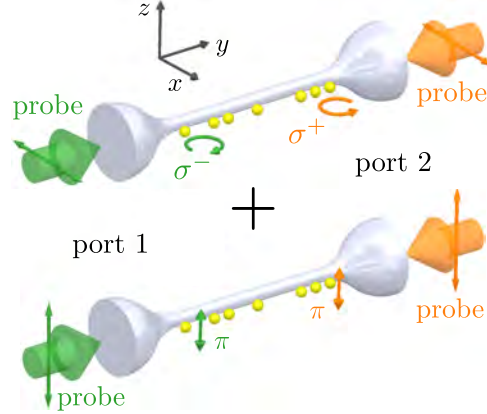


FIGURE 5.3: Schematic of the experimental setup. We trap atoms in a two-color dipole trap on one side of an optical nanofiber. We couple a probe beam into one of the two ports of the fiber. The field is linearly polarized, with the polarization axis adjusted to 45° with respect to the x - y plane that contains the atoms. We describe the polarization of the fiber-guided light field as a superposition of two linearly polarized modes: Upper panel, at the location of the atoms, the \mathbf{e}_{\parallel} eigenmode is σ^- (σ^+) polarized when the light propagates from port 1 to port 2 (port 2 to port 1). Lower panel, the \mathbf{e}_{\perp} eigenmode is for both propagation directions π polarized at the location of the atoms.

5.2.3 Experimental Setup

Here, we discuss the experimental setup for the measurements of the non-reciprocal phase shift. Figure 5.3 shows an illustration of the relevant probe polarizations. The atoms are trapped in an array on one side of the nanofiber. We couple a probe beam into the tapered optical fiber with the linear polarization axis adjusted to 45° with respect to the plane containing the atoms (x - y plane in Fig. 5.3). We describe the polarization as an equal superposition of the two eigenmodes \mathbf{e}_{\parallel} and \mathbf{e}_{\perp} , where \mathbf{e}_{\parallel} is the normalized fundamental HE_{11} mode, quasilinearly polarized in the plane of the atoms [115], and \mathbf{e}_{\perp} is orthogonal to that. The input field is thus

$$\mathbf{E}_{\text{in}} = \frac{E_0}{\sqrt{2}}(\mathbf{e}_{\parallel} + \mathbf{e}_{\perp}), \quad (5.7)$$

5.2. Experimental Setup and Method

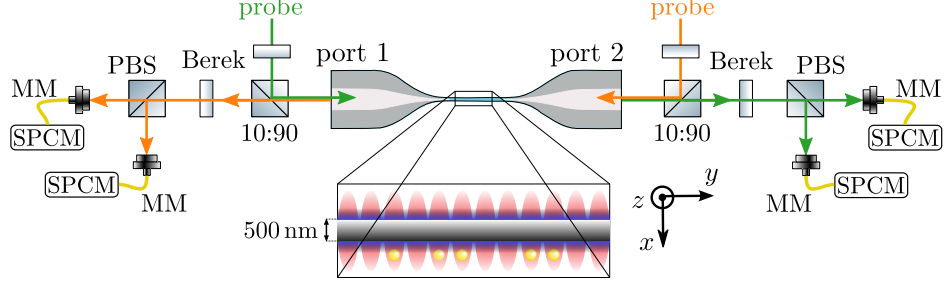


FIGURE 5.4: Schematic of the probe beam path. We launch the probe field into both ports of the nanofiber. We use Berek compensators to control the polarization of the probe field in the nanofiber. The probe light transmitted through the atomic ensemble is analyzed using a polarization-sensitive detection setup based on polarizing beamsplitters (PBS) and single-photon counting modules (SPCM), see main text. (MM, multi-mode fiber)

where E_0 is the field amplitude.

Our quantization axis is $+z$. The local polarization of the \mathbf{e}_{\parallel} eigenmode depends on the propagation direction (see upper panel of Fig. 5.3). If the probe field propagates from port 1 to port 2, it is predominantly σ^- polarized at the location of the atoms [79]. If it propagates in the $2 \rightarrow 1$ direction, it is σ^+ polarized at the location of the atoms. Specifically, the overlap of the probe field at the position of the atoms with σ^- (σ^+) polarization is 92% (8%) when propagating in the $1 \rightarrow 2$ direction. The polarization overlaps interchange when the probe field propagates in the $2 \rightarrow 1$ direction. In contrast, the polarization of the \mathbf{e}_{\perp} eigenmode does not depend on the propagation direction (see lower panel of Fig. 5.3). The probe field with this polarization is always π polarized at the location of the atoms and does not couple to the atoms because the $|6S_{1/2}, F=4, m_F=0\rangle \rightarrow |6P_{3/2}, F'=4, m_{F'}=0\rangle$ transition is dipole-forbidden. Thus, the resulting light field amplitude after interaction with the atoms is given by

$$\mathbf{E}_{\text{out}} = \frac{E_0}{\sqrt{2}}(t_{\parallel}e^{i\phi_{\parallel}}\mathbf{e}_{\parallel} + \mathbf{e}_{\perp}), \quad (5.8)$$

where ϕ_{\parallel} is the phase and t_{\parallel} is the modulus of the amplitude transmission coefficient for the \mathbf{e}_{\parallel} eigenmode.

Now, we discuss the optical setup of the probe laser field (see Fig. 5.4). Apart from

the detection setup, it is similar to the beam path of the signal laser field presented in Fig. 2.6. We control the probe polarization in the nanofiber with Berek compensators¹. We use beamsplitters² to combine and separate the incoming and the transmitted beams. Then, the probe light propagates through the nanofiber, interacts with the atomic ensemble, and exits the other end of the fiber in an altered polarization state.

Using polarization optics, we detect this polarization change by measuring the S_3 component of the Stokes vector [137, 205, 209]. From S_3 , we can infer the relative phase shift of the \mathbf{e}_{\parallel} eigenmode with respect to the unshifted \mathbf{e}_{\perp} eigenmode. Specifically, we use Berek compensators³ in both detection setups, which act as a quarter-wave plate and, moreover, compensate any parasitic birefringence along the optical path. Thus, without atoms, the light field after the Berek compensators is circularly polarized. Then, we split it with polarizing beamsplitters⁴ (PBS). By sending the light fields via multi-mode fibers⁵ onto SPCMs⁶, we detect the power at the output ports of each PBS, given by [205]

$$P_+ = \left| \frac{1}{\sqrt{2}} (\mathbf{e}_{\parallel}^* + i\mathbf{e}_{\perp}^*) \cdot \mathbf{E}_{\text{out}} \right|^2, \quad (5.9)$$

$$P_- = \left| \frac{1}{\sqrt{2}} (\mathbf{e}_{\parallel}^* - i\mathbf{e}_{\perp}^*) \cdot \mathbf{E}_{\text{out}} \right|^2. \quad (5.10)$$

We calculate the S_3 component of the Stokes vector according to [63, 205]

$$\frac{S_3}{S_0} = \frac{P_+ - P_-}{P_+ + P_-} = \frac{2t_{\parallel}}{1 + t_{\parallel}^2} \sin(\phi_{\parallel}). \quad (5.11)$$

For large transmission with $t_{\parallel}^2 \geq 0.75$, this quantity is well approximated by [205]

$$\frac{S_3}{S_0} \approx \sin(\phi_{\parallel}). \quad (5.12)$$

¹FOCtek, YVO4 crystal

²Thorlabs, BS041

³FOCtek, YVO4 crystal

⁴Thorlabs, PBS122

⁵Thorlabs, M69L02

⁶Excelitas Technologies, SPCM-AQRH-14-FC

5.2. Experimental Setup and Method

Therefore, the absolute phase shift of the \mathbf{e}_{\parallel} mode can be estimated by

$$\phi_{\parallel} = \arcsin\left(\frac{S_3}{S_0}\right) = \arcsin\left(\frac{P_+ - P_-}{P_+ + P_-}\right). \quad (5.13)$$

In the following, we measure P_+ and P_- . Then, we use Eq. 5.13 to calculate the phase shift ϕ_{\parallel} of the \mathbf{e}_{\parallel} eigenmode.

5.2.4 Experimental Sequence

In this section, we present our sequence to detect the phase shift of the probe light. First, we discuss the preparation of the atoms in the initial state. We use a molasses stage to load atoms from a MOT into the two-color optical dipole trap [15]. Here, the blue-detuned running wave has a free-space wavelength of $\lambda = 785$ nm and a fiber-guided power of ~ 17.8 mW. The red standing wave at $\lambda = 1064$ nm has a total power of ~ 2.9 mW. According to a calculation of the optical potentials, the atoms are then trapped ~ 270 nm away from the surface of the nanofiber.

After loading the atoms into the dipole trap, we remove the atoms trapped on one side of the nanofiber using side-selective degenerate Raman heating [155]. Simultaneously, the atoms in the remaining array are pumped to state $|6S_{1/2}, F = 4, m_F = -4\rangle$ and cooled close to their motional ground state. This step is performed at an offset magnetic field of $B_z \approx 0.5$ G. Then, we measure the OD of the atomic ensemble by recording the transmission of a fiber-guided laser field while scanning its frequency across the resonance of the $|6S_{1/2}, F = 4\rangle \rightarrow |6P_{3/2}, F' = 5\rangle$ cycling transition of the D_2 line. Then, we use the tabulated ratios of the transition strengths [154] to estimate the OD on the probe transitions $|F = 4, m_F = 0\rangle \rightarrow |F' = 4, m_{F'} = \pm 1\rangle$.

Next, we ramp the magnetic field up to $B_z \approx 9$ G. This is slightly higher than 7 G, which follows from Eq. 5.3 because we expect the linewidth of the transition to be slightly broader than the textbook value $\gamma = 5.225$ MHz [38, 81]. We switch on a free-space laser field that propagates in the $+x$ direction and is π polarized. This laser is tuned close to the resonance of the $|6S_{1/2}, F = 4\rangle \rightarrow |6P_{1/2}, F'' = 4\rangle$ transition of the D_1 line. We apply optical pumping with this field for 0.7 ms, which ideally pumps all atoms to the dark state $|6S_{1/2}, F = 4, m_F = 0\rangle$. We turn off the optical pumping and record the background for 0.2 ms. This background arises due to, e.g., insufficient suppression of the trapping light fields and detector dark counts. Then, we switch on the probe

laser within tens of nanoseconds with an AOM⁷. We alternate the propagation direction of the probe field between every run. We measure the transmitted probe powers P_- and P_+ for 10 μs with the SPCMs. In this time interval, the optical pumping out of the V-level scheme is negligible. Then, we remove the atoms from the trap, take a reference measurement to normalize the powers P_- and P_+ , and calculate the phase shift using Eq. 5.13. In total, the experimental cycle lasts for ~ 3 s. We repeat the experiment until the counting statistic is sufficiently good, which typically is the case after ~ 1000 cycles.

5.3 Experimental Demonstration of Non-Reciprocal Phase Shifts

Here, we present our experimental results. We start by discussing the frequency dependence of the relative probe phase shift of the \mathbf{e}_{\parallel} eigenmode with respect to the \mathbf{e}_{\perp} eigenmode. For this, we scan Δ around the resonances and measure the phase shift ϕ_{\parallel} in the $1 \rightarrow 2$ and the $2 \rightarrow 1$ directions (see Fig. 5.5). In both directions, we find a phase shift that has the expected frequency dependence, given by Eq. 5.4.

We fit the phase shifts with Eq. 5.6, using γ , B_z , and a global optical depth OD as our free fit parameters. For the measurement in the $1 \rightarrow 2$ ($2 \rightarrow 1$) direction, we assume $\text{OD}_{-1(+1)} = 0.92 \cdot \text{OD}$ and $\text{OD}_{+1(-1)} = 0.08 \cdot \text{OD}$ to account for the imperfect circular probe polarization [79]. Within the error bars, the fits agree mostly with the experimental data. From the fit, we obtain in the $1 \rightarrow 2$ direction $\text{OD}_{1 \rightarrow 2} = 0.93(6)$ and in the $2 \rightarrow 1$ direction $\text{OD}_{2 \rightarrow 1} = 0.98(7)$, i.e., within the error bars, the ODs agree with each other. In particular, this implies that the polarization plane of the probe field is the same in both directions. The fitted decay rates $\gamma_{1 \rightarrow 2} = 2\pi \times 5.9(6)$ MHz and $\gamma_{2 \rightarrow 1} = 2\pi \times 6.2(7)$ MHz also agree within the error bars. As previously reported by C. Sayrin *et al.* [81] and R. Mitsch *et al.* [38], the decay rate is higher than the natural decay rate of $\gamma = 2\pi \times 5.225(8)$ MHz [136], probably due to inhomogeneous broadening effects resulting, e.g., from inhomogeneous light shifts induced by the trapping lasers. In both directions, the fitting result for the magnetic field is $B_z \approx 11$ G, which is in reasonable agreement with the set value of 9 G (see Sec. 6.2.5).

The zero-crossing of the phase shift in the $1 \rightarrow 2$ direction, $\phi_{\parallel}^{1 \rightarrow 2}$, occurs at a different detuning Δ than the zero-crossing of the phase shift in the $2 \rightarrow 1$ direction, $\phi_{\parallel}^{2 \rightarrow 1}$. As desired, at the probe detuning where $\phi_{\parallel}^{1 \rightarrow 2}$ has a minimum, $\phi_{\parallel}^{2 \rightarrow 1}$ has a

⁷AA Opto Electronic, MT110-B50A1-VIS

5.3. Experimental Demonstration of Non-Reciprocal Phase Shifts

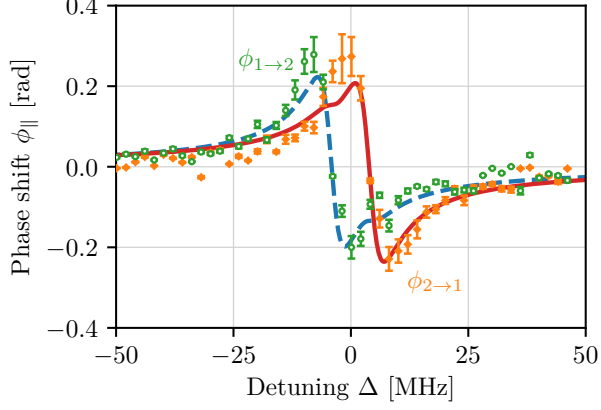


FIGURE 5.5: Phase shift $\phi_{||}$ as a function of the probe laser detuning Δ . The resonance in the $1 \rightarrow 2$ direction (green circles) occurs at a different detuning Δ than in the $2 \rightarrow 1$ direction (orange diamonds). This is confirmed by fits that agree well with the experimental data (lines). As expected, at $\Delta \approx 0$ MHz, we observe $\phi_{||}^{2 \rightarrow 1} \approx -\phi_{||}^{1 \rightarrow 2}$, i.e., here, the phase shift is antisymmetric.

maximum. Moreover, the absolute shift is similar, i.e., $\phi_{||}^{1 \rightarrow 2} \approx -\phi_{||}^{2 \rightarrow 1}$. We infer that the phase shift is non-reciprocal and antisymmetric around $\Delta = 0$ MHz.

Next, we study the antisymmetric phase shift as a function of OD. We vary the OD by loading a different number of atoms in the nanofiber-based dipole trap. We tune the probe laser in resonance with the dipole forbidden $|F = 4, m_F = 0\rangle \rightarrow |F' = 4, m_{F'} = 0\rangle$ transition, i.e., $\Delta = 0$ MHz. In Fig. 5.6, we present measurements of $\phi_{||}^{1 \rightarrow 2}$ and $\phi_{||}^{2 \rightarrow 1}$ for various ODs. We observe a linear dependence of the phase shift on the OD in both directions. The antisymmetric behavior of the phase shifts, $\phi_{||}^{2 \rightarrow 1} \approx -\phi_{||}^{1 \rightarrow 2}$, is maintained over the whole range. We fit the measurements with the linear function $\phi_{||} = k \cdot \text{OD}$. In the $1 \rightarrow 2$ direction, we find a slope of $k = -0.17(1)$ rad/OD. In the $2 \rightarrow 1$ direction, the slope is $k = 0.19(1)$ rad/OD. The absolute values of the slopes agree with each other within the error bars confirming the antisymmetric proportionality of the phase shift $\phi_{||}$ with the OD.

We compare the measurements with our model (see Eq. 5.6). We find a theoretically expected slope of $k \approx \pm 0.20$ rad/OD, where we assumed $\Delta = 0$ MHz, $\gamma = 2\pi \times 5.9$ MHz, $B_z = 10$ G, $\text{OD}_{-(+)} = 0.92 \cdot \text{OD}$, and $\text{OD}_{+(-)} = 0.08 \cdot \text{OD}$. We attribute the deviation

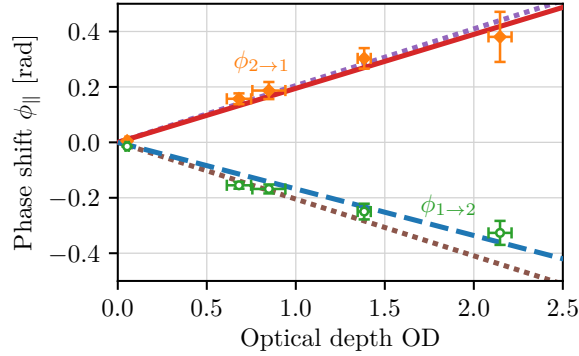


FIGURE 5.6: OD dependence of the phase shift. We tune the probe laser to $\Delta = 0$ MHz and measure the phase shifts $\phi_{\parallel}^{1 \rightarrow 2}$ (green circles) and $\phi_{\parallel}^{2 \rightarrow 1}$ (orange diamonds). With linear fits, we find a slope of $k = -0.17(1)$ rad in the $1 \rightarrow 2$ direction (dashed blue line) and a slope of $k = 0.19(1)$ rad in the $2 \rightarrow 1$ direction (solid red line). This agrees well with the theoretical expectation (dotted lines).

between the measurement and theoretical expectation to insufficient OD and magnetic field calibrations. If we take the errors of our OD and magnetic field calibration into account, the experimental results and the theory agree within the error bars.

5.4 Summary and Outlook

In this chapter, we proposed and experimentally demonstrated an antisymmetric non-reciprocal phase shift based on chiral light-matter coupling. The propagation direction-dependent coupling originates from the local polarization of the nanofiber-guided probe field in conjunction with polarization-dependent atom-light coupling. We spin-polarized the atoms such that the light field couples to different transitions with the same transition strength, depending on its propagation direction. We used Zeeman energy shifts to modify the transition frequencies in this effective V-type level scheme. This way, the resonance frequencies are met at different probe laser frequencies. We showed that this leads to a non-reciprocal phase shift. Specifically, at one detuning, this non-reciprocal phase shift is antisymmetric. We have demonstrated that the phase shift scales linearly with the optical depth and that the antisymmetric behavior is maintained for all optical

5.4. Summary and Outlook

depths. Such an antisymmetric phase shift might be interpreted as an effective gauge potential for photons or the photonic Aharonov–Bohm effect [210–215].

Our implementation used magnetic fields to shift the Zeeman substates. However, our scheme can readily be realized without magnetic fields using vector light shifts. In future projects, we might also investigate atomic spin-controlled non-reciprocal phase shifts. Here, tensor light shifts could be used for the spin polarization of the atoms [83].

Our demonstrated non-reciprocal phase shifter enables the development of novel photonic devices. For example, optical isolators and circulators can be realized by embedding such phase shifters in a Mach–Zehnder interferometer [42, 95, 199, 216–218]. Using light shifts instead of magnetic fields, our scheme could be implemented on-chip where non-reciprocity is a highly desired tool [219]. Eventually, this might lead to a scalable architecture for a quantum network [220]. Moreover, our scheme can be realized with defect centers in diamonds coupled to a spin-momentum locked waveguide. For example, nitrogen-vacancy centers would feature a suitable ground state level scheme, and the sensitivity to circular microwaves was recently investigated [221]. This could enable applications also in the microwave domain. Finally, we might go to higher optical depths and realize π phase shifts. This would also allow us to construct a gyrator [222] which is a fundamental non-reciprocal element that introduces asymmetric phase shifts in the transmission that differ by π [59].

Chapter 6

Lifetime Measurement of the Cesium $5D_{5/2}$ State

In the last chapters, we performed experiments with laser-cooled cesium atoms trapped in two-color dipole traps in the vicinity of an optical nanofiber. We used blue-detuned trapping light fields at free-space wavelengths of $\lambda = 760$ nm and $\lambda = 785$ nm. An attractive alternative blue-detuned wavelength for trapping is around $\lambda = 687$ nm because at this so-called magic wavelength, the differential AC Stark shifts for the $6S_{1/2}$ and $6P_{3/2}$ states cancel [223]. However, the $6S_{1/2} \rightarrow 5D_{5/2}$ electric quadrupole transition has a wavelength of $\lambda = 685$ nm, which is close to this magic wavelength at $\lambda = 687$ nm. This triggered our following investigation of the $6S_{1/2} \rightarrow 5D_{5/2}$ transition and the $5D_{5/2}$ state [224].

In this chapter, we measure the lifetime of the cesium $5D_{5/2}$ state. We excite atoms that reside initially in the electronic ground state, $6S_{1/2}$, in a hot vapor cell via the electric quadrupole transition at a wavelength of 685 nm. We record the subsequently emitted fluorescence at a wavelength of 852 nm. We find a lifetime of 1353(5) ns for the $5D_{5/2}$ state. This value is in agreement with a recent theoretical prediction and contributes to resolving a long-standing disagreement between a number of experimental and theoretical results. The discussion in this chapter closely follows the published manuscript [225].

6.1 Introduction and Motivation

Alkali-metal atoms feature a simple electronic level structure. This makes them a popular test bench for atomic structure theories. Precision measurements of alkali-metal atomic properties are thus crucial for our theoretical understanding of nature. Standard experimental methods are lifetime studies of excited atomic states. This way, we can obtain information about the atomic structure and the interaction of an atom with an electromagnetic field.

In this chapter, we experimentally study the alkali-metal cesium (Cs). We only discuss the stable isotope ^{133}Cs , which is an established species to test the foundations of physics. For instance, one of the most precise detections of parity non-conservation (PNC) in the electroweak interaction was performed with cesium atoms [226, 227]. These experiments are based on S - S transitions, but it has been proposed that S - D transitions are promising candidates to improve the precision of the measurements [228]. In order to compare the results of such experiments with theoretical predictions, precise measurements of cesium atomic properties are required. This can be achieved by precisely measuring the lifetimes of the cesium D states.

Recent experimental measurements of cesium lifetimes include the states $6P_{3/2}$ [136, 229], $7S_{1/2}$ [230], $7P_{3/2}$, and $7P_{1/2}$ [231]. The lifetimes of low-lying D -states were measured with high precision in the alkali-metal atoms rubidium [8] and francium [232]. For cesium, the lifetime of the $5D_{5/2}$ state has been measured with an increasing precision [233–237]. Furthermore, several theoretical predictions were developed [238–245]. In Tab. 6.1, we summarize these measurements and calculations. In section 6.5, we also present a figure of this summary.

The two most recent measurements of the $5D_{5/2}$ -lifetime were performed in the 1990s. At that time, Hoeling *et al.* [236] and DiBerardino *et al.* [237] published values of 1226(12) ns and 1281(9) ns, respectively. Both measurements state a high precision and a small error bar. However, these reported values disagree clearly beyond their stated error bars. As a result, a theoretical discussion about this lifetime arose. Safronova and Clark [243] showed that there are inconsistencies between the measurements of the $5D_{5/2}$ -lifetime and independently measured polarizabilities of the $6P$ states of cesium. From the measurements of the $6P_{3/2}$ state polarizability performed by Tanner and Wieman [246], they derived a $5D_{5/2}$ -lifetime of 1359(18) ns [243]. Later, this value was refined to 1351(52) ns [245]. Recently, independent theoretical calculations by Sahoo [244] predicted a lifetime of 1270(28) ns. This is in agreement with the

6.2. Experimental Method and Setup

TABLE 6.1: Review of calculations (calc.) and experimental results (exp.) of the lifetime τ_D of the cesium $5D_{5/2}$ state (see also Fig. 6.11).

Year	Ref.	Author(s)	τ_D (ns)	type
1961	[238]	Heavens	1370	calc.
1962	[239]	Stone	1342	calc.
1968	[240]	Warner	1190	calc.
1976	[241]	Fabry	1434	calc.
1984	[242]	Theodosiou	1283	calc.
2004	[243]	Safronova <i>et al.</i>	1359(18)	calc.
2016	[244]	Sahoo	1270(28)	calc.
2016	[245]	Safronova <i>et al.</i>	1351(52)	calc.
1977	[233]	Marek <i>et al.</i>	890(90)	exp.
1992	[234]	Bouchiat <i>et al.</i>	1260(80)	exp.
1992	[235]	Sasso <i>et al.</i>	1250(115)	exp.
1996	[236]	Hoeling <i>et al.</i>	1226(12)	exp.
1998	[237]	DiBerardino <i>et al.</i>	1281(9)	exp.
2020	[225]	this work	1353(5) ns	exp.

measurement by DiBerardino *et al.* but in contradiction with the works of Safronova *et al.*

In this chapter, we discuss our precision measurement of the lifetime, τ_D , of the $5D_{5/2}$ state of cesium. We performed these experiments with a standard technique known as time-resolved single-photon counting. From our measurements, we obtain a lifetime value of 1353(5) ns in agreement with the predictions by Safronova *et al.* [243, 245].

6.2 Experimental Method and Setup

In the present work, we want to detect the lifetime of the cesium $5D_{5/2}$ state experimentally. We perform time-resolved measurements of the atomic fluorescence, which is a common method in the field of atomic lifetime studies [236, 247]. We present an illustration of our experimental method in Fig. 6.1. An excitation laser beam excites atoms

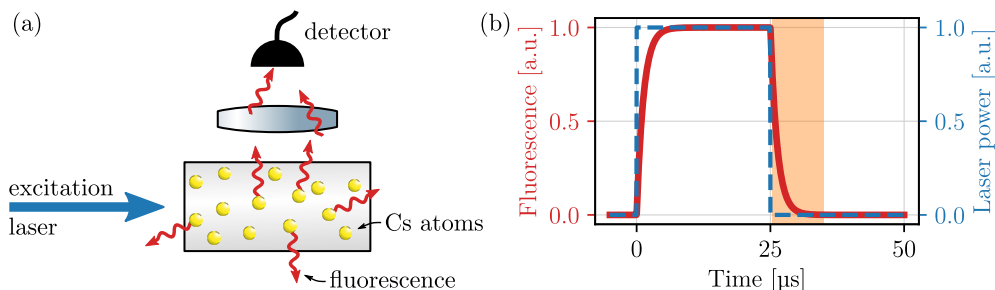


FIGURE 6.1: Illustration of our experimental method. (a) An excitation laser beam excites Cs atoms in a vapor cell which then emit fluorescence in all directions. We collect the fluorescence with a lens from the side and send it to a detector. (b) A simplified illustration of our sequence. At the beginning, we turn the excitation laser beam on (dashed blue line). The atoms get excited and subsequently emit fluorescence (solid red line). After the fluorescence signal reached a steady state, we turn the laser beam off. From a fit of the decaying fluorescence signal (orange area), we get the lifetime of the state.

in a vapor cell which subsequently emit fluorescence in all directions. We detect the fluorescence light emitted by the atoms in a direction perpendicular to the excitation laser beam path (see Fig. 6.1(a)). Under continuous excitation, the fluorescence will reach a steady state (see Fig. 6.1(b)). Then an AOM turns off the excitation beam fast compared to the expected lifetime of the excited state. For a system of independent two-level atoms, the excited atoms will exponentially decay from the upper state to the ground state. We can determine the lifetime of the excited state by fitting the exponential decay of the fluorescence signal. The lifetime is the duration after which $1/e$ of the initially excited atoms are still excited.

In the following, we will discuss the relevant atomic structure and the dynamics of the fluorescence decay in more detail. Then, we present our setup, a few test measurements, and our experimental sequence.

6.2.1 Atomic Level Structure

Cesium has 55 electrons, but because it is an alkali metal, we can readily describe its properties by studying only the outermost electron. In the ground state, this electron

6.2. Experimental Method and Setup

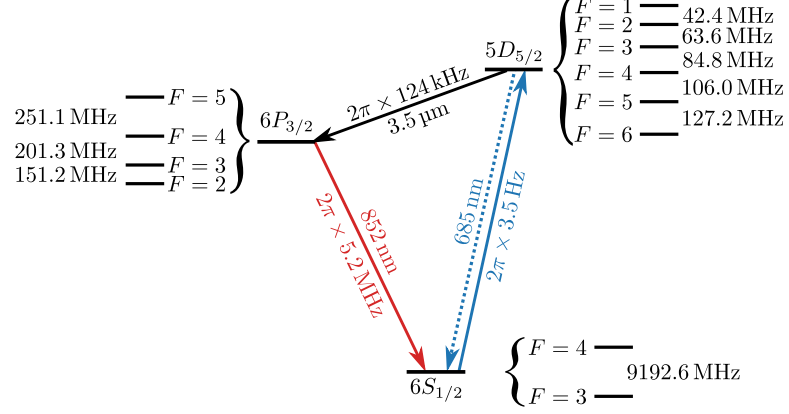


FIGURE 6.2: Cesium energy levels relevant to our experiment. We excite atoms via an electric quadrupole transition at a wavelength of 685 nm, and we detect the fluorescence emitted at a wavelength of 852 nm.

is in the $6S_{1/2}$ state. The further energy levels of cesium relevant for the present measurement are shown in Fig. 6.2.

We excite atoms from the $6S_{1/2}$ state to the $5D_{5/2}$ state via an electric quadrupole transition at a wavelength of 685 nm [248]. This transition features a partial decay rate of $\gamma_{D \rightarrow S} \approx 2\pi \times 3.5 \text{ Hz}$ [249], which is very small compared to the other transition rates in the present level scheme. From the excited state, most of the atoms, therefore, decay to the $6P_{3/2}$ state via an electric dipole transition at a wavelength of $3.5 \mu\text{m}$ [250]. A transition rate of about $\gamma_{D \rightarrow P} \approx 2\pi \times 124 \text{ kHz}$ was previously documented [237]. We emphasize that this transition rate is crucial for us because it primarily determines the lifetime of the $5D_{5/2}$ state. The atoms will dwell, on average, $\tau_P = 30.462(46) \text{ ns}$ [136] in the $6P_{3/2}$ -intermediate state, and then decay back to the ground state. We detect the fluorescence photons from the last transition at a wavelength of 852 nm. The decay rate of the $6P_{3/2} \rightarrow 6S_{1/2}$ transition is $\gamma_P \approx 2\pi \times 5.2 \text{ MHz}$.

We note that it would be advantageous to measure the fluorescence photons at a wavelength of $3.5 \mu\text{m}$ because, e.g., we expect much less radiation trapping for the $3.5 \mu\text{m}$ photons than for the 852 nm photons. However, we did not have a detector at this wavelength available. It is worth mentioning that the subsequently emitted fluorescence photons at the wavelengths of $3.5 \mu\text{m}$ and 852 nm are correlated and can be entangled [251–253].

6.2.2 Decay Model of a Three-Level System

We now derive a model to describe the decay of the emitted fluorescence. We consider the three-level system presented in Fig. 6.2. In a typical fluorescence measurement, we excite the atoms with laser light resonant with the $|6S_{1/2}, F = 4\rangle \rightarrow |5D_{5/2}\rangle$ -electric quadrupole transition. After $25\ \mu\text{s}$ of illumination, we switch the laser off. We can calculate the time evolution of the populations in the different states by solving the following rate equations

$$\dot{N}_D = -(\gamma_{D \rightarrow P} + \gamma_{D \rightarrow S})N_D + PN_S - PN_D, \quad (6.1)$$

$$\dot{N}_P = \gamma_{D \rightarrow P}N_D - \gamma_P N_P, \quad (6.2)$$

$$\dot{N}_S = \gamma_{D \rightarrow S}N_D + \gamma_P N_P - PN_S + PN_D, \quad (6.3)$$

where N_D , N_P , and N_S are the populations in the $5D_{5/2}$, $6P_{3/2}$, and $6S_{1/2}$ states, respectively. P is a pumping rate which depends on the laser settings. Since $\gamma_{D \rightarrow S} \ll \gamma_{D \rightarrow P}$, we neglect direct fluorescence on the electric quadrupole transition. Hence, the total decay rate from the $5D_{5/2}$ state, γ_D , is dominated by the decay to the $6P_{3/2}$ state and we make the approximation $\gamma_D = \gamma_{D \rightarrow P} + \gamma_{D \rightarrow S} \approx \gamma_{D \rightarrow P}$.

In our experiment, we switch the excitation laser on for a sufficiently long time to reach a steady state of the fluorescence intensity I_0 . Then, we turn the laser beam off and define the switch-off moment as the time $t = 0$. Here, we also define the initial parameters $N_{D0} = N_D(t = 0)$ and $N_{P0} = N_P(t = 0)$. Starting from the steady state at $t = 0$, we obtain the time-resolved fluorescence intensity, $I(t) \propto \dot{N}_S(t)$, as follows. When the laser is switched off ($P = 0$), we can solve equation 6.1, and find

$$N_D(t) = N_{D0}e^{-\gamma_{D \rightarrow P}t}. \quad (6.4)$$

We can use this together with the steady-state relation $\gamma_{D \rightarrow P}N_{D0} = \gamma_P N_{P0}$ to find the solution of equation 6.2

$$N_P(t) = N_{P0} \left\{ \frac{\gamma_P}{\gamma_P - \gamma_{D \rightarrow P}} e^{-\gamma_{D \rightarrow P}t} - \frac{\gamma_{D \rightarrow P}}{\gamma_P - \gamma_{D \rightarrow P}} e^{-\gamma_P t} \right\}. \quad (6.5)$$

We insert this in equation 6.3 to obtain the time-resolved fluorescence intensity

$$I(t) \propto \dot{N}_S(t) = I_0 \left\{ \frac{\gamma_P}{\gamma_P - \gamma_D} e^{-\gamma_D t} - \frac{\gamma_D}{\gamma_P - \gamma_D} e^{-\gamma_P t} \right\}, \quad (6.6)$$

6.2. Experimental Method and Setup

where $I_0 = \gamma_P N_{P0}$. Thus, the fluorescence signal is the sum of two exponential terms with decay rates γ_D and γ_P .

Since $\gamma_P \gg \gamma_D$, the contribution of the second term to the fluorescence signal is already small at $t = 0$. We ascertain a contribution of about 2% to the total intensity. Furthermore, the second term decays much faster than the first one. 500 ns after the laser switch-off, this term only contributes to about 2×10^{-9} of the total intensity. As discussed later, we start fitting the fluorescence signal at least 500 ns after the laser switch-off. We can, therefore, safely neglect the second term of equation (6.6). Hence, we fit our data only with a single exponential decay. As we will see below, we observe significant radiation trapping when we heat the atoms, and we, hence, use equation 6.6 to fit the fluorescence decay.

6.2.3 Laser Setup

Our experimental setup is illustrated in Fig. 6.3. First, we focus on the laser beam path. We use a tapered amplifier laser¹ to generate light at a wavelength of 685 nm. We term this laser the excitation laser. Directly after the output of the laser, a short pass filter² with a cut-off wavelength of 800 nm suppresses the amplified spontaneous emission of the laser around the detected wavelength of the fluorescence at 852 nm.

Then, we send the excitation laser beam through two AOMs. In both cases, we use the first diffraction order. By switching the RF power supplied to the AOMs, we can turn the excitation beam on and off. We send the beam through a commercial spectroscopy cell³ containing hot cesium vapor. In front of the vapor cell, the excitation beam has a power of about 21 mW and a beam diameter of about 1.2 mm resulting in an intensity of 2.3 W/cm^2 . This intensity is on the order of the saturation intensity of the $|6S_{1/2}, F = 4\rangle \rightarrow |5D_{5/2}\rangle$ -electric quadrupole transition [254]. Note that saturation broadening does not affect our lifetime results because the laser is off during the time interval in which we make our fits.

A single-photon counting module (SPCM⁴) detects the power of the excitation beam transmitted through the cell. This reference SPCM allows us to monitor the switch-off behavior of the laser. In Fig. 6.4, we present a typical signal of the reference SPCM during an experimental run. First, we observe a delay of about 500 ns between

¹Toptica, TA pro, LD-0690-0025-AR-1 and TA-0690-0500-1

²Thorlabs, FESH0800

³Thorlabs, GC25075-CS

⁴Excelitas Technologies, SPCM-AQRH-14-FC

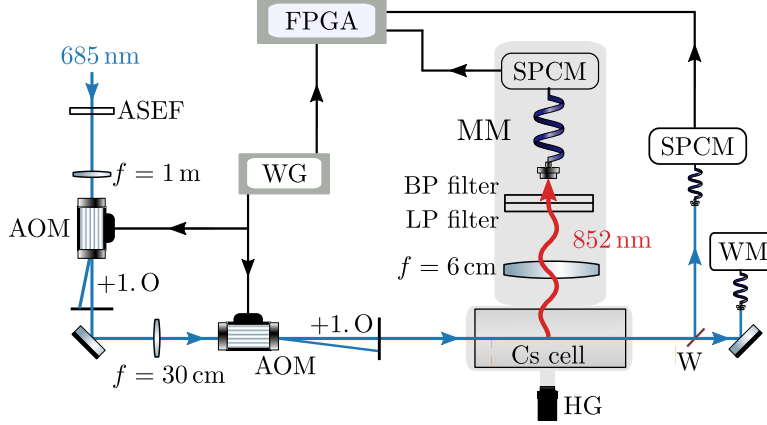


FIGURE 6.3: Illustration of our experimental setup. We send a laser beam at a wavelength of 685 nm through two acousto-optic modulators (AOM), and then to a cell containing cesium vapor. A single-photon counting module (SPCM) detects fluorescence photons at a wavelength of 852 nm. (+1. O, +1. order of diffraction; ASEF, amplified spontaneous emission filter; BP filter, bandpass filter; LP filter, longpass filter; MM, multi-mode optical fiber; WG, waveform generator; FPGA, field-programmable gate array; WM, wavelength meter; HG, heat gun)

the electronic signal commanding the excitation laser beam turn-off and the actual intensity decay. Then, the laser beam is suppressed to about 0.1 % of its initial power in a few tens of nanoseconds.

We continuously measure the laser frequency by sending part of the excitation beam after the cell to a wavelength meter⁵. To tune the laser into resonance with the $6S_{1/2} \rightarrow 5D_{5/2}$ transition, we obtain a fluorescence excitation spectrum at the beginning of each experimental run (see Appendix Sec. C). Subsequently, we tune the frequency of the laser in resonance with the $|6S_{1/2}, F = 4\rangle \rightarrow |5D_{5/2}\rangle$ transition. Then, we keep the laser frequency constant during the entire experimental run using the wavelength meter. An experimental run consists of several cycles, as we explain in section 6.2.5. We checked that drifts of the wavelength meter are irrelevant under our lab conditions and, thus, do not give rise to an error in the frequency stabilization of the excitation laser.

⁵HighFinesse, WS-6

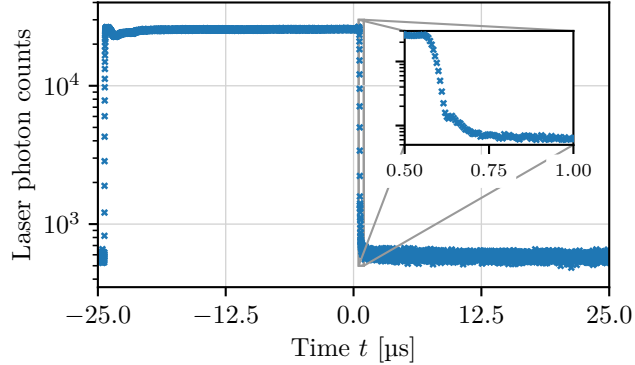


FIGURE 6.4: Typical measurement of the excitation beam power. Here, the sequence had a length of $50 \mu\text{s}$. We bin the photon counts with a binning length of 5 ns . In the beginning ($t = -25 \mu\text{s}$), we turn the excitation laser on. At $t = 0$, we turn it off. After a delay of about 550 ns , the laser power starts to drop. The inset shows a zoom of the relevant time interval. We see that the laser beam is suppressed to about 0.1% of its initial power in a few tens of nanoseconds.

6.2.4 Fluorescence Setup

In this section, we discuss our setup to collect and detect the fluorescence emitted by the cesium atoms in the vapor cell. Our vapor cell is a commercial cesium spectroscopy cell made of borosilicate glass. The cell has a length of 7.18 cm and a diameter of 2.54 cm . We enclose the cell inside a metal box. By letting heated air flow through the box, we control the temperature of the cell. To monitor the conditions inside the box, we install four temperature sensors⁶. We measure the temperature-dependent resistance of the sensors with an Arduino and take one data point every second. We take two of the sensors to define the temperature of the vapor cell. One is glued to the cell, and the other measures the temperature of the air close to the cell. We combine the temperature values from both sensors and use the average of these values as the temperature of the cesium atoms during the respective measurement.

We now discuss how we detect the fluorescence light emitted by the atoms. We collect the fluorescence emitted into a direction perpendicular to the excitation laser

⁶Epcos, B57861S103F40

beam path. To improve the collection efficiency, we use a lens with a focal length of 6 cm and a diameter of 5.08 cm. A long pass filter⁷ with a cut-off wavelength of 808 nm suppresses stray light at a wavelength of 685 nm that mainly stems from the excitation beam scattered off the various optical interfaces. A bandpass filter⁸, centered at 852 nm, further reduces background photon counts. We use a multi-mode optical fiber to guide the filtered fluorescence light onto an SPCM. We record the arrival times of the detected fluorescence photons and those of the reference SPCM signal using a field-programmable gate array (FPGA⁹).

6.2.5 Experimental Sequence

In an excitation cycle performed at room temperature, the excitation laser beam is switched on for 25 μ s. Meanwhile, the fluorescence signal reaches a steady state. The excitation laser is then switched off and stays off for 25 μ s. During the downtime, we measure a decay of the fluorescence. We repeat this cycle until we achieve an adequate counting statistic. At higher temperatures, radiation trapping of photons emitted at a wavelength of 852 nm slows down the fluorescence decay dynamics. Thus, we use longer experimental cycles to measure the decay of fluorescence longer until it is indistinguishable from the background dark counts.

We store the arrival times of photons detected by the fluorescence and the reference SPCMs using the FPGA. In the same way, we also record the electronic signal triggering the laser switch-off. We then compute the delay between the arrival time of each detected photon and the beginning of the respective experimental cycle. We bin the time delays using a binning size of 5 ns. Their histogram is shown in Fig. 6.5 (red dots). Note the logarithmic scale of the ordinate axis. The fluorescence signal starts at 4×10^4 counts/bin. It shows an exponential decay until background counts (about 600 counts/bin) begin to dominate. Moreover, a sharp switch-off behavior for the excitation laser light is observed (blue crosses). A typical experimental run consists of about 10^9 excitation cycles and takes about 14 hours. We detect a total of about 10^8 fluorescence photons during one measurement series, which corresponds to a rate of about 0.1 detected photons per excitation cycle.

⁷Semrock, BLP01-808R-25

⁸Semrock, LL01-852-12.5

⁹Opal Kelly, XEM3005-1200M32P

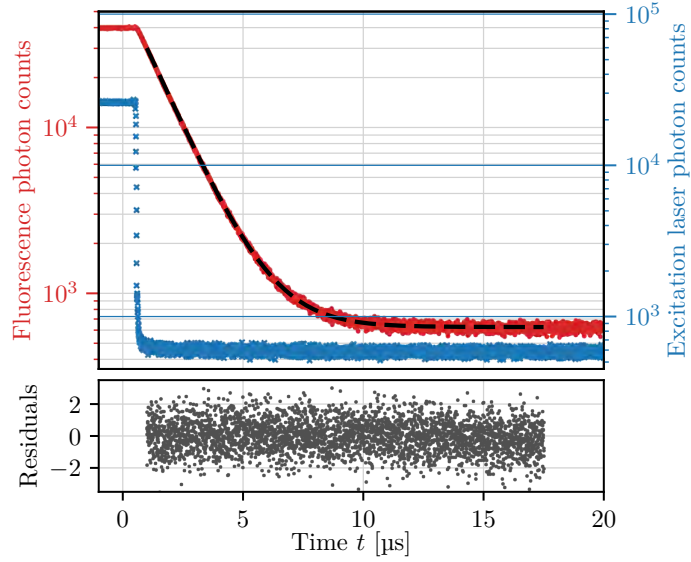


FIGURE 6.5: Typical lifetime measurement at room temperature. Top panel: a measurement of the atomic fluorescence (red dots) and the excitation laser (blue crosses) intensities. At $t = 0 \mu\text{s}$, we generate the trigger commanding the laser to switch off. We detect the signals with two separate SPCMs. We store the photon arrival times. From this data, we produce the photon count histograms using a bin length of 5 ns. The dashed black line is a fit of a single exponential decay with an offset. Bottom panel: normalized fit residuals for each time bin.

6.3 Results

In this section, we discuss the method we use to obtain the lifetime of the $5D_{5/2}$ state from the detected fluorescence decay. First, we present our fitting routine with the corresponding statistical error. Then, we further investigate the error of the lifetime measurement by analyzing long-term statistical fluctuations and various systematic errors.

6.3.1 Fit Method

We fit the raw data using the LMFIT python package¹⁰. This package provides a high-level interface to non-linear optimization and curve-fitting problems. It relies on a non-linear least-squares minimization method. We fit the measured fluorescence decay with

$$I^{(\text{fit})}(t) = I_0 \exp\left(-\frac{t}{\tau_D}\right) + c, \quad (6.7)$$

where t is the time. Our free fit parameters are the initial intensity, I_0 , the decay time constant, τ_D , and a constant offset, c . This offset takes background photons and detector dark counts into account. This way, we obtain $\tau_D = 1353.2(5)$ ns for the fluorescence decay shown in Fig. 6.5. The error of the fit result corresponds to the 68 % confidence interval.

6.3.2 Goodness of the Fit

We now discuss the goodness of the fit. We use four parameters for this verification: the normalized fit residuals r_i , the distribution of the normalized residuals, the Fourier transformation of the normalized residuals, and the reduced chi-squared, $\tilde{\chi}^2$.

We define the normalized fit residuals as

$$r_i = \frac{y_i - y_i^{(\text{fit})}}{\sigma_i} = \frac{y_i - y_i^{(\text{fit})}}{\sqrt{y_i}}, \quad (6.8)$$

where y_i ($y_i^{(\text{fit})}$) are the measured (fitted) photon counts in the i^{th} time bin, and σ_i is the standard deviation of the variable y_i . We assume that shot noise is the only present noise. The corresponding Poisson distribution leads to $\sigma_i = \sqrt{y_i}$. For the fit in Fig. 6.5, we present the respective fit residuals below the panel with the fluorescence photon counts. We cannot find any obvious unexpected behavior. For instance, no oscillations are visible.

Next, we bin the normalized residuals. We compare the resulting histogram with a Gaussian distribution centered on zero with a variance of one (see Fig. 6.6). They agree with each other, indicating that our fit is reasonably resembling the data. In our fitting workflow, we always also examine the Fourier transform of the residuals and find no prominent frequencies in the spectral densities.

¹⁰<https://lmfit.github.io/lmfit-py/>, last accessed on 2020-05-02

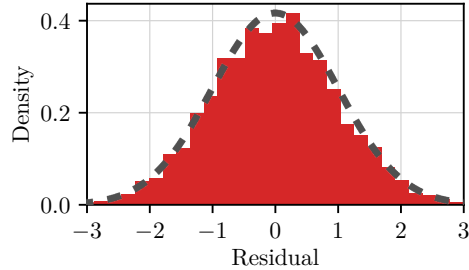


FIGURE 6.6: The distribution of the normalized fit residuals. The dashed gray line is a Gaussian distribution centered on zero with a variance of one.

In our fit model, the number of time bins, N , is large compared to the number of free parameters. Hence, we can define the reduced chi-squared, $\tilde{\chi}^2$, as the mean of the squared residuals

$$\tilde{\chi}^2 = \frac{1}{N} \sum_{i=1}^N r_i^2 . \quad (6.9)$$

A reduced chi-squared close to unity is an indicator of a good fit. $\tilde{\chi}^2 > 1$ indicates that the fit has not fully captured the data, and the fit model should be reconsidered, or that the error variance has been underestimated. $\tilde{\chi}^2 < 1$ is known as "overfitting" of the data. Either the model improperly fits noise, or, more probable, the error variance has been overestimated. For the fit in Fig. 6.5, we find $\tilde{\chi}^2 = 1.0009$. Since here $\tilde{\chi}^2 \approx 1$, we take that as another indication that our model is adequate for fitting our experimental data.

6.3.3 Fit Results and Statistical Fluctuations

Our fit routine provides a 68% confidence interval of every free fit parameter. This gives us a first estimate of the error of the lifetime inferred from the fit of the fluorescence decay. We find a confidence interval of about 0.5 ns for the lifetime of the $5D_{5/2}$ state.

However, the 68% confidence interval seems to underestimate fluctuations in our measurements. This was investigated by performing several independent experimental runs and comparing their results. We present the outcome of our entire campaign in Fig. 6.7. The individual measurements had approximately the same duration and the

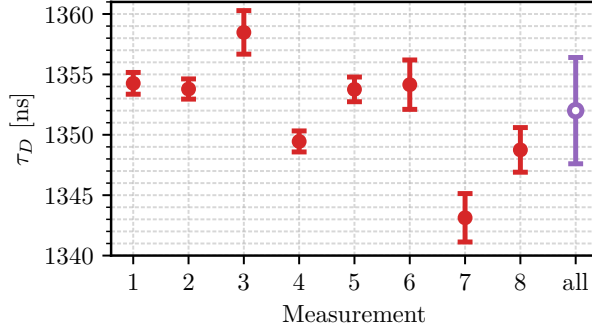


FIGURE 6.7: Fitted lifetime of the $5D_{5/2}$ state for six independent experimental runs (see main text for more details). The error bars take the 68% confidence interval of the fit and the truncation error into account, *i.e.*, the standard deviation of the fit result when varying the fitting range (cf. section 6.4.2). The purple data point “all” is an average of the eight detected lifetimes (red dots). We use this value as the outcome of our lifetime measurement at room temperature.

same photon count rate (see Tab. 6.2). We took them over a period of about eight weeks during six experimental runs. Data points 1 & 2 and 5 & 6 stem from the same measurement runs, which we divided into two subsets of equal sizes. The temperature during the measurements was between 22.5 °C and 24 °C, with a stability of about 0.4 °C within one measurement. Averaging the eight measured values, we obtain a mean lifetime of $\overline{\tau_D} = 1352.0$ ns, with a standard deviation of $\sigma_\tau = 4.4$ ns (cf. data point “all” in Fig. 6.7). In the following, we use $\overline{\tau_D}$ as the lifetime of the $5D_{5/2}$ state at room temperature.

We notice that the standard deviation of the eight measured lifetime values is larger than the individual error estimations from the fits. This indicates that the variations in our measurements arise from drifts of unknown origin rather than purely statistical fluctuations. Those drifts might occur at timescales comparable to or larger than a typical duration of an experimental run. Therefore, they are not captured by an error estimation of a single measurement. In this case, one can rescale the individual errors to take the observed variations into account or, alternatively, make an educated guess of the total error [255]. Here, we make a conservative choice and use the standard deviation of the measured lifetimes, $\sigma_\tau = 4.4$ ns, as an estimate of the error that is caused by the drifts. This error is included in our total error budget (see Tab. 6.4,

6.4. Systematic Errors

TABLE 6.2: Fitted lifetimes of the measurements used in Fig. 6.7. The quoted error takes into account both the fit confidence interval and the truncation error. “M.” is the measurement number. We also present the temperature during the measurement (“Temp.”), the measurement duration (“Dur.”), and the detected photons per cycle. For every measurement, the cycle duration was 50 μs . The point “all” is the unweighted average over the eight measured values.

M.	τ_D [ns]	Error [ns]	Temp. [$^{\circ}\text{C}$]	Dur. [h]	Photons/cycle
1	1354.3	0.9	22.8(4)	33.3/2	0.097
2	1353.8	0.8	22.8(4)	33.3/2	0.097
3	1358.5	1.8	22.8(3)	68.2	0.023
4	1349.5	0.9	23.9(4)	16.3	0.108
5	1353.8	1.0	22.6(3)	26.4/2	0.104
6	1354.2	2.0	22.6(3)	26.4/2	0.104
7	1343.1	2.0	23.7(3)	22.1	0.043
8	1348.8	1.8	23.8(3)	63.9	0.039
all	1352.0	4.4	23.1(6)		

“Other drifts”).

6.4 Systematic Errors

We now discuss systematic errors that can impact our lifetime measurement. Here, we focus on the effect of atomic collisions and the truncation error. Other systematic effects that turn out to be negligible in our system are summarized in Appendix Sec. D.

6.4.1 Effect of Atomic Collisions

Collisional broadening occurs when atoms collide with other atoms or with the wall of the vapor cell while they are excited. In particular, inelastic collisions can shorten the lifetime of the excited state [256]. Therefore, these collisions can influence our measurements. The collision rate depends on the atomic number density n as well as on the cesium pressure in the cell P_{Cs} . This pressure can be connected to the temperature T of the cell via a vapor-pressure model [257]. For temperatures below

$T = 28.44^\circ\text{C}$, where cesium is solid at usual pressures, it states

$$\log_{10} P_{\text{Cs}} = -219.482 + \frac{1088.676}{T} - 0.08336185T + 94.88752 \log_{10} T, \quad (6.10)$$

where P_{Cs} has the unit torr and T the unit K. For higher temperatures, cesium is in the liquid phase and the vapor-pressure model predicts

$$\log_{10} P_{\text{Cs}} = 8.22127 + \frac{4006.048}{T} - 0.00060194T + 0.19623 \log_{10} T. \quad (6.11)$$

According to the semiclassical Lindholm-Foley model, the total decay rate of the $5D_{5/2}$ state γ_D can be written as [258, 259]

$$\gamma_D = \gamma_{D,0} + \gamma_{D,\text{coll}}, \quad (6.12)$$

where $\gamma_{D,0}$ is the natural decay rate and $\gamma_{D,\text{coll}}$ is the collision-induced decay rate. We can write $\gamma_{D,\text{coll}}$ as

$$\gamma_{D,\text{coll}} = A \times \frac{P_{\text{Cs}}}{T^{0.7}}, \quad (6.13)$$

where T is the temperature of the cesium vapor, P_{Cs} is the partial cesium pressure in the cell, and A is a constant which needs to be determined. The exponent 0.7 follows from the Lindholm-Foley impact theory, see e.g. [260].

At higher temperatures, we cannot neglect radiation trapping. As an example, we present a measurement at a temperature of $98(1)^\circ\text{C}$ in Fig. 6.8. We see that the fluorescence decay is significantly longer. Hence, we use equation 6.6 to fit the decay. We use γ_D , γ_P , I_0 , and a constant offset c as our free fit parameters. The fit in Fig. 6.8 yields a $5D_{5/2}$ -lifetime of $\tau_D = 874(16)$ ns and an apparent $6P_{3/2}$ -lifetime of $\tau_P = 5.87(1)$ μs . The $5D_{5/2}$ -lifetime is shorter than at room temperature because of inelastic collisions. The $6P_{3/2}$ -lifetime is influenced by both, radiation trapping and inelastic collisions. However, radiation trapping clearly dominates and makes the $6P_{3/2}$ -lifetime appear much longer than the natural lifetime. Although we see small oscillations in the fitting residuals, we find $\tilde{\chi}^2 = 1.02$, which is still acceptable.

In Fig. 6.9, we present lifetime measurements at different temperatures T . We discuss the data of the individual measurements and fits in Tab. 6.3. Note that we use ND filters at high temperatures to decrease the detected photon rate and prevent a saturation of the SPCM. In Fig. 6.9(a), we depict $\gamma_D = 1/\tau_D$ as a function of the

6.4. Systematic Errors

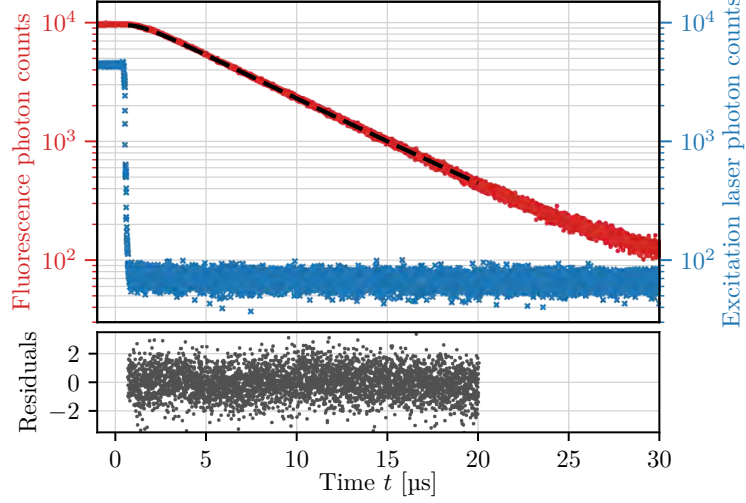


FIGURE 6.8: A lifetime measurement at a temperature of 98(1) °C. In the upper panel, we present the detected fluorescence (red dots) and the turn-off behavior of the excitation laser (blue crosses). Radiation trapping makes the fluorescence decay significantly longer. We use equation 6.6 to fit the decay (dashed black line) and find a shorter $5D_{5/2}$ -lifetime (see main text). In the lower panel, we depict the residuals. We find $\tilde{\chi}^2 = 1.02$.

parameter $x = P_{Cs}/T^{0.7}$. The latter is varied by changing T , which also results in a variation of P_{Cs} . We also present τ_D depending on the parameter $x = P_{Cs}/T^{0.7}$ in Fig. 6.9(b). We perform a linear fit of γ_D weighted with the error of the individual γ_D (see Fig. 6.9(a)). This fit yields $A = 300(30) \mu\text{s}^{-1} \text{Pa}^{-1} \text{K}^{0.7}$.

The measurements shown in Fig. 6.7 were carried out at a temperature of 23(1) °C. At this temperature, we expect a partial pressure of 1.4×10^{-6} mbar, corresponding to $x = 2.6 \times 10^{-6} \text{Pa K}^{-0.7}$. With that, we calculate an estimated collision-induced decay rate of $\gamma_{D,\text{coll}} = 7.8(8) \times 10^{-4} \mu\text{s}^{-1}$. Therefore, the total lifetime of 1352 ns features a systematic error of 1.4(1) ns due to collisions. Finally, the temperature error of about 1 °C in our measurements results in an additional uncertainty of 0.1 ns, which we add to our error budget.

TABLE 6.3: Fitted lifetimes for the measurements used in Fig. 6.9. The quoted error takes into account both the fit confidence interval and the truncation error (“Error”). We present the temperature during the measurement (“Temp.”), the measurement duration (“Dur.”), the detected photons per cycle, and the cycle duration (“Cycle Dur.”).

Temp. [°C]	τ_D [ns]	Error [ns]	Dur. [h]	Cycle dur. [μ s]	Photons/cycle
22.6(3)	1354	2	26.4	50	0.104
37.7(6)	1357	2	18.6	100	0.188
62.5(6)	1321	7	15.3	250	0.374
63(2)	1335	17	12.9	40	0.0564
63(1)	1316	8	20.3	100	0.927
73(1)	1248	100	13.5	250	3.54
92(2)	991	37	14	40	0.245
98(1)	874	22	15.3	250	1.092
104(2)	937	187	12.8	200	2.977
108(2)	860	50	11.2	200	2.29
116(2)	470	75	12.9	250	0.527

6.4.2 Truncation Error

The truncation error results from variation in the inferred lifetime when varying the fitting interval. We only consider data that was recorded at least 500 ns after the actual laser switch-off. This is done to neglect the contribution of the $6P_{3/2}$ state lifetime in the fluorescence signal. In order to find the optimum start and stop times of the fit, we ran the fitting routine while scanning the fitting range in a two-dimensional way. For each iteration, we checked the reduced chi-squared and the 68 %-confidence interval of the fit results.

In Fig. 6.10, we present the results of this analysis for the measurement shown in Fig. 6.5. We scanned the fitting interval over a broad range to find a region where $\tilde{\chi}^2$ is close to one. In Fig. 6.10(a), we depict the inferred lifetime τ_D of all fit intervals. In Fig. 6.10(b), we present the corresponding values of $\tilde{\chi}^2$. We find that the fit works well for start and stop times ranging from 0.9 μ s to 1.3 μ s and 13 μ s to 17 μ s after the laser switch-off, respectively (see black rectangles in Fig. 6.10). We estimate the truncation error by computing the standard deviation of the fit result when varying the start and

6.5. Final Lifetime with Total Error Budget

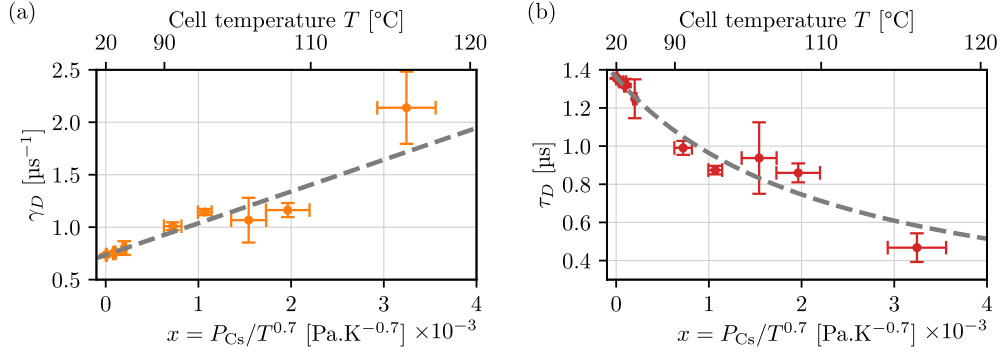


FIGURE 6.9: (a) Fitted decay rate, $\gamma_D = \gamma_{D,0} + \gamma_{D,\text{coll}}$, of the $5D_{5/2}$ state as a function of $x = P_{\text{Cs}}/T^{0.7}$. As expected, the collisional decay rate scales linearly with x . A linear fit (solid line) yields a slope of $300(30) \mu\text{s}^{-1} \text{Pa}^{-1} \text{K}^{0.7}$. The error bars take into account both the fit 68% confidence interval and the truncation error (cf. section 6.4.2). (b) Lifetime, $\tau_D = 1/\gamma_D$, of the $5D_{5/2}$ state as a function of x . The solid line corresponds to the linear fit on the decay rate shown in (a). We present the cell temperature, T , at the top of the figure.

stop time within this range. For the present measurement, we find a mean lifetime of 1354 ns, a truncation error of 1 ns, and a reduced chi-squared of 0.993(5). For the measurement campaign shown in Fig. 6.7, we obtain a mean truncation error of 0.9 ns, and a mean reduced chi-squared of 1.01(2).

6.5 Final Lifetime with Total Error Budget

In Tab. 6.4, we summarize the final error budget. We add the total correction of +1.4 ns to the lifetime value of 1352.0 ns that we found in our measurement campaign discussed in Sec. 6.3.3. Together with a total error budget of 4.6 ns, we obtain a final lifetime of the $5D_{5/2}$ state of 1353(5) ns.

In Fig. 6.11, we compare the result of our measurements to previous measurements and calculations. Our final $5D_{5/2}$ lifetime is longer than what was measured before. In particular, our result disagrees with the measurements of Hoeling *et al.* [236] and DiBerardino *et al.* [237] beyond the stated error bars. However, the theoretical studies of Safronova *et al.* [243, 245] predicted a lifetime of the $5D_{5/2}$ state, which agrees within the error bars with our measurement. Their calculations are based on precise

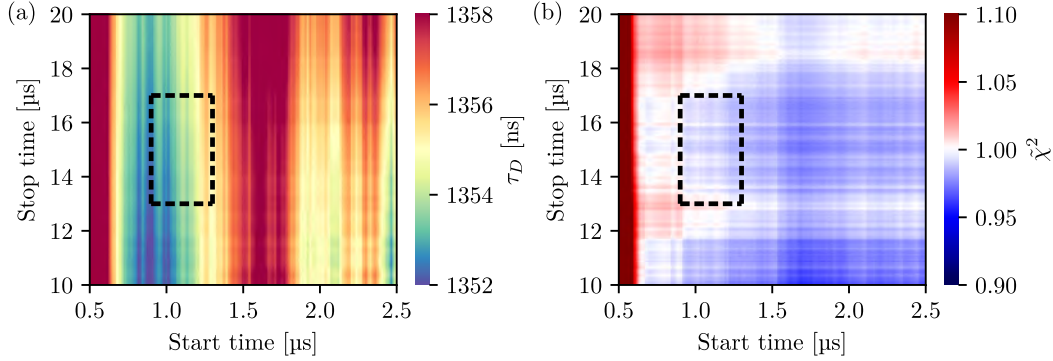


FIGURE 6.10: Analysis of τ_D for various fitting intervals. We scan the fitting range in a two-dimensional way to find the truncation error of the measurement shown in Fig. 6.5. (a) τ_D in a broad range of fitting intervals. (b) the $\tilde{\chi}^2$ corresponding to the values of τ_D in (a). To find the truncation error, we consider the area framed by the dashed black lines in (a) and (b). In this area, $\tilde{\chi}^2$ is close to one. We estimate the truncation error by computing the standard deviation of the fit result.

measurements of the cesium $6P$ -state polarizabilities. Hence, we conclude that our result is consistent with these polarizabilities.

6.6 Summary and Outlook

In conclusion, our measurements contribute to resolving a long-standing disagreement between a number of experimental and theoretical results of the lifetime of the $5D_{5/2}$ state. Specifically, we obtain a final value of 1353(5) ns for this lifetime which should be consistent with known values of the cesium $6P$ -state polarizabilities [243]. Note that our results are not compatible with the theoretical studies of Sahoo [244] which are consistent with the lifetime measured by DiBerardino *et al.* [237]. In order to improve the traceability of our measurements and analysis, we provided the raw experimental data in an open-access repository [261] (see Appendix Sec. E). We hope that our results support future theoretical predictions of atomic properties and will help resolve the current discrepancy between different theoretical calculations of the cesium $5D_{5/2}$ state lifetime.

6.6. Summary and Outlook

TABLE 6.4: summary of the corrections and errors used to infer the final value of the $5D_{5/2}$ -state lifetime. For the error arising because of collisional broadening, there are two contributions arising from the temperature uncertainty and from the uncertainty in the measurement of the collision-induced decay rate. The error of other drifts results from the measurements discussed in section 6.3.3.

Source	Correction [ns]	Error [ns]
Fit confidence interval		1.0
Collisional broadening	+1.4	$0.1 + 0.1$
FPGA accuracy		< 0.1
SPCM dead time		< 0.1
Quantum beats		< 0.1
Truncation error		0.9
Other drifts		4.4
Total	+1.4	4.6

Although our measurement of the lifetime of the cesium $5D_{5/2}$ state is the most precise reported so far, it could be improved, e.g., by continuously measuring the pressure in the vapor cell. Also, it would be advantageous to detect the fluorescence decay of the $3.5\ \mu\text{m}$ photons emitted on the $5D_{5/2} \rightarrow 6P_{3/2}$ transition to eliminate any contributions of the lifetime of the $6P_{3/2}$ state. Beam shaping could be used to improve the scattering rate and the emitted fluorescence. For example, the steep evanescent field gradient of an optical nanofiber can be used to drive electric quadrupole transitions [251, 262]. In this context, it would be interesting to study the alteration of the lifetime of the $5D_{5/2}$ state close to an optical nanofiber.

By changing the wavelength of the excitation laser to 689 nm, our experimental setup is suitable to measure the lifetime of the $5D_{3/2}$. Also for this state, discrepancies between the measured [237] and the calculated [243, 244] are reported. Overcoming these inconsistencies and further improving the knowledge of the electronic structure of cesium can boost the test of parity non-conservation. Moreover, it will be beneficial for fundamental studies of atomic physics in general.

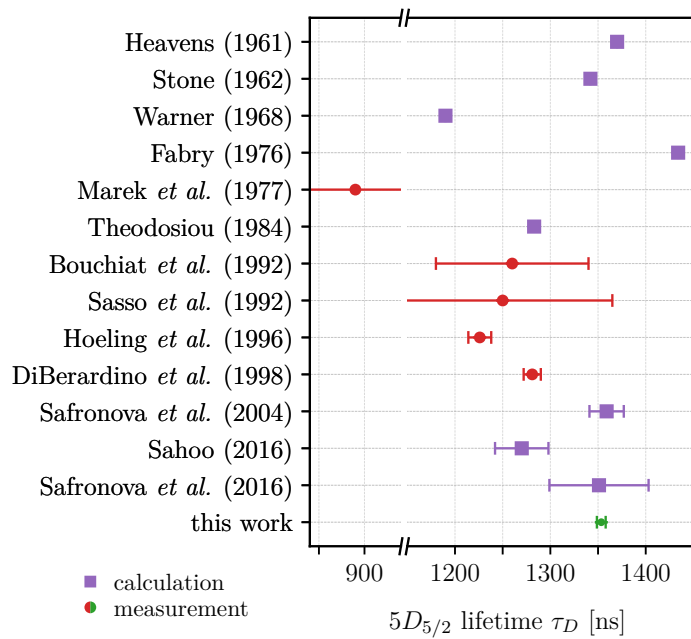


FIGURE 6.11: Review of literature values of the $5D_{5/2}$ -state lifetime (cf. Tab. 6.1). We compare our final results (green circle) with available calculations (purple squares) and experimental results (red circles). Our value agrees with the theoretical studies of Safronova *et al.* [243, 245] but disagrees with the measurements of Hoeling *et al.* [236] and DiBerardino *et al.* [237] beyond the stated error bars.

Chapter 7

Conclusion and Outlook

In this thesis, we have studied properties of cesium atoms and used them to create non-reciprocal nanophotonic systems. Typically, one needs either the magneto-optical effect, a temporal modulation, or an optical nonlinearity to break reciprocity [59]. By contrast, in our system, the non-reciprocal response arises from the propagation direction-dependent local polarization of the nanofiber-guided light in conjunction with polarization-dependent atom-light coupling. Based on that, we proposed and experimentally demonstrated non-reciprocal amplification of a fiber-guided light field. Moreover, we used the chiral coupling in our system to experimentally demonstrate anti-symmetric non-reciprocal phase shifts of the guided light field.

We used Raman gain in our amplification scheme. As demonstrated, we can control the direction of amplification via the spin state of the atoms. In particular, we showed that we do not need an external magnetic field for the non-reciprocal response. Moreover, no temporal modulation is involved, e.g., by an optical pump field that shares the same spatial mode as the signal field. Finally, in contrast to non-linear schemes, our scheme is capable of handling signal fields that simultaneously propagate in both directions through the device. We conclude that our approach of breaking reciprocity is qualitatively different from the textbook examples. Building on that, we also measured a non-reciprocal phase shift of the fiber-guided light field. We proposed and experimentally demonstrated a scheme where the phase shift is antisymmetric. Our results are relevant, e.g., for protecting sensitive light sources from undesired feedback, for the construction of new optical isolators, and for simplifying the design of optical networks. Notably, our schemes could be implemented in other nanophotonic systems, including those implemented on-chip.

The future experimental studies of non-reciprocity in our system will, most likely, focus on magnetic field-free atomic spin controlled non-reciprocal phase shifts, the

implementation of a gyrator [59, 222], and unidirectional lasing. Our results on EIT might also pave the way towards all-optical switching [263] and a new cooling scheme for the nanofiber-trapped atoms based on EIT [127, 264].

In this thesis, we also made a contribution to the fundamental understanding of atoms by measuring the lifetime of the cesium $5D_{5/2}$ state. We obtained a final lifetime of 1353(5) ns. This value disagrees with the latest experimental results [236, 237], while it agrees with theoretical calculations [243, 245]. In the future, we might measure more lifetimes of alkali metals, including other states of cesium. The most obvious choice is the measurement of the lifetime of the cesium $5D_{3/2}$ state. With a small modification to our experimental setup, we could excite the atoms to this state using a laser with a wavelength of 689 nm. Also for this state, disagreements between the latest measurement [237] and the theory have been reported [243, 245].

Appendices

Appendix A

Derivation of the Frequency Dependence of the Phase Shift

Here, we discuss the frequency dependence of the phase shift of a laser field that interacts classically with an atom that we treat as a dipole with a resonance frequency. We follow the derivation of the linear Lorentz oscillator model in [265], but we note that similar discussions can be found in several textbooks. The atom can be described with an electron with mass m , which is harmonically bound at $\mathbf{r}_e = 0$. We model the motion of the electron with a damped harmonic oscillator that is driven by a periodic force $\mathbf{F}(\omega)$

$$\ddot{\mathbf{r}}_e + \gamma\dot{\mathbf{r}}_e + \omega_0^2\mathbf{r}_e = \frac{1}{m}\mathbf{F}(\omega) , \quad (\text{A.1})$$

where \mathbf{r}_e is the displacement of an electron from the steady-state, γ the energy decay rate, ω_0 the resonance frequency of the dipole oscillator, and m is the mass of an electron. We now apply an optical field which oscillates with a frequency ω close to ω_0

$$\ddot{\mathbf{r}}_e + \gamma\dot{\mathbf{r}}_e + \omega_0^2\mathbf{r}_e = \frac{e}{m}\mathbf{E}_0e^{i(\mathbf{k}\cdot\mathbf{r}-\omega t)} , \quad (\text{A.2})$$

where \mathbf{E}_0 is a constant amplitude and e the elementary charge. When we solve this equation, we find

$$\mathbf{r}_e = \frac{e}{m} \frac{\mathbf{E}_0 e^{i(\mathbf{k}\cdot\mathbf{r}-\omega t)}}{\omega_0^2 - \omega^2 - i\omega\gamma} . \quad (\text{A.3})$$

This shows that the electron position \mathbf{r}_e oscillates with the same frequency ω as the driving field. The polarization of a linear dielectric material with N dipoles $\mathbf{d} = e\mathbf{r}_e$ is

given by

$$\mathbf{P} = N e \mathbf{r}_e = \frac{N e^2}{m} \left(\frac{1}{\omega_0^2 - \omega^2 - i \omega \gamma} \right) \mathbf{E}_0 e^{i(\mathbf{k} \cdot \mathbf{r} - \omega t)}. \quad (\text{A.4})$$

We compare this with Eq. 1.5 and obtain an electric susceptibility of

$$\chi(\omega) = \frac{N e^2}{\epsilon_0 m} \frac{1}{\omega_0^2 - \omega^2 - i \omega \gamma}. \quad (\text{A.5})$$

In general, $\chi(\omega)$ is a complex number which leads to a complex refractive index

$$\tilde{n}(\omega) = n(\omega) + i \kappa(\omega) = \sqrt{1 + \chi(\omega)}, \quad (\text{A.6})$$

where n is the real part and κ is the imaginary part of the refractive index. We assume $\gamma \ll \omega_0$, and that the driving field frequency ω is tuned close to ω_0 , i.e., the detuning $\Delta = \omega - \omega_0$ is small. Therefore, we can make the approximations [266]

$$\begin{aligned} \omega^2 - \omega_0^2 &= (\omega + \omega_0)(\omega - \omega_0) \approx 2\omega_0(\omega - \omega_0) = 2\omega_0 \Delta, \\ \omega \gamma &\approx \omega_0 \gamma. \end{aligned} \quad (\text{A.7})$$

Then, we solve for the real part of the electric susceptibility [94]

$$\Re(\chi(\omega)) = -\frac{N e^2}{\epsilon_0 m} \frac{2\omega_0 \Delta}{4\omega_0^2 \Delta^2 + \omega_0^2 \gamma^2}. \quad (\text{A.8})$$

In a weakly absorbing medium, we can approximate the real part of the refractive index as [94]

$$n(\omega) \approx \sqrt{1 + \Re(\chi(\omega))} \approx 1 + \frac{1}{2} \Re(\chi(\omega)). \quad (\text{A.9})$$

The phase difference between two fields is proportional to the difference of the real parts of the refractive indices Δn . We assume now that one field is the reference field which propagates in a medium with a refractive index of one and find [256]

$$\begin{aligned} \Delta \phi &= \frac{2\pi L}{\lambda} \Delta n = \frac{2\pi L}{\lambda} (n - 1) = \frac{\pi L}{\lambda} \Re(\chi(\omega)) \\ &= -2\phi_{\max} \frac{\tilde{\Delta}}{\tilde{\Delta}^2 + 1}, \end{aligned} \quad (\text{A.10})$$

Appendix A. Derivation of the Frequency Dependence of the Phase Shift

where $\tilde{\Delta} = 2\Delta/\gamma$ is the detuning of the probe laser from the transition resonance frequency, normalized to the half width at half maximum of the atomic linewidth, $\gamma/2$. Here, the maximal phase difference ϕ_{\max} occurs at $\tilde{\Delta} = 1$ and is given by

$$\phi_{\max} = \frac{\pi L N e^2}{2\lambda \epsilon_0 m \omega_0 \gamma} . \quad (\text{A.11})$$

Appendix B

Theoretical Aspects of Lifetimes

Here, we deal with theoretical aspects of the radiative lifetime of a state. A lifetime is connected to the theory of spontaneous emission, which can be described by the Wigner-Weisskopf theory [267]. This theory shows that an atom in the excited state decays exponentially into other states due to fluctuations of the quantized vacuum field [181].

We study the time-dependent population densities of a two-level system. For our discussion, it is sufficient to describe this system with rate equations. Let us assume N_e atoms in the excited state and N_g atoms in the ground state. The rate equations are

$$\dot{N}_e(t) = -\gamma N_e , \quad (\text{B.1})$$

$$\dot{N}_g(t) = +\gamma N_e , \quad (\text{B.2})$$

where γ is the transition rate between the two states. The solution of the first rate equation is

$$N_e(t) = N_0 e^{-\gamma t} , \quad (\text{B.3})$$

with $N_0 = N_e(t = 0)$, i.e., N_0 is the initial number of atoms in the excited state. The atoms will decay exponentially from the excited state to the ground state. The probability per unit time dP_{eg}/dt that an excited atom makes a transition to a lower level via spontaneous emission of a photon depends on the structure of the atom and the selected transition $|e\rangle \rightarrow |g\rangle$ [256]. Also, it is related to the Einstein coefficient A_{eg} via [268]

$$\frac{dP_{eg}}{dt} = A_{eg} . \quad (\text{B.4})$$

A_{eg} is also known as the transition rate γ . We define the lifetime τ_e of the excited state as the time after $1/e$ of the population is still in the excited state, i.e., $N_e(\tau_e) = N_0 e^{-1}$. This lifetime is connected to the transition rate, the linewidth $\Delta\omega$, and the energy uncertainty ΔE

$$\frac{1}{\tau_e} = \gamma = \Delta\omega = \frac{\Delta E}{\hbar} . \quad (\text{B.5})$$

For a two-level system with a linear dipole, the lifetime of a state is connected to the reduced matrix element $\langle\psi_g|\mathbf{d}_z|\psi_e\rangle$ via the following expression [269]

$$\gamma = \frac{8\pi^2\nu^3}{\epsilon_0\hbar c^3} |\langle\psi_g|\mathbf{d}_z|\psi_e\rangle|^2 , \quad (\text{B.6})$$

where ν is the frequency of the transition, ϵ_0 is the vacuum permittivity, \hbar is the Planck constant, and c is the speed of light. To calculate the reduced matrix element, the wavefunctions $|\psi_g\rangle$ and $|\psi_e\rangle$ have to be known precisely. Lifetime measurements of a state can be a test for theoretical predictions of wavefunctions [270, 271].

Under ideal conditions, the lifetime of a state is a physical constant. Some effects, however, can alter this lifetime or lead to an apparent lifetime in measurements. For example, collisional broadening can shorten the lifetime [256]. This broadening results from, e.g., inelastic collisions between atoms. The excitation energy of one atom can be either partly or entirely transferred into the internal energy of a second atom leading to a faster decrease of the number of atoms in the excited state. It is common to call them quenching collisions because they quench the fluorescence intensity [256]. The collision rate depends on the density of the atomic vapor and, thus, on the pressure inside the vapor cell, which can be deduced from the temperature [257]. Also, radiation trapping depends on the pressure inside a vapor cell (see Appendix Sec. D.1). On the contrary, it can lead to considerably longer apparent lifetimes meaning that the measured lifetime may seem longer than it is [8].

Appendix C

Spectrally Resolved Fluorescence Measurement

In Fig. C.1, we present a fluorescence excitation spectrum. We excite atoms with the excitation beam and measure the secondary fluorescence at a wavelength of 852 nm. We scan the frequency of the excitation laser over the resonances of the $|6S_{1/2}, F = 4\rangle \rightarrow |5D_{5/2}, F' = 2 - 6\rangle$ transitions. While scanning, we record the absolute frequency of the laser with a wavelength meter. A calibration of the wavelength meter previously unveiled a frequency offset of 0.85 GHz which we subtract from the detected frequency [224]. Simultaneously, we continuously count how many photons the SPCM detects in 20 ms. We find a Doppler-broadened fluorescence signal leading to an unresolved hyperfine spectrum of the transition. Similar to [254], we superimpose five Gaussian functions to fit the detected fluorescence. The relative intensities of the lines are given by [254, 272]

$$S_{FF'}^Q = (2F' + 1) (2J + 1) \left\{ \begin{array}{ccc} J & J' & 2 \\ F' & F & I \end{array} \right\}^2, \quad (\text{C.1})$$

where F , J , and I are the respective quantum numbers of the transition. We can, therefore, use the relative intensities together with the relative frequencies of the hyperfine levels as fixed parameters. We perform the fit with four free fit parameters: a global amplitude, a global frequency shift, a common FWHM of each Gaussian, and a global offset. We find that the FWHM of the Gaussians is $\Delta\nu_{\text{Dopp}} = 477(4)$ MHz. This is in good agreement with theoretical calculations based on the velocity distribution of the atoms predicting a Doppler width of ~ 465 MHz for our experimental situation [224].

The hyperfine splitting of the ground state is ~ 9.2 GHz, i.e., much broader than

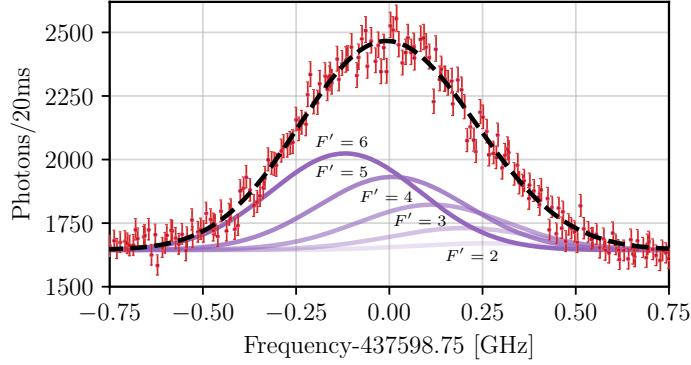


FIGURE C.1: Fluorescence excitation spectrum. We scan the frequency of the excitation laser over the $|6S_{1/2}, F = 4\rangle \rightarrow |5D_{5/2}, F' = 2 - 6\rangle$ transitions. We count for a time of 20 ms the photon detection events. We find a Doppler-broadened fluorescence signal (red dots). We fit the measurement with five superimposed Gaussian functions with predefined relative frequencies and amplitudes (dashed black line). We plot the individual Gaussian functions with solid purple lines and labeled them with the corresponding quantum numbers F' of the $5D_{5/2}$ state.

the Doppler broadened linewidth (see Fig. 6.2). Hence, we can resolve the hyperfine structure of the $6S_{1/2}$ ground state. All lifetime measurements in this thesis are performed with the excitation laser tuned to the $|6S_{1/2}, F = 4\rangle \rightarrow |5D_{5/2}\rangle$ transition. We excite atoms to all the hyperfine F -states of the $5D_{5/2}$ state because the hyperfine structure of this state is unresolved. Since all of these states are expected to have the same lifetime, this has no effect on the outcome of our measurement.

Appendix D

Other Systematic Errors of the Lifetime Measurement

In this section, we summarize the study of systematic errors that, in the end, turn out to be negligible in our system. First, we study radiation trapping and then, we analyze the FPGA accuracy and the SPCM dead time. Finally, we also discuss other systematic errors that are also not influencing the outcome of our analysis.

D.1 Radiation Trapping

When an atom in a vapor cell emits a photon, it can be reabsorbed by another atom. This effect depends on the length and the density of the atomic sample and is also known as radiation trapping. In general, radiation trapping can increase the measured lifetime of an atomic state substantially [271]. In our experiment, the population of atoms in the $6P_{3/2}$ state is small. Therefore, we expect no reabsorption of photons emitted at a wavelength of $3.5\ \mu\text{m}$ (cf. Fig. 6.2). Since most of the atoms are in the $6S_{1/2}$ state, subsequently emitted photons at a wavelength of $852\ \text{nm}$ can be reabsorbed by other atoms in the vapor cell. Hence, the apparent lifetime of the $6P_{3/2}$ state will be increased.

In the actual experiment, the $6P_{3/2}$ decay will not be described by a single exponential [236]. Mathematically, we can describe radiation-trapping with the Holstein radiation-trapping equation [273, 274]. This equation is an integro-differential equation for the density of excited atoms. For a given geometry, there is an orthogonal set of eigenmodes. These eigenmodes are also known as the Holstein modes. Each mode will

decay exponentially with a time constant

$$\tau_P^{(i)} = g_i \tau_P, \quad (\text{D.1})$$

where i is the mode index and g_i the Holstein radiation trapping factor [275].

We compute the eigenmodes for an infinite cylinder geometry and a Doppler broadened ensemble of atoms. The fluorescence signal can be expressed as the sum of the series of these eigenmodes. In this situation, the trapping factors g_i can be defined as [275]

$$g_i^D = 1 + \frac{1}{m_i^D} \cdot \alpha_0 R \sqrt{\ln \left(\frac{\alpha_0 R}{2} + e \right)} - \frac{c_{0i}^D \alpha_0 R \ln(\alpha_0 R) + c_{1i}^D \alpha_0 R + c_{2i}^D (\alpha_0 R)^2}{1 + c_{3i}^D \alpha_0 R + c_{4i}^D (\alpha_0 R)^2}, \quad (\text{D.2})$$

where R is the radius of the cell and α_0 is the absorption coefficient at the line center. The coefficients m_i^D defines the behavior at a high OD ($\alpha_0 R \gg 1$) and can be found in the literature [275, 276]. In [275], the coefficients c_{ni}^D were calculated. We can approximate the detuning dependent absorption cross section $\sigma(\delta)$ by a rectangular function with a width of γ_P . In the limit of $\Gamma \ll \Delta\nu_{\text{Dopp}}$, we find

$$\alpha_0 = n\sigma = \int n(\delta)\sigma(\delta)d\delta \approx \frac{n_0\gamma_P\sigma_0}{\sqrt{2\pi}\Delta\nu_{\text{Dopp}}}, \quad (\text{D.3})$$

where n is the atomic density, δ is the laser detuning, and $\sigma_0 = \frac{3\lambda^2}{2\pi}$. For the measurements carried out at a temperature of 23 °C, we expect $n(\delta) = n_0 \approx 3.4 \times 10^{10} \text{ cm}^{-3}$, corresponding to an attenuation factor of $\alpha R \approx 0.66$. For this setting, we calculate the first three trapping factors g_i and find

- $g_1 = 1.6223$,
- $g_2 = 1.1753$,
- $g_3 = 1.1003$.

The largest Holstein factor g_1 thus corresponds to a $\sim 60\%$ increase of the $6P_{3/2}$ state lifetime at room temperature. This results in an apparent $6P_{3/2}$ state lifetime of $\tau_P^1 = 48.6 \text{ ns}$. For the considered fitting ranges (cf. section 6.2.2), the contribution of the $6P_{3/2}$ state to the apparent lifetime of the $5D_{5/2}$ state is therefore negligible, even in the presence of radiation trapping.

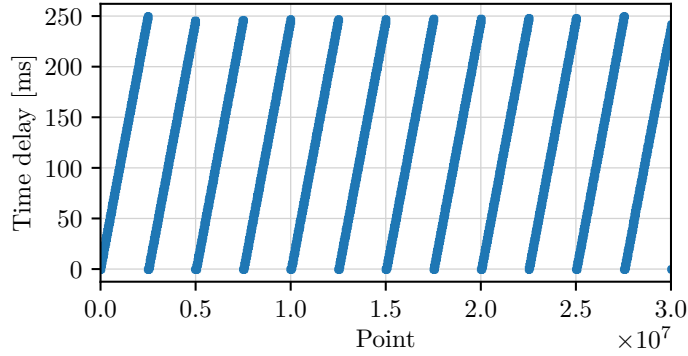


FIGURE D.1: Delay of time-tags with respect to the first time-tag of the measurement. The FPGA records the times of every period of a sinus with a frequency of 10 MHz. The delays with respect to the first time-tag show that the FPGA clock is set to 0 s every 250 ms.

D.2 FPGA Accuracy

To check the accuracy of the FPGA clock, we compare it to a reference signal from a rubidium-based atomic clock¹. The clock provides a sinus signal with a frequency of 10 MHz. We send this signal directly to the FPGA, which was set to record one time-tag per period of the sinus. The FPGA stores the time-tags in picoseconds in a file on a computer. We computed the time delays between two time-tags. In Fig. D.1, we present the delay of every time-tag compared to the first time-tag after the start of the measurement. We see that the FPGA clock is set to 0 s every 250 ms. In our lifetime measurements, we always compute the time delay of a photon with respect to a trigger signal. We neglect negative delays. Therefore, this resetting of the FPGA does not affect the lifetime measurement.

We compute the time delay between consecutive time-tags. We make a histogram of these delays (see Fig. D.2(a)). Since the time-tags are saved in ps, we used a binning length of 1 ps for the histogram. We expect a delay of 100 ns. We fit the histogram with a Gaussian function. The free fit parameters were a constant offset, the amplitude, the expected value, and the width of the Gaussian. The expected value differs by about 5.88 ps from 100 ns corresponding to a relative error of about $\Delta t_{\text{rel}} = 6 \times 10^{-5}$. Hence,

¹Stanford Research Systems, FS725

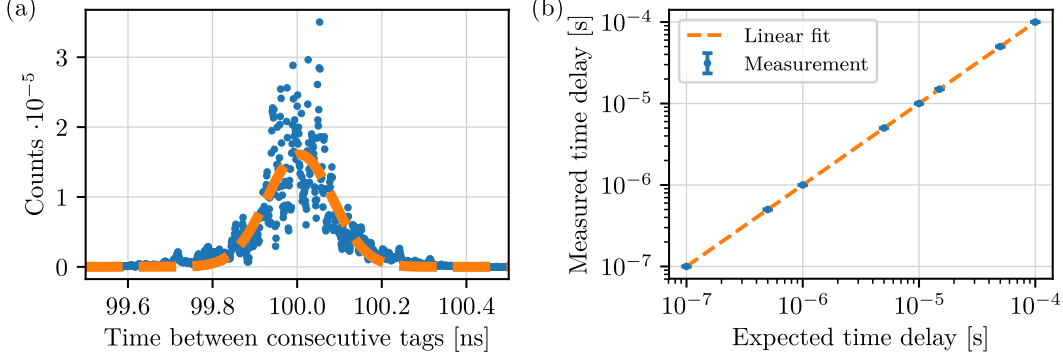


FIGURE D.2: Measurement of the FPGA accuracy. (a) A histogram of the delay of consecutive time-tags. We expect a delay of 100 ns. From a fit with a Gaussian function, we find a deviation of about 5.88 ps from the expected value. (b) Delay between time-tags which are n time-tags apart. We expect a delay of $n \cdot 100$ ns. We show the average and the standard deviation of the computed delays.

the real time t is obtained from the clock time t_c with $t = (1 + \Delta t_{\text{rel}}) \cdot t_c$. We fit our lifetime measurement with t_c , meaning we fit $I_0 \exp(-t_c/\tau_D) + c$. The corrected lifetime is $\tau_{D,\text{corr}} = (1 + \Delta t_{\text{rel}}) \cdot \tau_D$. For our measured lifetime values, this yields an error of about 80 ps, which is negligible in our error budget. The FWHM of the measured delay distribution is about 78.0(1) ps, which is also negligible in our final error budget.

We want to investigate the FPGA clock on a longer time scale than 100 ns. We compute the delay Δt of a time-tag with respect to a time-tag which was recorded n time-tags before. We expect a delay of $\Delta t = n \cdot 100$ ns. In Fig. D.2(b), we present the average delay $\overline{\Delta t}$ and the standard deviation of the delays for $n = 1, 5, 10, 50, 100, 150, 500, 1000$ depending on the expected value. As predicted, we find a linear behavior. Hence, we fit the average delays with a linear function $k \cdot \overline{\Delta t} + d$ where k and d are our free fit parameters. We find $k \approx 1.000033$. This is close to $\Delta t_{\text{rel}} = 6 \times 10^{-5}$ which we found above. Furthermore, we find $d \approx 5 \times 10^{-16}$ s which is negligible. Hence, we accept the estimate above and neglect the FPGA contribution in our final error budget.

D.3 SPCM Dead Time

Our SPCM is specified to have a dead time of $t_{\text{dead}} = 22$ ns. Therefore, if a photon arrives on the SPCM less than 22 ns after the detection of another photon, it will not be detected. This alters the distribution of the arrival times when the photon flux is large. We can calculate the actual photon rate f_a with

$$f_a = \frac{f_m \cdot x - f_{\text{dark}}}{\epsilon}, \quad (\text{D.4})$$

where f_m is the measured photon count rate, $f_{\text{dark}} = 100$ Hz is the dark count rate, $\epsilon \approx 50\%$ is the photon detection efficiency, and x is a correction factor. At low count rates, we can calculate the correction factor as

$$x = \frac{1}{1 - t_{\text{dead}} \cdot f_m}. \quad (\text{D.5})$$

In our measurements, we detect, on average, 0.1 photons per 50 μ s cycle, corresponding to an photon count rate of $f_m = 2$ kHz. Hence $x \approx 1$, and we can neglect the dead time of the SPCM.

D.4 Other Systematics

There are many systematic effects that could alter the detected lifetime. For example, multiple decay paths from the excited state to the ground state could interfere. Then, the decay signal is superimposed by a modulation with a frequency given by the energy separation of the two coherently excited levels [277]. The phenomenon of this modulation is commonly known as quantum beats [278]. In our system, only quantum beats arising as a result of an energy difference between different Zeeman substates play a role. To investigate that, we performed measurements with various magnetic fields up to 25 G, using a coil that encloses the cesium cell. We observed no quantum beats. Other quantum beats, e.g., originating from different hyperfine levels, are expected to have oscillation periods much shorter than the lifetime of the $5D_{5/2}$ state.

Inelastic collisions of excited atoms with the walls of the vapor cell can deexcite the atoms [236]. In our setup, we paid attention to send the laser beam through the center of the vapor cell. Then, considering the diameter of our vapor cell, wall collisions

Appendix D. Other Systematic Errors of the Lifetime Measurement

should be negligible [236, 237]. Also, black-body radiation [236], afterpulses [236], and pulse pile-up correction [8] should not influence the outcome of our analysis.

Appendix E

Open Access to the Experimental Data

The way how science is performed is always changing. Nowadays, not only the total amount of data worldwide is growing exponentially [279] but also the science community is growing at a great pace. This raises new challenges and opportunities. For example, it opens the possibility for worldwide collaborations. However, new science institutions, especially in low-income countries, are often without the funding required to participate in the scientific exchange because, e.g., many papers are published behind expensive paywalls of peer-reviewed journals [280, 281]. Open access publications and open access data can resolve many of these issues and could lead to faster circulations of scientific ideas and, that way, also to more scientific output. Regarding this, especially the COVID-19 crisis has shown how important open scientific exchange can be. For instance, open access to new results and the latest data let to a fast knowledge about the properties of the virus.

Here, we want to discuss our contributions to open data and open access. We demonstrate an exemplary workflow that could serve as an assistant for other publications. We start with an overview of how one can make data findable, accessible, interoperable, and reusable (FAIR). Then, we discuss possible repositories to publish scientific data which supports a publication and mention the protection of data by, e.g., licenses. Finally, we present our implementation of open access to our publication as well as the supporting data and description. In this section, however, data corresponds to the measured data, and metadata refers to the data about the data. It is also common to talk about paradata describing data "around" the data.

E.1 The FAIR-Principles

We discuss here the FAIR principles. It describes a set of guiding principles to make data findable, accessible, interoperable, and reusable. FAIR data is, in this context, data that meets certain principles. The FAIR Data Principles were developed in 2016 to improve the infrastructure supporting the reuse of scholarly data [282]. It is widely accepted as a guideline for people who want to enhance the reusability of their data. The latest developments on FAIR can be found at GO-FAIR¹. The principles apply to infrastructures and services as well as to data management.

We discuss some important aspects of the FAIR principles, which might be obvious, but often they are neglected. In order to be reusable, data has to be findable. Both data and metadata should be easy to find for humans as well as computers. Machine-readable metadata is essential for automatic discovery. Once the user finds the data, it should be obvious how to access it. This can include authentications and authorizations. Data often has to be integrated with other data or integrated into workflows for analysis, storage, and processing. Therefore, it should be interoperable. In order to make data reusable, data and metadata should be well-described.

E.2 Data Repositories

A data repository is a collection of data sets. Usually, it is a place that stores data and makes it available to use. There are several operating repositories that have advantages and disadvantages. A reliable repository should fulfill some requirements which may change from case to case. OpenAIRE² and re3data³ can be used to find a suitable repository. We now discuss our requirements to publish experimental data of measurements similar to the present lifetime measurement.

A repository should provide a permanent digital identifier (DOI) to a data set which makes it easier to find. Furthermore, it is possible to use this DOI in publications. A repository is preferable funded by public funding. An example could be a nation or the European Union. Repositories funded by a company depend on the plans of the company, which may, e.g., decide to restrict access to the data. Preferably, the

¹“FAIR Principles”, (2019), URL <https://www.go-fair.org/fair-principles/>, last accessed on 2020-05-02

²“OpenAIRE”, (2020), URL <https://www.openaire.eu/>, last accessed on 2020-05-02

³“re3data.org - Registry of Research Data Repositories”, (2020), URL <https://doi.org/10.17616/R3D>, last accessed on 2020-05-02

possibility to choose the accessibility of the data should be provided, e.g., if the data set is freely accessible, if there is an embargo, or if the access is controlled by, e.g., the owner. Furthermore, a good backup strategy is essential. This includes that the data is stored in several places. The repository should have the possibility to provide the data in our chosen format, which is usually an open and standard format. Some repositories provide peer-reviewing, but this usually entails costs. It should be considered if a repository helps to track how the data has been used. Finally, guidance on how to cite the data should be provided.

Several data repositories are in operation. There are many data-type-specific repositories. However, when there is no specialized data repository, a general-purpose repository is a common choice. We take Zenodo⁴ as an example for such a repository, but similar repositories are often recommended, as for example Dryad⁵, Figshare⁶, or the Harvard Database⁷. Zenodo is a service developed under the European OpenAIRE program and operated by CERN. Hence, the European Commission and CERN itself provide the main funding. It is a dependable open home for science that enables researchers to share and preserve any research outputs. However, there is a size limit of 50 GB per dataset, which can be extended on a reasonable request. Zenodo provides a DOI to datasets and stores the data in the EU. Every file that is uploaded to Zenodo has two replicas located on different disk servers. Additionally, it provides citation guidelines and options to restrict access to datasets. The outlined reasons make Zenodo a popular repository within the science community.

E.3 Data Access and Licences

We discuss here how to protect data and how to prevent misuse of the data. In this context, we take a look at data access arrangements and licenses.

Open data refers to data that can be accessed by any user without registration. However, there might be a reason to restrict access by, e.g., making registration compulsory. Many services provide the possibility that the authors can decide who has access. A user has to contact the author who can provide him the access via, e.g., a link or a special password. Often it is possible to set an embargo on the data. This

⁴“Zenodo”, (2020), URL <https://zenodo.org/>, last accessed on 2020-05-02

⁵“Dryad”, (2020), URL <https://datadryad.org/>, last accessed on 2020-05-02

⁶“figshare”, (2020), URL <https://figshare.com/>, last accessed on 2020-05-02

⁷“Harvard Dataverse”, (2020), URL <https://dataverse.harvard.edu/>, last accessed on 2020-05-02

might be useful when the data should be published together with, e.g., a paper in a journal. An embargo typically has a specific date where it ends.

Data always has to be published with a license. This is not only to prevent misuse and declare ownership but also to inform the user what can be done with the data. In this context, a license is a permission for someone else to do something. Licenses define conditions of access and conditions of (re-)use. The most common licenses are the “Creative Commons Licenses”⁸. They provide different kinds of licenses that declare how the data can be used. For instance, the license “CC BY” lets others do almost everything with the data as long as they credit the owner for the original creation. The license “CC BY-NC” additionally declares that it is only allowed to use the data non-commercially. More specifications are available.

E.4 Our Implementation

We took several measures to improve the traceability of the presented lifetime measurements and the corresponding analysis. First, we took actions that our preprint [283], as well as our manuscript [225] on the lifetime measurement of the $5D_{5/2}$ state, is made available barrier-free and open access. We use Zenodo to provide access to our experimental data because it fulfills all of our requirements (see section E.2). In the manuscript, we included a DOI and a link to our repository on Zenodo [261]. This repository contains raw experimental data used for our study. To store the raw time-tags of one measurement in a file, we use the common DAT file format. Since the files of the raw measurement data are large, we also generated histograms of the time-tags and provided them in data files (.dat) as well as in NumPy compressed array format files (.npz). The repository also includes additional information on the measurements. For every measurement, a JavaScript Object Notation file (.json) contains the following information: temperature of the cell, number of detected photons, photons per cycle, and the total measurement duration. Finally, we provided examples of source codes that demonstrate how our data can be processed with Python.

In conclusion, we are certain that the outlined arrangements make our measured experimental data findable, accessible, interoperable, and reusable. We hope that we could improve the traceability of the presented measurements and analysis. Our workflow might be beneficial for similar studies of fundamental values as, e.g., the lifetimes

⁸“Creative Commons”, (2020), URL <https://creativecommons.org/>, last accessed on 2020-05-02

E.4. Our Implementation

of excited atomic states. These values are often long-lasting and reused for, e.g., theoretical calculations and estimations.

Bibliography

- [1] J. Dalton, *A new system of chemical Philosophy* (1808)
- [2] J. J. Thomson, “XXIV. On the structure of the atom: an investigation of the stability and periods of oscillation of a number of corpuscles arranged at equal intervals around the circumference of a circle; with application of the results to the theory of atomic structure”, *Lond. Edinb. Dublin philos. mag. j. sci.*, **7**, 237 (1904), URL <https://doi.org/10.1080/14786440409463107>
- [3] E. Rutherford, “LXXIX. The scattering of α and β particles by matter and the structure of the atom”, *Lond. Edinb. Dublin philos. mag. j. sci.*, **21**, 669 (1911), URL <https://doi.org/10.1080/14786440508637080>
- [4] N. Bohr, “I. On the constitution of atoms and molecules”, *Lond. Edinb. Dublin philos. mag. j. sci.*, **26**, 1 (1913), URL <https://doi.org/10.1080/14786441308634955>
- [5] L. De Broglie, “Recherches sur la théorie des Quanta”, Ph.D. thesis, Migration-université en cours d’affectation (1924), URL <https://tel.archives-ouvertes.fr/tel-00006807>
- [6] E. Schrödinger, “Quantisierung als eigenwertproblem”, *Ann. Phys.*, **385**, 437 (1926), URL <https://doi.org/10.1002/andp.19263861802>
- [7] C. J. Foot, *Atomic physics*, volume 7, Oxford University Press (2005), URL <https://global.oup.com/academic/product/atomic-physics-9780198506966>
- [8] D. Sheng, A. Pérez Galván and L. A. Orozco, “Lifetime measurements of the 5d states of rubidium”, *Phys. Rev. A*, **78**, 062506 (2008), URL <https://link.aps.org/doi/10.1103/PhysRevA.78.062506>
- [9] E. L. Raab, M. Prentiss, A. Cable, S. Chu and D. E. Pritchard, “Trapping of Neutral Sodium Atoms with Radiation Pressure”, *Phys. Rev. Lett.*, **59**, 2631 (1987), URL <https://link.aps.org/doi/10.1103/PhysRevLett.59.2631>
- [10] I. B. Mekhov and H. Ritsch, “Quantum optics with ultracold quantum gases: towards the full quantum regime of the light–matter interaction”, *J. Phys. B*, **45**, 102001 (2012), URL <http://dx.doi.org/10.1088/0953-4075/45/10/102001>
- [11] M. Saffman, T. G. Walker and K. Mølmer, “Quantum information with Rydberg atoms”, *Rev. Mod. Phys.*, **82**, 2313 (2010), URL <https://doi.org/10.1103/RevModPhys.82.2313>
- [12] I. S. Madjarov, J. P. Covey, A. L. Shaw, J. Choi, A. Kale, A. Cooper, H. Pichler, V. Schkolnik, J. R. Williams and M. Endres, “High-fidelity entanglement and detection of alkaline-earth Rydberg atoms”, *Nat. Phys.*, **16**, 857 (2020), URL <https://doi.org/10.1038/s41567-020-0903-z>

-
- [13] S. Ebadi, T. T. Wang, H. Levine, A. Keesling, G. Semeghini, A. Omran, D. Bluvstein, R. Samajdar, H. Pichler, W. W. Ho, S. Choi, S. Sachdev, M. Greiner, V. Vuletić and M. D. Lukin, “Quantum phases of matter on a 256-atom programmable quantum simulator”, *Nature*, **595**, 227–232 (2021), URL [10.1038/s41586-021-03582-4](https://doi.org/10.1038/s41586-021-03582-4)
- [14] P. Scholl, M. Schuler, H. J. Williams, A. A. Eberharter, D. Barredo, K.-N. Schymik, V. Lienhard, L.-P. Henry, T. C. Lang, T. Lahaye, A. M. Läuchli and A. Browaeys, “Quantum simulation of 2D antiferromagnets with hundreds of Rydberg atoms”, *Nature*, **595**, 233 (2021), URL <https://doi.org/10.1038/s41586-021-03585-1>
- [15] E. Vetsch, D. Reitz, G. Sagué, R. Schmidt, S. T. Dawkins and A. Rauschenbeutel, “Optical Interface Created by Laser-Cooled Atoms Trapped in the Evanescent Field Surrounding an Optical Nanofiber”, *Phys. Rev. Lett.*, **104**, 203603 (2010), URL <https://link.aps.org/doi/10.1103/PhysRevLett.104.203603>
- [16] J. D. Thompson, T. Tiecke, N. P. de Leon, J. Feist, A. Akimov, M. Gullans, A. S. Zibrov, V. Vuletić and M. D. Lukin, “Coupling a single trapped atom to a nanoscale optical cavity”, *Science*, **340**, 1202 (2013), URL <https://doi.org/10.1126/science.1237125>
- [17] T. Tiecke, J. D. Thompson, N. P. de Leon, L. Liu, V. Vuletić and M. D. Lukin, “Nanophotonic quantum phase switch with a single atom”, *Nature*, **508**, 241 (2014), URL <https://doi.org/10.1038/nature13188>
- [18] A. Goban, C.-L. Hung, J. D. Hood, S.-P. Yu, J. A. Muniz, O. Painter and H. J. Kimble, “Superradiance for Atoms Trapped along a Photonic Crystal Waveguide”, *Phys. Rev. Lett.*, **115**, 063601 (2015), URL <https://link.aps.org/doi/10.1103/PhysRevLett.115.063601>
- [19] S. Kato and T. Aoki, “Strong Coupling between a Trapped Single Atom and an All-Fiber Cavity”, *Phys. Rev. Lett.*, **115**, 093603 (2015), URL <https://link.aps.org/doi/10.1103/PhysRevLett.115.093603>
- [20] A. Reiserer and G. Rempe, “Cavity-based quantum networks with single atoms and optical photons”, *Rev. Mod. Phys.*, **87**, 1379 (2015), URL <https://link.aps.org/doi/10.1103/RevModPhys.87.1379>
- [21] T. Nieddu, V. Gokhroo and S. N. Chormaic, “Optical nanofibres and neutral atoms”, *J. Opt.*, **18**, 053001 (2016), URL <http://dx.doi.org/10.1088/2040-8978/18/5/053001>
- [22] K. P. Nayak, J. Wang and J. Keloth, “Real-Time Observation of Single Atoms Trapped and Interfaced to a Nanofiber Cavity”, *Phys. Rev. Lett.*, **123**, 213602 (2019), URL <https://link.aps.org/doi/10.1103/PhysRevLett.123.213602>
- [23] L. Novotny and B. Hecht, *Principles of nano-optics*, Cambridge university press (2012), URL <https://doi.org/10.1017/CB09780511813535>
- [24] K. Y. Bliokh and F. Nori, “Transverse and longitudinal angular momenta of light”, *Phys. Rep.*, **592**, 1 (2015), URL <https://doi.org/10.1016/j.physrep.2015.06.003>
- [25] K. Y. Bliokh, F. J. Rodríguez-Fortuño, F. Nori and A. V. Zayats, “Spin-orbit interactions of light”, *Nat. Photon.*, **9**, 796 (2015), URL <https://doi.org/10.1038/nphoton.2015.201>
- [26] A. Aiello, P. Banzer, M. Neugebauer and G. Leuchs, “From transverse angular momentum to photonic wheels”, *Nat. Photon.*, **9**, 789 (2015), URL <https://doi.org/10.1038/nphoton.2015.203>

BIBLIOGRAPHY

- [27] T. Van Mechelen and Z. Jacob, “Universal spin-momentum locking of evanescent waves”, *Optica*, **3**, 118 (2016), URL <https://doi.org/10.1364/OPTICA.3.000118>
- [28] T. Kawalec, L. Józefowski, J. Fiutowski, M. Kasprówicz and T. Dohnalik, “Spectroscopic measurements of the evanescent wave polarization state”, *Opt. Commun.*, **274**, 341 (2007), URL <https://doi.org/10.1016/j.optcom.2007.02.042>
- [29] K. Y. Bliokh and A. Aiello, “Goos–Hänchen and Imbert–Fedorov beam shifts: an overview”, *J. Opt.*, **15**, 014001 (2013), URL <http://dx.doi.org/10.1088/2040-8978/15/1/014001>
- [30] X. Yin, Z. Ye, J. Rho, Y. Wang and X. Zhang, “Photonic spin Hall effect at metasurfaces”, *Science*, **339**, 1405 (2013), URL <https://doi.org/10.1126/science.1231758>
- [31] A. Aiello, N. Lindlein, C. Marquardt and G. Leuchs, “Transverse Angular Momentum and Geometric Spin Hall Effect of Light”, *Phys. Rev. Lett.*, **103**, 100401 (2009), URL <https://link.aps.org/doi/10.1103/PhysRevLett.103.100401>
- [32] K. Y. Bliokh, M. A. Alonso, E. A. Ostrovskaya and A. Aiello, “Angular momenta and spin-orbit interaction of nonparaxial light in free space”, *Phys. Rev. A*, **82**, 063825 (2010), URL <https://link.aps.org/doi/10.1103/PhysRevA.82.063825>
- [33] M. Neugebauer, P. Banzer, T. Bauer, S. Orlov, N. Lindlein, A. Aiello and G. Leuchs, “Geometric spin Hall effect of light in tightly focused polarization-tailored light beams”, *Phys. Rev. A*, **89**, 013840 (2014), URL <https://link.aps.org/doi/10.1103/PhysRevA.89.013840>
- [34] I. Luxmoore, N. A. Wasley, A. J. Ramsay, A. Thijssen, R. Oulton, M. Hugues, A. Fox and M. Skolnick, “Optical control of the emission direction of a quantum dot”, *Applied Physics Letters*, **103**, 241102 (2013), URL <http://dx.doi.org/10.1063/1.4845975>
- [35] F. J. Rodríguez-Fortuño, G. Marino, P. Ginzburg, D. O’Connor, A. Martínez, G. A. Wurtz and A. V. Zayats, “Near-field interference for the unidirectional excitation of electromagnetic guided modes”, *Science*, **340**, 328 (2013), URL <https://doi.org/10.1126/science.1233739>
- [36] J. Lin, J. B. Mueller, Q. Wang, G. Yuan, N. Antoniou, X.-C. Yuan and F. Capasso, “Polarization-controlled tunable directional coupling of surface plasmon polaritons”, *Science*, **340**, 331 (2013), URL <https://doi.org/10.1126/science.1233746>
- [37] J. Petersen, J. Volz and A. Rauschenbeutel, “Chiral nanophotonic waveguide interface based on spin-orbit interaction of light”, *Science*, **346**, 67 (2014), URL <https://doi.org/10.1126/science.1257671>
- [38] R. Mitsch, C. Sayrin, B. Albrecht, P. Schneeweiss and A. Rauschenbeutel, “Exploiting the local polarization of strongly confined light for sub-micrometer-resolution internal state preparation and manipulation of cold atoms”, *Phys. Rev. A*, **89**, 063829 (2014), URL <https://link.aps.org/doi/10.1103/PhysRevA.89.063829>
- [39] I. Shomroni, S. Rosenblum, Y. Lovsky, O. Bechler, G. Guendelman and B. Dayan, “All-optical routing of single photons by a one-atom switch controlled by a single photon”, *Science*, **345**, 903 (2014), URL <https://doi.org/10.1126/science.1254699>
- [40] P. V. Kapitanova, P. Ginzburg, F. J. Rodríguez-Fortuño, D. S. Filonov, P. M. Voroshilov, P. A. Belov, A. N. Poddubny, Y. S. Kivshar, G. A. Wurtz and A. V. Zayats, “Photonic spin Hall effect in hyperbolic metamaterials for polarization-controlled routing of subwavelength modes”, *Nat. Commun.*, **5**, 1 (2014), URL <https://doi.org/10.1038/ncomms4226>

-
- [41] B. Le Feber, N. Rotenberg and L. Kuipers, “Nanophotonic control of circular dipole emission”, *Nat. Commun.*, **6**, 1 (2015), URL <https://doi.org/10.1038/ncomms7695>
- [42] I. Söllner, S. Mahmoodian, S. L. Hansen, L. Midolo, A. Javadi, G. Kiršanskė, T. Pregnolato, H. El-Ella, E. H. Lee, J. D. Song *et al.*, “Deterministic photon–emitter coupling in chiral photonic circuits”, *Nat. Nanotechnol.*, **10**, 775 (2015), URL <https://doi.org/10.1038/nnano.2015.159>
- [43] B. Lang, D. M. Beggs and R. Oulton, “Time-reversal constraint limits unidirectional photon emission in slow-light photonic crystals”, *Philos. Trans. R. Soc. A*, **374**, 20150263 (2016), URL <https://doi.org/10.1098/rsta.2015.0263>
- [44] R. Coles, D. Price, J. Dixon, B. Royall, E. Clarke, P. Kok, M. Skolnick, A. Fox and M. Makhonin, “Chirality of nanophotonic waveguide with embedded quantum emitter for unidirectional spin transfer”, *Nat. Commun.*, **7**, 1 (2016), URL <https://doi.org/10.1038/ncomms11183>
- [45] T. Chervy, S. Azzini, E. Lorchat, S. Wang, Y. Gorodetski, J. A. Hutchison, S. Berciaud, T. W. Ebbesen and C. Genet, “Room temperature chiral coupling of valley excitons with spin-momentum locked surface plasmons”, *ACS Photonics*, **5**, 1281 (2018), URL <https://doi.org/10.1021/acsp Photonics.7b01032>
- [46] S.-H. Gong, F. Alpegiani, B. Sciacca, E. C. Garnett and L. Kuipers, “Nanoscale chiral valley-photon interface through optical spin-orbit coupling”, *Science*, **359**, 443 (2018), URL <https://doi.org/10.1126/science.aan8010>
- [47] L. Tang, J. Tang, W. Zhang, G. Lu, H. Zhang, Y. Zhang, K. Xia and M. Xiao, “On-chip chiral single-photon interface: Isolation and unidirectional emission”, *Phys. Rev. A*, **99**, 043833 (2019), URL <https://link.aps.org/doi/10.1103/PhysRevA.99.043833>
- [48] M. Rothe, Y. Zhao, J. Müller, G. Kewes, C. T. Koch, Y. Lu and O. Benson, “Self-Assembly of Plasmonic Nanoantenna–Waveguide Structures for Subdiffractive Chiral Sensing”, *ACS nano*, **15**, 351 (2020), URL <https://doi.org/10.1021/acsnano.0c05240>
- [49] F. Lei, G. Tkachenko, X. Jiang, J. M. Ward, L. Yang and S. N. Chormaic, “Enhanced directional coupling of light with a whispering gallery microcavity”, *ACS Photonics*, **7**, 361 (2020), URL <https://doi.org/10.1021/acsp Photonics.9b01611>
- [50] R. Shreiner, K. Hao, A. Butcher and A. A. High, “Electrically controllable chirality in a nanophotonic interface with a two-dimensional semiconductor”, *Nat. Photon.*, 1–7 (2022), URL <https://doi.org/10.1038/s41566-022-00971-7>
- [51] B. Lang, D. P. S. McCutcheon, E. Harbord, A. B. Young and R. Oulton, “Perfect Chirality with Imperfect Polarization”, *Phys. Rev. Lett.*, **128**, 073602 (2022), URL <https://link.aps.org/doi/10.1103/PhysRevLett.128.073602>
- [52] Y. Cheng, K. A. Oyesina, B. Xue, D. Lei, A. M. H. Wong and S. Wang, “Directional Dipole Dice: Circular-Huygens-Janus Dipole in an Anisotropic Chiral Particle”, (2022), URL <https://doi.org/10.48550/arxiv.2208.04151>
- [53] J. Olthaus, M. Sohr, S. Wong, S. S. Oh and D. E. Reiter, “Modelling spatio-temporal dynamics of chiral coupling of quantum emitters to light fields in nanophotonic structures”, (2022), URL <https://doi.org/10.48550/arxiv.2208.00879>

BIBLIOGRAPHY

- [54] P. Lodahl, S. Mahmoodian, S. Stobbe, A. Rauschenbeutel, P. Schneeweiss, J. Volz, H. Pichler and P. Zoller, “Chiral quantum optics”, *Nature*, **541**, 473 (2017), URL <https://doi.org/10.1038/nature21037>
- [55] B. Lang, R. Oulton and D. M. Beggs, “Optimised photonic crystal waveguide for chiral light–matter interactions”, *J. Opt.*, **19**, 045001 (2017), URL <https://doi.org/10.1088/2040-8986/aa5f5f>
- [56] Y.-F. Xiao, C.-L. Zou, Q. Gong and L. Yang, *Ultra-high-Q Optical Microcavities*, World Scientific (2020), URL <https://doi.org/10.1142/8964>
- [57] D. Hallett, A. P. Foster, D. Whittaker, M. S. Skolnick and L. R. Wilson, “Engineering Chiral Light–Matter Interactions in a Waveguide-Coupled Nanocavity”, *ACS Photonics* (2022), URL <https://doi.org/10.1021/acsp Photonics.1c01806>
- [58] N. Nefedkin, M. Cotrufo, A. Krasnok and A. Alù, “Dark-State Induced Quantum Nonreciprocity”, *Adv. Quantum Technol.*, 2100112 (2022), URL <https://doi.org/10.1002/qute.202100112>
- [59] V. S. Asadchy, M. S. Mirmoosa, A. Díaz-Rubio, S. Fan and S. A. Tretyakov, “Tutorial on Electromagnetic Nonreciprocity and its Origins”, *Proc. IEEE*, **108**, 1684 (2020), URL <https://doi.org/10.1109/JPROC.2020.3012381>
- [60] G. G. Stokes, *On the perfect blackness of the central spot in Newton’s rings, and on the verification of Fresnel’s formulae for the intensities of reflected and refracted rays*, volume 4 (1849), URL http://resolver.sub.uni-goettingen.de/purl?PPN600493962_0004
- [61] H. v. Helmholtz, “Handbuch der Physiologischen Optik”, *Optik Leipzig: Leopold Voss*, **1** (1856)
- [62] H. A. Lorentz, “The theorem of Poynting concerning the energy in the electromagnetic field and two general propositions concerning the propagation of light”, *Amsterdammer Akademie der Wetenschappen*, **4**, 176 (1896)
- [63] B. E. Saleh and M. C. Teich, *Fundamentals of photonics*, JWS (1991), URL <https://doi.org/10.1002/0471213748>
- [64] R. J. Potton, “Reciprocity in optics”, *Rep. Prog. Phys.*, **67**, 717 (2004), URL <https://doi.org/10.1088/0034-4885/67/5/R03>
- [65] D. Jalas, A. Petrov, M. Eich, W. Freude, S. Fan, Z. Yu, R. Baets, M. Popović, A. Melloni, J. D. Joannopoulos, M. Vanwolleghem, C. R. Doerr and H. Renner, “What is—and what is not—an optical isolator”, *Nat. Photon.*, **7**, 579 (2013), URL <https://doi.org/10.1038/nphoton.2013.185>
- [66] C. Caloz, A. Alù, S. Tretyakov, D. Sounas, K. Achouri and Z.-L. Deck-Léger, “Electromagnetic Nonreciprocity”, *Phys. Rev. Applied*, **10**, 047001 (2018), URL <https://link.aps.org/doi/10.1103/PhysRevApplied.10.047001>
- [67] C. Sayrin, C. Junge, R. Mitsch, B. Albrecht, D. O’Shea, P. Schneeweiss, J. Volz and A. Rauschenbeutel, “Nanophotonic Optical Isolator Controlled by the Internal State of Cold Atoms”, *Phys. Rev. X*, **5**, 041036 (2015), URL <https://link.aps.org/doi/10.1103/PhysRevX.5.041036>
- [68] M. Scheucher, A. Hilico, E. Will, J. Volz and A. Rauschenbeutel, “Quantum optical circulator controlled by a single chirally coupled atom”, *Science*, **354**, 1577 (2016), URL <https://doi.org/10.1126/science.aaj2118>

-
- [69] X.-X. Hu, Z.-B. Wang, P. Zhang, G.-J. Chen, Y.-L. Zhang, G. Li, X.-B. Zou, T. Zhang, H. X. Tang, C.-H. Dong, G.-C. Guo and C.-L. Zou, “Noiseless photonic non-reciprocity via optically-induced magnetization”, *Nat. Commun.*, **12**, 1 (2021), URL <https://doi.org/10.1038/s41467-021-22597-z>
- [70] F. Song, Z. Wang, E. Li, B. Yu and Z. Huang, “Nonreciprocity with Structured Light Using Optical Pumping in Hot Atoms”, *Phys. Rev. Applied*, **18**, 024027 (2022), URL <https://doi.org/10.1103/PhysRevApplied.18.024027>
- [71] P. Solano, J. A. Grover, J. E. Hoffman, S. Ravets, F. K. Fatemi, L. A. Orozco and S. L. Rolston, “Optical nanofibers: a new platform for quantum optics”, *Adv. At. Mol. Opt. Phys.*, **66**, 439 (2017), URL <https://doi.org/10.1016/bs.aamop.2017.02.003>
- [72] K. P. Nayak, M. Sadgrove, R. Yalla, F. Le Kien and K. Hakuta, “Nanofiber quantum photonics”, *J. Opt.*, **20**, 073001 (2018), URL <https://doi.org/10.1088/2040-8986/aac35e>
- [73] F. Le Kien, V. I. Balykin and K. Hakuta, “Atom trap and waveguide using a two-color evanescent light field around a subwavelength-diameter optical fiber”, *Phys. Rev. A*, **70**, 063403 (2004), URL <https://link.aps.org/doi/10.1103/PhysRevA.70.063403>
- [74] A. Goban, K. S. Choi, D. J. Alton, D. Ding, C. Lacroûte, M. Pototschnig, T. Thiele, N. P. Stern and H. J. Kimble, “Demonstration of a State-Insensitive, Compensated Nanofiber Trap”, *Phys. Rev. Lett.*, **109**, 033603 (2012), URL <https://link.aps.org/doi/10.1103/PhysRevLett.109.033603>
- [75] J.-B. Béguin, E. M. Bookjans, S. L. Christensen, H. L. Sørensen, J. H. Müller, E. S. Polzik and J. Appel, “Generation and Detection of a Sub-Poissonian Atom Number Distribution in a One-Dimensional Optical Lattice”, *Phys. Rev. Lett.*, **113**, 263603 (2014), URL <https://link.aps.org/doi/10.1103/PhysRevLett.113.263603>
- [76] J. Lee, J. Grover, J. Hoffman, L. Orozco and S. Rolston, “Inhomogeneous broadening of optical transitions of ^{87}Rb atoms in an optical nanofiber trap”, *J. Phys. B: At. Mol. Opt. Phys.*, **48**, 165004 (2015), URL <http://dx.doi.org/10.1088/0953-4075/48/16/165004>
- [77] D. Su, R. Liu, Z. Ji, X. Qi, Z. Song, Y. Zhao, L. Xiao and S. Jia, “Observation of ladder-type electromagnetically induced transparency with atomic optical lattices near a nanofiber”, *New J. Phys.*, **21**, 043053 (2019), URL <https://doi.org/10.1088/1367-2630/ab172e>
- [78] R. K. Gupta, J. L. Everett, A. D. Tranter, R. Henke, V. Gokhroo, P. K. Lam and S. N. Chormaic, “Machine learner optimization of optical nanofiber-based dipole traps for cold ^{87}Rb atoms”, *arXiv preprint arXiv:2110.03931* (2021), URL <https://doi.org/10.48550/arXiv.2110.03931>
- [79] R. Mitsch, C. Sayrin, B. Albrecht, P. Schneeweiss and A. Rauschenbeutel, “Quantum state-controlled directional spontaneous emission of photons into a nanophotonic waveguide”, *Nat. Commun.*, **5**, 1 (2014), URL <https://doi.org/10.1038/ncomms6713>
- [80] A. Dareau, Y. Meng, P. Schneeweiss and A. Rauschenbeutel, “Observation of Ultrastrong Spin-Motion Coupling for Cold Atoms in Optical Microtraps”, *Phys. Rev. Lett.*, **121**, 253603 (2018), URL <https://link.aps.org/doi/10.1103/PhysRevLett.121.253603>
- [81] C. Sayrin, C. Clausen, B. Albrecht, P. Schneeweiss and A. Rauschenbeutel, “Storage of fiber-guided light in a nanofiber-trapped ensemble of cold atoms”, *Optica*, **2**, 353 (2015), URL <https://doi.org/10.1364/OPTICA.2.000353>

BIBLIOGRAPHY

- [82] B. Gouraud, D. Maxein, A. Nicolas, O. Morin and J. Laurat, “Demonstration of a Memory for Tightly Guided Light in an Optical Nanofiber”, *Phys. Rev. Lett.*, **114**, 180503 (2015), URL <https://link.aps.org/doi/10.1103/PhysRevLett.114.180503>
- [83] S. Pucher, C. Liedl, S. Jin, A. Rauschenbeutel and P. Schneeweiss, “Atomic spin-controlled non-reciprocal Raman amplification of fibre-guided light”, *Nat. Photon.* (2022), URL <https://doi.org/10.1038/s41566-022-00987-z>
- [84] C. Liedl, S. Pucher, F. Tebbenjohanns, P. Schneeweiss and A. Rauschenbeutel, “Collective excitation and decay of waveguide-coupled atoms: from timed Dicke states to inverted ensembles”, (2022), URL <https://doi.org/10.48550/arxiv.2204.04106>
- [85] H. L. Sørensen, J.-B. Béguin, K. W. Kluge, I. Iakoupov, A. S. Sørensen, J. H. Müller, E. S. Polzik and J. Appel, “Coherent Backscattering of Light Off One-Dimensional Atomic Strings”, *Phys. Rev. Lett.*, **117**, 133604 (2016), URL <https://link.aps.org/doi/10.1103/PhysRevLett.117.133604>
- [86] N. V. Corzo, B. Gouraud, A. Chandra, A. Goban, A. S. Sheremet, D. V. Kupriyanov and J. Laurat, “Large Bragg Reflection from One-Dimensional Chains of Trapped Atoms Near a Nanoscale Waveguide”, *Phys. Rev. Lett.*, **117**, 133603 (2016), URL <https://link.aps.org/doi/10.1103/PhysRevLett.117.133603>
- [87] N. V. Corzo, J. Raskop, A. Chandra, A. S. Sheremet, B. Gouraud and J. Laurat, “Waveguide-coupled single collective excitation of atomic arrays”, *Nature*, **566**, 359 (2019), URL <https://doi.org/10.1038/s41586-019-0902-3>
- [88] A. S. Prasad, J. Hinney, S. Mahmoodian, K. Hammerer, S. Rind, P. Schneeweiss, A. S. Sørensen, J. Volz and A. Rauschenbeutel, “Correlating photons using the collective nonlinear response of atoms weakly coupled to an optical mode”, *Nat. Photon.*, **14**, 719 (2020), URL <https://doi.org/10.1038/s41566-020-0692-z>
- [89] J. Hinney, A. S. Prasad, S. Mahmoodian, K. Hammerer, A. Rauschenbeutel, P. Schneeweiss, J. Volz and M. Schemmer, “Unraveling Two-Photon Entanglement via the Squeezing Spectrum of Light Traveling through Nanofiber-Coupled Atoms”, *Phys. Rev. Lett.*, **127**, 123602 (2021), URL <https://link.aps.org/doi/10.1103/PhysRevLett.127.123602>
- [90] P. Solano, P. Barberis-Blostein, F. K. Fatemi, L. A. Orozco and S. L. Rolston, “Super-radiance reveals infinite-range dipole interactions through a nanofiber”, *Nat. Commun.*, **8**, 1 (2017), URL <https://doi.org/10.1038/s41467-017-01994-3>
- [91] R. Pennetta, D. Lechner, M. Blaha, A. Rauschenbeutel, P. Schneeweiss and J. Volz, “Observation of coherent coupling between super- and subradiant states of an ensemble of cold atoms collectively coupled to a single propagating optical mode”, *arXiv preprint arXiv:2112.10806* (2021), URL <https://doi.org/10.48550/arXiv.2112.10806>
- [92] R. Pennetta, M. Blaha, A. Johnson, D. Lechner, P. Schneeweiss, J. Volz and A. Rauschenbeutel, “Collective Radiative Dynamics of an Ensemble of Cold Atoms Coupled to an Optical Waveguide”, *Phys. Rev. Lett.*, **128**, 073601 (2022), URL <https://link.aps.org/doi/10.1103/PhysRevLett.128.073601>
- [93] M. Mansuripur, “The Faraday effect”, *Opt. Photonics News*, **10**, 32 (1999), URL <https://doi.org/10.1364/OPN.10.11.000032>

-
- [94] B. E. Saleh and M. C. Teich, *Fundamentals of photonics*, JWS (2019), URL <https://doi.org/10.1002/0471213748>
- [95] D. L. Sounas and A. Alù, “Non-reciprocal photonics based on time modulation”, *Nat. Photon.*, **11**, 774 (2017), URL <https://doi.org/10.1038/s41566-017-0051-x>
- [96] S. Fan, Y. Shi and Q. Lin, “Nonreciprocal photonics without magneto-optics”, *IEEE Antennas Wirel. Propag. Lett.*, **17**, 1948 (2018), URL <https://doi.org/10.1109/LAWP.2018.2856258>
- [97] J. B. Khurgin, “Non-reciprocal propagation versus non-reciprocal control”, *Nat. Photon.*, **14**, 711 (2020), URL <https://doi.org/10.1038/s41566-020-00723-5>
- [98] E. A. Kittlaus, “Reply to ‘Non-reciprocal propagation versus non-reciprocal control’”, *Nat. Photon.*, **14**, 712 (2020), URL <https://doi.org/10.1038/s41566-020-00724-4>
- [99] A. Metelmann and A. A. Clerk, “Nonreciprocal Photon Transmission and Amplification via Reservoir Engineering”, *Phys. Rev. X*, **5**, 021025 (2015), URL <https://link.aps.org/doi/10.1103/PhysRevX.5.021025>
- [100] L. Ranzani and J. Aumentado, “Graph-based analysis of nonreciprocity in coupled-mode systems”, *New J. Phys.*, **17**, 023024 (2015), URL <http://dx.doi.org/10.1088/1367-2630/17/2/023024>
- [101] A. Metelmann and H. E. Türeci, “Nonreciprocal signal routing in an active quantum network”, *Phys. Rev. A*, **97**, 043833 (2018), URL <https://link.aps.org/doi/10.1103/PhysRevA.97.043833>
- [102] G. Lin, S. Zhang, Y. Hu, Y. Niu, J. Gong and S. Gong, “Nonreciprocal amplification with four-level hot atoms”, *Phys. Rev. Lett.*, **123**, 033902 (2019), URL <https://link.aps.org/doi/10.1103/PhysRevLett.123.033902>
- [103] H. Yang, S. Zhang, Y. Niu and S. Gong, “Ultra-strong nonreciprocal amplification with hot atoms”, *Opt. Commun.*, 128195 (2022), URL <https://doi.org/10.1016/j.optcom.2022.128195>
- [104] F. Ruesink, M.-A. Miri, A. Alu and E. Verhagen, “Nonreciprocity and magnetic-free isolation based on optomechanical interactions”, *Nat. Commun.*, **7**, 1 (2016), URL <https://doi.org/10.1038/ncomms13662>
- [105] Z. Shen, Y.-L. Zhang, Y. Chen, C.-L. Zou, Y.-F. Xiao, X.-B. Zou, F.-W. Sun, G.-C. Guo and C.-H. Dong, “Experimental realization of optomechanically induced non-reciprocity”, *Nat. Photon.*, **10**, 657 (2016), URL <https://doi.org/10.1038/nphoton.2016.161>
- [106] K. Fang, J. Luo, A. Metelmann, M. H. Matheny, F. Marquardt, A. A. Clerk and O. Painter, “Generalized non-reciprocity in an optomechanical circuit via synthetic magnetism and reservoir engineering”, *Nat. Phys.*, **13**, 465 (2017), URL <https://doi.org/10.1038/nphys4009>
- [107] Z. Shen, Y.-L. Zhang, Y. Chen, F.-W. Sun, X.-B. Zou, G.-C. Guo, C.-L. Zou and C.-H. Dong, “Reconfigurable optomechanical circulator and directional amplifier”, *Nat. Commun.*, **9**, 1 (2018), URL <https://doi.org/10.1038/s41467-018-04187-8>
- [108] N. T. Otterstrom, E. A. Kittlaus, S. Gertler, R. O. Behunin, A. L. Lentine and P. T. Rakich, “Resonantly enhanced nonreciprocal silicon Brillouin amplifier”, *Optica*, **6**, 1117 (2019), URL <https://doi.org/10.1364/OPTICA.6.001117>

BIBLIOGRAPHY

- [109] X. Zeng, P. S. J. Russell, C. Wolff, M. H. Frosz, G. K. Wong and B. Stiller, “Nonreciprocal vortex isolator by stimulated Brillouin scattering in chiral photonic crystal fibre”, *arXiv preprint arXiv:2203.03680* (2022), URL <https://doi.org/10.48550/arXiv.2203.03680>
- [110] M. Ahmadi, J. Lefebvre, W. Shi and S. LaRochelle, “Non-reciprocal sub-micron waveguide Raman amplifiers, towards loss-less silicon photonics”, *IEEE Journal of Selected Topics in Quantum Electronics*, 1–9 (2022), URL <https://doi.org/10.1109/JSTQE.2022.3195950>
- [111] M. Krause, J. Müller and E. Brinkmeyer, “Measurement of nonreciprocal stimulated Raman scattering in silicon photonic wires”, in *The 9th International Conference on Group IV Photonics (GFP)*, 6–8, IEEE (2012), URL doi.org/10.1109/GROUP4.2012.6324068
- [112] M. Lawrence and J. A. Dionne, “Nanoscale nonreciprocity via photon-spin-polarized stimulated Raman scattering”, *Nat. Commun.*, **10**, 1 (2019), URL <https://doi.org/10.1038/s41467-019-11175-z>
- [113] R. Zektzer, E. Talker, Y. Barash, N. Mazurski and U. Levy, “Chiral light–matter interactions in hot vapor-cladded waveguides”, *Optica*, **6**, 15 (2019), URL <https://doi.org/10.1364/OPTICA.6.000015>
- [114] C. Genet, “Chiral Light–Chiral Matter Interactions: an Optical Force Perspective”, *ACS Photonics* (2022), URL <https://doi.org/10.1021/acsp Photonics.1c01130>
- [115] F. L. Kien, J. Liang, K. Hakuta and V. Balykin, “Field intensity distributions and polarization orientations in a vacuum-clad subwavelength-diameter optical fiber”, *Opt. Commun.*, **242**, 445 (2004), URL <https://doi.org/10.1016/j.optcom.2004.08.0440>
- [116] P.-O. Guimond, H. Pichler, A. Rauschenbeutel and P. Zoller, “Chiral quantum optics with V-level atoms and coherent quantum feedback”, *Phys. Rev. A*, **94**, 033829 (2016), URL <https://link.aps.org/doi/10.1103/PhysRevA.94.033829>
- [117] C. Gonzalez-Ballester, E. Moreno, F. J. Garcia-Vidal and A. Gonzalez-Tudela, “Nonreciprocal few-photon routing schemes based on chiral waveguide-emitter couplings”, *Phys. Rev. A*, **94**, 063817 (2016), URL <https://doi.org/10.1103/PhysRevA.94.063817>
- [118] M.-T. Cheng, X. Ma, J.-W. Fan, J. Xu and C. Zhu, “Controllable single-photon nonreciprocal propagation between two waveguides chirally coupled to a quantum emitter”, *Opt. Lett.*, **42**, 2914 (2017), URL <https://doi.org/10.1364/OL.42.002914>
- [119] G.-Z. Song, E. Munro, W. Nie, F.-G. Deng, G.-J. Yang and L.-C. Kwek, “Photon scattering by an atomic ensemble coupled to a one-dimensional nanophotonic waveguide”, *Phys. Rev. A*, **96**, 043872 (2017), URL <https://link.aps.org/doi/10.1103/PhysRevA.96.043872>
- [120] O. Bechler, A. Borne, S. Rosenblum, G. Guendelman, O. E. Mor, M. Netser, T. Ohana, Z. Aqua, N. Drucker, R. Finkelstein *et al.*, “A passive photon–atom qubit swap operation”, *Nat. Phys.*, **14**, 996 (2018), URL <https://doi.org/10.1038/s41567-018-0241-6>
- [121] L. Du, Y.-T. Chen and Y. Li, “Nonreciprocal frequency conversion with chiral Λ -type atoms”, *arXiv preprint arXiv:2109.05449* (2021), URL <https://doi.org/10.48550/arXiv.2109.05449>
- [122] Y.-T. Chen, L. Du, L. Guo, Z. Wang, Y. Zhang, Y. Li and J.-H. Wu, “Nonreciprocal and chiral single-photon scattering for giant atoms”, *arXiv preprint arXiv:2203.00823* (2022), URL <https://doi.org/10.48550/arXiv.2203.00823>

-
- [123] M. Premaratne and G. P. Agrawal, *Light propagation in gain media: optical amplifiers*, Cambridge University Press (2011), URL <https://doi.org/10.1017/CB09780511973635>
- [124] C. M. O'Brien, "Coherent Control of Optical Processes in a Resonant Medium", Ph.D. thesis, Texas University (2011), URL <https://oaktrust.library.tamu.edu/handle/1969.1/ETD-TAMU-2011-12-10438>
- [125] M. Fleischhauer, A. Imamoglu and J. P. Marangos, "Electromagnetically induced transparency: Optics in coherent media", *Rev. Mod. Phys.*, **77**, 633 (2005), URL <https://link.aps.org/doi/10.1103/RevModPhys.77.633>
- [126] S. Scheel, S. Y. Buhmann, C. Clausen and P. Schneeweiss, "Directional spontaneous emission and lateral Casimir-Polder force on an atom close to a nanofiber", *Phys. Rev. A*, **92**, 043819 (2015), URL <https://link.aps.org/doi/10.1103/PhysRevA.92.043819>
- [127] F. Schmidt-Kaler, J. Eschner, G. Morigi, C. Roos, D. Leibfried, A. Mundt and R. Blatt, "Laser cooling with electromagnetically induced transparency: application to trapped samples of ions or neutral atoms", *Appl. Phys. B*, **73**, 807 (2001), URL <https://doi.org/10.1007/s003400100721>
- [128] E. Brion, L. H. Pedersen and K. Mølmer, "Adiabatic elimination in a lambda system", *J. Phys. A Math. Theor.*, **40**, 1033 (2007), URL <https://doi.org/10.1088/1751-8113/40/5/011>
- [129] C. Østfeldt, J.-B. S. Béguin, F. T. Pedersen, E. S. Polzik, J. H. Müller and J. Appel, "Dipole force free optical control and cooling of nanofiber trapped atoms", *Opt. Lett.*, **42**, 4315 (2017), URL <https://doi.org/10.1364/OL.42.004315>
- [130] S. B. Markussen, J. Appel, C. Østfeldt, J.-B. S. Béguin, E. S. Polzik and J. H. Müller, "Measurement and simulation of atomic motion in nanoscale optical trapping potentials", *Appl. Phys. B*, **126** (2020), URL <https://doi.org/10.1007/s00340-020-07424-5>
- [131] A. Dawes, "Undergraduate Quantum Mechanics: a Numerical Approach using QuTiP", *arXiv preprint arXiv:1909.13651* (2019), URL <https://doi.org/10.48550/arXiv.1909.13651>
- [132] G. Lindblad, "On the generators of quantum dynamical semigroups", *Commun. Math. Phys.*, **48**, 119 (1976), URL <https://doi.org/10.1007/BF01608499>
- [133] V. Gorini, A. Kossakowski and E. C. G. Sudarshan, "Completely positive dynamical semigroups of N-level systems", *J. Math. Phys.*, **17**, 821 (1976), URL <https://doi.org/10.1063/1.522979>
- [134] D. Manzano, "A short introduction to the Lindblad master equation", *AIP Adv.*, **10**, 025106 (2020), URL <https://doi.org/10.1063/1.5115323>
- [135] R. J. Johansson, P. D. Nation and F. Nori, "QuTiP 2: A Python framework for the dynamics of open quantum systems", *Comput. Phys. Commun.*, **184**, 1234 (2013), URL <http://www.sciencedirect.com/science/article/pii/S0010465512003955>
- [136] B. M. Patterson, J. F. Sell, T. Ehrenreich, M. A. Gearba, G. M. Brooke, J. Scoville and R. J. Knize, "Lifetime measurement of the cesium $6P_{3/2}$ level using ultrafast pump-probe laser pulses", *Phys. Rev. A*, **91**, 012506 (2015), URL <https://link.aps.org/doi/10.1103/PhysRevA.91.012506>
- [137] E. Vetsch, "Optical interface based on a nanofiber atom-trap", Ph.D. thesis, Mainz (2011)

BIBLIOGRAPHY

- [138] F. Warken, “Ultradünne Glasfasern als Werkzeug zur Kopplung von Licht und Materie”, Ph.D. thesis, Rheinische Friedrich-Wilhelms-Universität Bonn (2007), URL [url={https://hdl.handle.net/20.500.11811/3141}](https://hdl.handle.net/20.500.11811/3141)
- [139] F. Warken, A. Rauschenbeutel and T. Bartholomaus, “Fiber Pulling Profits from Precise Positioning-Precise motion control improves manufacturing of fiber optical resonators.” *Photonics Spectra*, **42**, 73 (2008)
- [140] Y. Meng, C. Liedl, S. Pucher, A. Rauschenbeutel and P. Schneeweiss, “Imaging and Localizing Individual Atoms Interfaced with a Nanophotonic Waveguide”, *Phys. Rev. Lett.*, **125**, 053603 (2020), URL <https://link.aps.org/doi/10.1103/PhysRevLett.125.053603>
- [141] Y. B. Ovchinnikov, S. Shul’Ga and V. Balykin, “An atomic trap based on evanescent light waves”, *J. Phys. B: At. Mol. Opt. Phys.*, **24**, 3173 (1991), URL <https://doi.org/10.1088/0953-4075/24/14/009>
- [142] J. P. Dowling and J. Gea-Banacloche, “Evanescent light-wave atom mirrors, resonators, waveguides, and traps”, *Adv. At. Mol. Opt. Phys.*, **37**, 1 (1996), URL <https://www.sciencedirect.com/science/article/pii/S1049250X08600981>
- [143] D. Hümmer, O. Romero-Isart, A. Rauschenbeutel and P. Schneeweiss, “Probing Surface-Bound Atoms with Quantum Nanophotonics”, *Phys. Rev. Lett.*, **126**, 163601 (2021), URL <https://link.aps.org/doi/10.1103/PhysRevLett.126.163601>
- [144] F. L. Kien, S. Dutta Gupta and K. Hakuta, “Phonon-mediated decay of an atom in a surface-induced potential”, *Phys. Rev. A*, **75**, 062904 (2007), URL <https://link.aps.org/doi/10.1103/PhysRevA.75.062904>
- [145] S. Buhmann, “Dispersion Forces I: Macroscopic Quantum Electrodynamics and Ground-State Casimir, Casimir-Polder and van der Waals Forces”, (2012), URL <https://doi.org/10.1007/978-3-642-32484-0>
- [146] E. Zaremba and W. Kohn, “Theory of helium adsorption on simple and noble-metal surfaces”, *Phys. Rev. B*, **15**, 1769 (1977), URL <https://link.aps.org/doi/10.1103/PhysRevB.15.1769>
- [147] A. Zangwill, *Physics at surfaces*, Cambridge university press (1988)
- [148] M.-C. Desjonqueres and D. Spanjaard, “Concepts in Surface Physics”, (2012)
- [149] N. Schlosser, G. Reymond and P. Grangier, “Collisional Blockade in Microscopic Optical Dipole Traps”, *Phys. Rev. Lett.*, **89**, 023005 (2002), URL <https://link.aps.org/doi/10.1103/PhysRevLett.89.023005>
- [150] E. Vetsch, S. T. Dawkins, R. Mitsch, D. Reitz, P. Schneeweiss and A. Rauschenbeutel, “Nanofiber-Based Optical Trapping of Cold Neutral Atoms”, *IEEE J. Sel. Top. Quantum Electron.*, **18**, 1763 (2012), URL <https://doi.org/10.1109/JSTQE.2012.2196025>
- [151] R. J. Rafac and C. E. Tanner, “Measurement of the ^{133}Cs $6p^2P_{1/2}$ state hyperfine structure”, *Phys. Rev. A*, **56**, 1027 (1997), URL <https://link.aps.org/doi/10.1103/PhysRevA.56.1027>
- [152] T. Udem, J. Reichert, R. Holzwarth and T. W. Hänsch, “Absolute Optical Frequency Measurement of the Cesium D_1 Line with a Mode-Locked Laser”, *Phys. Rev. Lett.*, **82**, 3568 (1999), URL <https://link.aps.org/doi/10.1103/PhysRevLett.82.3568>

- [153] V. Gerginov, A. Derevianko and C. E. Tanner, “Observation of the Nuclear Magnetic Octupole Moment of ^{133}Cs ”, *Phys. Rev. Lett.*, **91**, 072501 (2003), URL <https://link.aps.org/doi/10.1103/PhysRevLett.91.072501>
- [154] D. Steck, “Cesium D line data”, (2019), URL <https://steck.us/alkalidata/cesiumnumbers.pdf>
- [155] Y. Meng, A. Dureau, P. Schneeweiss and A. Rauschenbeutel, “Near-Ground-State Cooling of Atoms Optically Trapped 300 nm Away from a Hot Surface”, *Phys. Rev. X*, **8**, 031054 (2018), URL <https://link.aps.org/doi/10.1103/PhysRevX.8.031054>
- [156] M. Müller, “Realisation and Characterization of a Phase Locked Laser System for Coherent Spectroscopy of Fiber-coupled Cesium Atoms”, Master’s thesis, Johannes Gutenberg-Universität Mainz (2010), URL <https://ati.tuwien.ac.at/fileadmin/t/aqp/files/publications/diplmueller.pdf>
- [157] C. Liedl, S. Pucher, P. Schneeweiss, L. P. Yatsenko and A. Rauschenbeutel, “Observation of oscillatory Raman gain associated with two-photon Rabi oscillations of nanofiber-coupled atoms”, (2022), URL <https://doi.org/10.48550/arxiv.2207.00437>
- [158] C. F. Bohren and D. R. Huffman, *Absorption and scattering of light by small particles*, John Wiley & Sons (2008), URL <https://doi.org/10.1002/9783527618156>
- [159] S. E. Harris, J. E. Field and A. Imamoglu, “Nonlinear optical processes using electromagnetically induced transparency”, *Phys. Rev. Lett.*, **64**, 1107 (1990), URL <https://link.aps.org/doi/10.1103/PhysRevLett.64.1107>
- [160] S. H. Autler and C. H. Townes, “Stark Effect in Rapidly Varying Fields”, *Phys. Rev.*, **100**, 703 (1955), URL <https://link.aps.org/doi/10.1103/PhysRev.100.703>
- [161] U. Fano, “Effects of Configuration Interaction on Intensities and Phase Shifts”, *Phys. Rev.*, **124**, 1866 (1961), URL <https://link.aps.org/doi/10.1103/PhysRev.124.1866>
- [162] T. Y. Abi-Salloum, “Electromagnetically induced transparency and Autler-Townes splitting: Two similar but distinct phenomena in two categories of three-level atomic systems”, *Phys. Rev. A*, **81**, 053836 (2010), URL <https://link.aps.org/doi/10.1103/PhysRevA.81.053836>
- [163] P. M. Anisimov, J. P. Dowling and B. C. Sanders, “Objectively Discerning Autler-Townes Splitting from Electromagnetically Induced Transparency”, *Phys. Rev. Lett.*, **107**, 163604 (2011), URL <https://link.aps.org/doi/10.1103/PhysRevLett.107.163604>
- [164] C. Tan and G. Huang, “Crossover from electromagnetically induced transparency to Autler-Townes splitting in open ladder systems with Doppler broadening”, *J. Opt. Soc. Am. B*, **31**, 704 (2014), URL <http://josab.osa.org/abstract.cfm?URI=josab-31-4-704>
- [165] H.-C. Sun, Y.-x. Liu, H. Ian, J. Q. You, E. Il’ichev and F. Nori, “Electromagnetically induced transparency and Autler-Townes splitting in superconducting flux quantum circuits”, *Phys. Rev. A*, **89**, 063822 (2014), URL <https://link.aps.org/doi/10.1103/PhysRevA.89.063822>
- [166] L.-Y. He, T.-J. Wang, Y.-P. Gao, C. Cao and C. Wang, “Discerning electromagnetically induced transparency from Autler-Townes splitting in plasmonic waveguide and coupled resonators system”, *Opt. Express*, **23**, 23817 (2015), URL <http://www.opticsexpress.org/abstract.cfm?URI=oe-23-18-23817>

BIBLIOGRAPHY

- [167] B. Wei and S. Jian, “Objectively discriminating the optical analogy of electromagnetically induced transparency from Autler–Townes splitting in a side coupled graphene-based waveguide system”, *J. Opt.*, **19**, 115001 (2017), URL <https://doi.org/10.1088/2040-8986/aa8c56>
- [168] L. Giner, L. Veissier, B. Sparkes, A. S. Sheremet, A. Nicolas, O. S. Mishina, M. Scherman, S. Burks, I. Shomroni, D. V. Kupriyanov, P. K. Lam, E. Giacobino and J. Laurat, “Experimental investigation of the transition between Autler-Townes splitting and electromagnetically-induced-transparency models”, *Phys. Rev. A*, **87**, 013823 (2013), URL <https://link.aps.org/doi/10.1103/PhysRevA.87.013823>
- [169] C. Zhu, C. Tan and G. Huang, “Crossover from electromagnetically induced transparency to Autler-Townes splitting in open V-type molecular systems”, *Phys. Rev. A*, **87**, 043813 (2013), URL <https://link.aps.org/doi/10.1103/PhysRevA.87.043813>
- [170] B. Peng, Ş. K. Özdemir, W. Chen, F. Nori and L. Yang, “What is and what is not electromagnetically induced transparency in whispering-gallery microcavities”, *Nat. Commun.*, **5**, 1 (2014), URL <https://doi.org/10.1038/ncomms6082>
- [171] L. Xiao-Gang, M. Xing-Xu, B. Jin-Hai, Y. Yuan, W. Ling-An, F. Pan-Ming, W. Ru-Quan and Z. Zhan-Chun, “Crossover between electromagnetically induced transparency and Autler–Townes splitting with dispersion”, *Chin. Phys. B*, **24**, 094204 (2015), URL <https://doi.org/10.1088/1674-1056/24/9/094204>
- [172] X. Lu, X. Miao, J. Bai, L. Pei, M. Wang, Y. Gao, L.-A. Wu, P. Fu, R. Wang and Z. Zuo, “Transition from Autler–Townes splitting to electromagnetically induced transparency based on the dynamics of decaying dressed states”, *J. Phys. B: At. Mol. Opt. Phys.*, **48**, 055003 (2015), URL <http://doi.org/10.1088/0953-4075/48/5/055003>
- [173] H.-C. Li, G.-Q. Ge and H.-Y. Zhang, “Dressed-state realization of the transition from electromagnetically induced transparency to Autler-Townes splitting in superconducting circuits”, *Opt. Express*, **23**, 9844 (2015), URL <http://www.opticsexpress.org/abstract.cfm?URI=oe-23-8-9844>
- [174] J. Liu, H. Yang, C. Wang, K. Xu and J. Xiao, “Experimental distinction of Autler-Townes splitting from electromagnetically induced transparency using coupled mechanical oscillators system”, *Sci. Rep.*, **6**, 1 (2016), URL <https://doi.org/10.1038/srep19040>
- [175] L. Hao, Y. Jiao, Y. Xue, X. Han, S. Bai, J. Zhao and G. Raithel, “Transition from electromagnetically induced transparency to Autler–Townes splitting in cold cesium atoms”, *New J. Phys.*, **20**, 073024 (2018), URL <https://doi.org/10.1088/1367-2630/aad153>
- [176] B. C. Das, A. Das, D. Bhattacharyya, S. Chakrabarti and S. De, “Interplay between electromagnetically induced transparency (EIT), absorption (EIA), and Autler-Townes (AT) splitting in an N-type atomic system: experiment and theory”, *OSA Contin.*, **2**, 994 (2019), URL <http://www.osapublishing.org/osac/abstract.cfm?URI=osac-2-3-994>
- [177] S. K. Nath, V. Naik, A. Chakrabarti and A. Ray, “Discriminating electromagnetically induced transparency from Autler–Townes splitting in a Ξ system”, *J. Opt. Soc. Am. B*, **36**, 2610 (2019), URL <http://josab.osa.org/abstract.cfm?URI=josab-36-9-2610>

- [178] A. Rastogi, E. Saglamyurek, T. Hrushevskiy, S. Hubele and L. J. LeBlanc, “Discerning quantum memories based on electromagnetically-induced-transparency and Autler-Townes-splitting protocols”, *Phys. Rev. A*, **100**, 012314 (2019), URL <https://link.aps.org/doi/10.1103/PhysRevA.100.012314>
- [179] R. Kumar, V. Gokhroo, K. Deasy and S. N. Chormaic, “Autler-Townes splitting via frequency up-conversion at ultralow-power levels in cold ^{87}Rb atoms using an optical nanofiber”, *Phys. Rev. A*, **91**, 053842 (2015), URL <https://link.aps.org/doi/10.1103/PhysRevA.91.053842>
- [180] M. Fox, *Quantum optics: an introduction*, volume 15, OUP Oxford (2006), URL <https://global.oup.com/academic/product/quantum-optics-9780198566731>
- [181] P. van der Straten and H. Metcalf, *Atoms and Molecules Interacting with Light: Atomic Physics for the Laser Era*, Cambridge University Press (2016)
- [182] M. Bartelmann, B. Feuerbacher, T. Krüger, D. Lüst, A. Rebhan and A. Wipf, *Theoretische Physik*, Springer (2015), URL <https://doi.org/10.1007/978-3-642-54618-1>
- [183] F. Le Kien, P. Schneeweiss and A. Rauschenbeutel, “State-dependent potentials in a nanofiber-based two-color trap for cold atoms”, *Phys. Rev. A*, **88**, 033840 (2013), URL <https://link.aps.org/doi/10.1103/PhysRevA.88.033840>
- [184] W. Guerin, F. Michaud and R. Kaiser, “Mechanisms for Lasing with Cold Atoms as the Gain Medium”, *Phys. Rev. Lett.*, **101**, 093002 (2008), URL <https://link.aps.org/doi/10.1103/PhysRevLett.101.093002>
- [185] C. C. Wanjura, M. Brunelli and A. Nunnenkamp, “Topological framework for directional amplification in driven-dissipative cavity arrays”, *Nat. Commun.*, **11**, 1 (2020), URL <https://doi.org/10.1038/s41467-020-16863-9>
- [186] J. G. Hinney, “Generation of squeezed light with nanofiber-trapped atoms”, Ph.D. thesis, Wien (2019), URL <http://hdl.handle.net/20.500.12708/6561>
- [187] A. S. Prasad, “Generating correlations between photons via interaction with nanofiber-trapped atoms”, Ph.D. thesis, Wien (2020), URL <http://hdl.handle.net/20.500.12708/16281>
- [188] A. A. Clerk, M. H. Devoret, S. M. Girvin, F. Marquardt and R. J. Schoelkopf, “Introduction to quantum noise, measurement, and amplification”, *Rev. Mod. Phys.*, **82**, 1155 (2010), URL <https://link.aps.org/doi/10.1103/RevModPhys.82.1155>
- [189] X. Gu, A. F. Kockum, A. Miranowicz, Y. Liu and F. Nori, “Microwave photonics with superconducting quantum circuits”, *Phys. Rep.*, **718-719**, 1 (2017), URL <https://www.sciencedirect.com/science/article/pii/S0370157317303290>
- [190] A. Nagulu and H. Krishnaswamy, “Non-magnetic non-reciprocal microwave components—State of the art and future directions”, *IEEE Journal of Microwaves*, **1**, 447 (2021), URL <https://doi.org/10.1109/JMW.2020.3034301>
- [191] F. Le Kien, P. Schneeweiss and A. Rauschenbeutel, “Dynamical polarizability of atoms in arbitrary light fields: general theory and application to cesium”, *Eur. Phys. J. D*, **67**, 1 (2013), URL <https://doi.org/10.1140/epjd/e2013-30729-x>
- [192] D. A. Steck, “Quantum and atom optics”, Available online at <http://steck.us/teaching> (revision 0.13.10, 22 September 2021)

BIBLIOGRAPHY

- [193] Q.-Q. Hu, C. Freier, Y. Sun, B. Leykauf, V. Schkolnik, J. Yang, M. Krutzik and A. Peters, “Observation of vector and tensor light shifts in ^{87}Rb using near-resonant, stimulated Raman spectroscopy”, *Phys. Rev. A*, **97**, 013424 (2018), URL <https://link.aps.org/doi/10.1103/PhysRevA.97.013424>
- [194] D. Braak and J. Mannhart, “Fermi’s Golden Rule and the Second Law of Thermodynamics”, *Found. Phys.*, **50**, 1509 (2020), URL <https://doi.org/10.1007/s10701-020-00380-2>
- [195] S. A. M. Loos and S. H. L. Klapp, “Irreversibility, heat and information flows induced by non-reciprocal interactions”, *New J. Phys.*, **22**, 123051 (2020), URL <https://doi.org/10.1088/1367-2630/abcc1e>
- [196] J. C. d. A. Carvalho, A. D. M. de Lima and J. W. R. Tabosa, “Lasing without inversion based on magnetically assisted gain in coherently prepared cold atoms”, *Phys. Rev. A*, **105**, 023706 (2022), URL <https://link.aps.org/doi/10.1103/PhysRevA.105.023706>
- [197] L. S. Froufe-Pérez, W. Guerin, R. Carminati and R. Kaiser, “Threshold of a Random Laser with Cold Atoms”, *Phys. Rev. Lett.*, **102**, 173903 (2009), URL <https://link.aps.org/doi/10.1103/PhysRevLett.102.173903>
- [198] Q. Baudouin, N. Mercadier, V. Guarrera, W. Guerin and R. Kaiser, “A cold-atom random laser”, *Nat. Phys.*, **9**, 357 (2013), URL <https://doi.org/10.1038/nphys2614>
- [199] H. Dötsch, N. Bahlmann, O. Zhuromskyy, M. Hammer, L. Wilkens, R. Gerhardt, P. Hertel and A. F. Popkov, “Applications of magneto-optical waveguides in integrated optics: review”, *J. Opt. Soc. Am. B*, **22**, 240 (2005), URL <http://opg.optica.org/josab/abstract.cfm?URI=josab-22-1-240>
- [200] Y. Shoji and T. Mizumoto, “Magneto-optical non-reciprocal devices in silicon photonics”, *Sci. Technol. Adv. Mater.*, **15**, 014602 (2014), URL <https://doi.org/10.1088/1468-6996/15/1/014602>
- [201] L. Bi, J. Hu, P. Jiang, D. H. Kim, G. F. Dionne, L. C. Kimerling and C. Ross, “On-chip optical isolation in monolithically integrated non-reciprocal optical resonators”, *Nat. Photon.*, **5**, 758 (2011), URL <https://doi.org/10.1038/nphoton.2011.270>
- [202] W. Yan, Y. Yang, S. Liu, Y. Zhang, S. Xia, T. Kang, W. Yang, J. Qin, L. Deng and L. Bi, “Waveguide-integrated high-performance magneto-optical isolators and circulators on silicon nitride platforms”, *Optica*, **7**, 1555 (2020), URL <https://doi.org/10.1364/OPTICA.408458>
- [203] X. Qin, Y. Jiang, W. Ma, Z. Ji, W. Peng and Y. Zhao, “Observation of V-type electromagnetically induced transparency and optical switch in cold Cs atoms using nanofiber optical lattice”, *Chin. Phys. B* (2022), URL <https://doi.org/10.1088/1674-1056/ac685a>
- [204] C.-H. Yan, M. Li, X.-B. Xu, Y.-L. Zhang, H. Yuan and C.-L. Zou, “Unidirectional transmission of single photons under nonideal chiral photon-atom interactions”, *Phys. Rev. A*, **102**, 053719 (2020), URL <https://link.aps.org/doi/10.1103/PhysRevA.102.053719>
- [205] S. T. Dawkins, R. Mitsch, D. Reitz, E. Vetsch and A. Rauschenbeutel, “Dispersive Optical Interface Based on Nanofiber-Trapped Atoms”, *Phys. Rev. Lett.*, **107**, 243601 (2011), URL <https://link.aps.org/doi/10.1103/PhysRevLett.107.243601>

- [206] X. Qi, B. Q. Baragiola, P. S. Jessen and I. H. Deutsch, “Dispersive response of atoms trapped near the surface of an optical nanofiber with applications to quantum nondemolition measurement and spin squeezing”, *Phys. Rev. A*, **93**, 023817 (2016), URL <https://link.aps.org/doi/10.1103/PhysRevA.93.023817>
- [207] A. Corney, *Atomic and laser spectroscopy*, Clarendon Press Oxford (1978), URL doi.org/10.1093/acprof:oso/9780199211456.001.0001
- [208] I. I. Sobelman, *Atomic spectra and radiative transitions*, volume 12, Springer Science & Business Media (1979), URL <https://doi.org/10.1007/978-3-662-05905-0>
- [209] J. Volz, M. Scheucher, C. Junge and A. Rauschenbeutel, “Nonlinear π phase shift for single fibre-guided photons interacting with a single resonator-enhanced atom”, *Nat. Photon.*, **8**, 965 (2014), URL <https://doi.org/10.1038/nphoton.2014.253>
- [210] K. Fang, Z. Yu and S. Fan, “Photonic Aharonov-Bohm Effect Based on Dynamic Modulation”, *Phys. Rev. Lett.*, **108**, 153901 (2012), URL <https://link.aps.org/doi/10.1103/PhysRevLett.108.153901>
- [211] K. Fang, Z. Yu and S. Fan, “Experimental demonstration of a photonic Aharonov-Bohm effect at radio frequencies”, *Phys. Rev. B*, **87**, 060301 (2013), URL <https://link.aps.org/doi/10.1103/PhysRevB.87.060301>
- [212] L. D. Tzuang, K. Fang, P. Nussenzveig, S. Fan and M. Lipson, “Non-reciprocal phase shift induced by an effective magnetic flux for light”, *Nat. Photon.*, **8**, 701 (2014), URL <https://doi.org/10.1038/nphoton.2014.177>
- [213] E. Li, B. J. Eggleton, K. Fang and S. Fan, “Photonic Aharonov–Bohm effect in photon–phonon interactions”, *Nat. Commun.*, **5**, 1 (2014), URL <https://doi.org/10.1038/ncomms4225>
- [214] M. Aidelsburger, M. Atala, S. Nascimbène, S. Trotzky, Y.-A. Chen and I. Bloch, “Experimental Realization of Strong Effective Magnetic Fields in an Optical Lattice”, *Phys. Rev. Lett.*, **107**, 255301 (2011), URL <https://link.aps.org/doi/10.1103/PhysRevLett.107.255301>
- [215] L. Yuan, S. Xu and S. Fan, “Achieving nonreciprocal unidirectional single-photon quantum transport using the photonic Aharonov–Bohm effect”, *Opt. Lett.*, **40**, 5140 (2015), URL <http://www.osapublishing.org/ol/abstract.cfm?URI=ol-40-22-5140>
- [216] H. Yokoi, T. Mizumoto, T. Takano and N. Shinjo, “Demonstration of an optical isolator by use of a nonreciprocal phase shift”, *Appl. Opt.*, **38**, 7409 (1999), URL <https://doi.org/10.1364/AO.38.007409>
- [217] Z. Yu and S. Fan, “Optical isolation based on nonreciprocal phase shift induced by interband photonic transitions”, *Appl. Phys. Lett.*, **94**, 171116 (2009), URL <https://doi.org/10.1063/1.3127531>
- [218] T. Shui, W.-X. Yang, M.-T. Cheng and R.-K. Lee, “Optical nonreciprocity and nonreciprocal photonic devices with directional four-wave mixing effect”, *Opt. Express*, **30**, 6284 (2022), URL <https://doi.org/10.1364/OE.446238>
- [219] K. Fang, Z. Yu and S. Fan, “Realizing effective magnetic field for photons by controlling the phase of dynamic modulation”, *Nat. Photon.*, **6**, 782 (2012), URL <https://doi.org/10.1038/nphoton.2012.236>

BIBLIOGRAPHY

- [220] S. Mahmoodian, P. Lodahl and A. S. Sørensen, “Quantum Networks with Chiral-Light–Matter Interaction in Waveguides”, *Phys. Rev. Lett.*, **117**, 240501 (2016), URL <https://link.aps.org/doi/10.1103/PhysRevLett.117.240501>
- [221] M. Mrózek, J. Mlynarczyk, D. S. Rudnicki and W. Gawlik, “Circularly polarized microwaves for magnetic resonance study in the GHz range: Application to nitrogen-vacancy in diamonds”, *Appl. Phys. Lett.*, **107**, 013505 (2015), URL <https://doi.org/10.1063/1.4923252>
- [222] B. D. Tellegen, “The gyrator, a new electric network element”, *Philips Res. Rep.*, **3**, 81 (1948)
- [223] C. Lacroûte, K. Choi, A. Goban, D. Alton, D. Ding, N. Stern and H. Kimble, “A state-insensitive, compensated nanofiber trap”, *New Journal of Physics*, **14**, 023056 (2012), URL doi.org/10.1088/1367-2630/14/2/023056
- [224] S. Pucher, “Spectroscopy of the $6S_{1/2}$ - $5D_{5/2}$ electric quadrupole transition of atomic caesium”, Master’s thesis, Technische Universität Wien (2018), URL <http://repositum.tuwien.ac.at/obvutwhs/download/pdf/2879033>
- [225] S. Pucher, P. Schneeweiss, A. Rauschenbeutel and A. Dureau, “Lifetime measurement of the cesium $5^2D_{5/2}$ state”, *Phys. Rev. A*, **101**, 042510 (2020), URL <https://link.aps.org/doi/10.1103/PhysRevA.101.042510>
- [226] C. S. Wood, S. C. Bennett, D. Cho, B. P. Masterson, J. L. Roberts, C. E. Tanner and C. E. Wieman, “Measurement of Parity Nonconservation and an Anapole Moment in Cesium”, *Science*, **275**, 1759 (1997), URL <https://science.sciencemag.org/content/275/5307/1759>
- [227] S. G. Porsev, K. Beloy and A. Derevianko, “Precision Determination of Electroweak Coupling from Atomic Parity Violation and Implications for Particle Physics”, *Phys. Rev. Lett.*, **102**, 181601 (2009), URL <https://link.aps.org/doi/10.1103/PhysRevLett.102.181601>
- [228] B. M. Roberts, V. A. Dzuba and V. V. Flambaum, “Nuclear-spin-dependent parity nonconservation in s - $d_{5/2}$ and s - $d_{3/2}$ transitions”, *Phys. Rev. A*, **89**, 012502 (2014), URL <https://link.aps.org/doi/10.1103/PhysRevA.89.012502>
- [229] J. F. Sell, B. M. Patterson, T. Ehrenreich, G. Brooke, J. Scoville and R. J. Knize, “Lifetime measurement of the cesium $6P_{3/2}$ state using ultrafast laser-pulse excitation and ionization”, *Phys. Rev. A*, **84**, 010501 (2011), URL <https://link.aps.org/doi/10.1103/PhysRevA.84.010501>
- [230] G. Toh, J. A. Jaramillo-Villegas, N. Glotzbach, J. Quirk, I. C. Stevenson, J. Choi, A. M. Weiner and D. S. Elliott, “Measurement of the lifetime of the $7s^2S_{1/2}$ state in atomic cesium using asynchronous gated detection”, *Phys. Rev. A*, **97**, 052507 (2018), URL <https://link.aps.org/doi/10.1103/PhysRevA.97.052507>
- [231] G. Toh, N. Chalus, A. Burgess, A. Damitz, P. Imany, D. E. Leaird, A. M. Weiner, C. E. Tanner and D. S. Elliott, “Measurement of the lifetimes of the $7p^2P_{3/2}$ and $7p^2P_{1/2}$ states of atomic cesium”, *Phys. Rev. A*, **100**, 052507 (2019), URL <https://link.aps.org/doi/10.1103/PhysRevA.100.052507>
- [232] J. M. Grossman, R. P. Flliller, L. A. Orozco, M. R. Pearson and G. D. Sprouse, “Lifetime measurements of the $7D$ levels of atomic francium”, *Phys. Rev. A*, **62**, 062502 (2000), URL <https://link.aps.org/doi/10.1103/PhysRevA.62.062502>

-
- [233] J. Marek, “Study of the time-resolved fluorescence of the Cs-Xe molecular bands”, *J. Phys. B: At. Mol. Phys.*, **10**, L325 (1977), URL <https://doi.org/10.1088%2F0022-3700%2F10%2F9%2F001>
- [234] M. A. Bouchiat, J. Guéna, P. Jacquier and M. Lintz, “Measurement of the radiative lifetime of the cesium $5d^2D_{5/2}$ level using pulsed excitation and delayed probe absorption”, *Z. Phys. D*, **24**, 335 (1992), URL <https://link.springer.com/article/10.1007/BF01426680>
- [235] A. Sasso, W. Demtröder, T. Colbert, C. Wang, E. Ehrlacher and J. Huennekens, “Radiative lifetimes, collisional mixing, and quenching of the cesium 5DJ levels”, *Phys. Rev. A*, **45**, 1670 (1992), URL <https://link.aps.org/doi/10.1103/PhysRevA.45.1670>
- [236] B. Hoeling, J. R. Yeh, T. Takekoshi and R. J. Knize, “Measurement of the lifetime of the atomic cesium $5^2D_{5/2}$ state with diode-laser excitation”, *Opt. Lett.*, **21**, 74 (1996), URL <https://www.osapublishing.org/abstract.cfm?uri=ol-21-1-74>
- [237] D. DiBerardino, C. E. Tanner and A. Sieradzan, “Lifetime measurements of cesium $5d^2D_{5/2,3/2}$ and $11s^2S_{1/2}$ states using pulsed-laser excitation”, *Phys. Rev. A*, **57**, 4204 (1998), URL <https://link.aps.org/doi/10.1103/PhysRevA.57.4204>
- [238] O. S. Heavens, “Radiative Transition Probabilities of the Lower Excited States of the Alkali Metals”, *J. Opt. Soc. Am.*, **51**, 1058 (1961), URL <https://www.osapublishing.org/josa/abstract.cfm?uri=josa-51-10-1058>
- [239] P. M. Stone, “Cesium Oscillator Strengths”, *Phys. Rev.*, **127**, 1151 (1962), URL <https://link.aps.org/doi/10.1103/PhysRev.127.1151>
- [240] B. Warner, “Atomic Oscillator Strengths—III. Alkali-Like Spectra”, *Mon. Not. R. Astron. Soc.*, **139**, 115 (1968), URL <https://academic.oup.com/mnras/article/139/1/115/2601492>
- [241] M. Fabry, “Theoretical and experimental determinations of cesium oscillator strengths”, *J. Quant. Spectrosc. Radiat. Transf.*, **16**, 127 (1976), URL <http://www.sciencedirect.com/science/article/pii/0022407376900935>
- [242] C. E. Theodosiou, “Lifetimes of alkali-metal—atom Rydberg states”, *Phys. Rev. A*, **30**, 2881 (1984), URL <https://link.aps.org/doi/10.1103/PhysRevA.30.2881>
- [243] M. S. Safronova and C. W. Clark, “Inconsistencies between lifetime and polarizability measurements in Cs”, *Phys. Rev. A*, **69**, 040501 (2004), URL <https://link.aps.org/doi/10.1103/PhysRevA.69.040501>
- [244] B. K. Sahoo, “Conforming the measured lifetimes of the $5d^2D_{3/2,5/2}$ states in Cs with theory”, *Phys. Rev. A*, **93**, 022503 (2016), URL <https://link.aps.org/doi/10.1103/PhysRevA.93.022503>
- [245] M. S. Safronova, U. I. Safronova and C. W. Clark, “Magic wavelengths, matrix elements, polarizabilities, and lifetimes of Cs”, *Phys. Rev. A*, **94**, 012505 (2016), URL <https://link.aps.org/doi/10.1103/PhysRevA.94.012505>
- [246] C. E. Tanner and C. Wieman, “Precision measurement of the Stark shift in the $6S_{1/2} \rightarrow 6P_{3/2}$ cesium transition using a frequency-stabilized laser diode”, *Phys. Rev. A*, **38**, 162 (1988), URL <https://link.aps.org/doi/10.1103/PhysRevA.38.162>
- [247] D. O’Connor, *Time-correlated single photon counting*, Academic Press (2012)

BIBLIOGRAPHY

- [248] K. B. S. Eriksson and I. Wenåker, “New Wavelength Measurements in Cs I”, *Phys. Scr.*, **1**, 21 (1970), URL <https://doi.org/10.1088%2F0031-8949%2F1%2F1%2F003>
- [249] S. Tojo, T. Fujimoto and M. Hasuo, “Precision measurement of the oscillator strength of the cesium $6^2S_{1/2} \rightarrow 5^2D_{5/2}$ electric quadrupole transition in propagating and evanescent wave fields”, *Phys. Rev. A*, **71**, 012507 (2005), URL <https://link.aps.org/doi/10.1103/PhysRevA.71.012507>
- [250] C. J. Sansonetti and K. L. Andrew, “Spectrum and energy levels of singly ionized cesium: I. Revision and extension of the Cs II energy levels”, *J. Opt. Soc. Am. B*, **3**, 386 (1986), URL <http://josab.osa.org/abstract.cfm?URI=josab-3-3-386>
- [251] F. Le Kien, T. Ray, T. Nieddu, T. Busch and S. Nic Chormaic, “Enhancement of the quadrupole interaction of an atom with the guided light of an ultrathin optical fiber”, *Phys. Rev. A*, **97**, 013821 (2018), URL <https://link.aps.org/doi/10.1103/PhysRevA.97.013821>
- [252] T. Chanelière, D. N. Matsukevich, S. D. Jenkins, T. A. B. Kennedy, M. S. Chapman and A. Kuzmich, “Quantum Telecommunication Based on Atomic Cascade Transitions”, *Phys. Rev. Lett.*, **96**, 093604 (2006), URL <https://link.aps.org/doi/10.1103/PhysRevLett.96.093604>
- [253] R. Roy, P. C. Condylis, Y. J. Johnathan and B. Hessmo, “Atomic frequency reference at 1033 nm for ytterbium (Yb)-doped fiber lasers and applications exploiting a rubidium (Rb) $5S_{1/2}$ to $4D_{5/2}$ one-colour two-photon transition”, *Opt. Express*, **25**, 7960 (2017), URL <http://www.opticsexpress.org/abstract.cfm?URI=oe-25-7-7960>
- [254] E. A. Chan, S. A. Aljunid, N. I. Zheludev, D. Wilkowski and M. Ducloy, “Doppler-free approach to optical pumping dynamics in the $6S_{1/2}$ - $5D_{5/2}$ electric quadrupole transition of cesium vapor”, *Opt. Lett.*, **41**, 2005 (2016), URL <http://ol.osa.org/abstract.cfm?URI=ol-41-9-2005>
- [255] W.-M. Yao, C. Amsler, D. Asner, R. Barnett, J. Beringer, P. Burchat, C. Carone, C. Caso, O. Dahl, G. D’Ambrosio *et al.*, “Review of Particle Physics”, *J. Phys. G: Nucl. Part. Phys.*, **33**, 1 (2006), URL <https://doi.org/10.1088%2F0954-3899%2F33%2F1%2F001>
- [256] W. Demtröder, *Laser Spectroscopy 1: Basic Principles*, Springer (2014), URL <https://doi.org/10.1007/978-3-642-53859-9>
- [257] C. Alcock, V. Itkin and M. Horrigan, “Vapour pressure equations for the metallic elements: 298–2500K”, *Can. Metall. Q.*, **23**, 309 (1984), URL <https://doi.org/10.1179/cmq.1984.23.3.309>
- [258] D. G. Fletcher and J. C. McDaniel, “Collisional shift and broadening of iodine spectral lines in air near 543 nm”, *J. Quant. Spectrosc. Radiat. Transf.*, **54**, 837 (1995), URL <http://www.sciencedirect.com/science/article/pii/002240739500105T>
- [259] A. Dareau, M. Scholl, Q. Beauvils, D. Döring, J. Beugnon and F. Gerbier, “Doppler spectroscopy of an ytterbium Bose-Einstein condensate on the clock transition”, *Phys. Rev. A*, **91**, 023626 (2015), URL <https://link.aps.org/doi/10.1103/PhysRevA.91.023626>
- [260] M. C. Heaven, W. Rawlins, G. P. Perram, S. J. Davis, K. L. Galbally-Kinney, A. Hoskinson and J. Hopwood, “Diode Pumped Rare-Gas Lasers”, Technical report, EMORY UNIVERSITY Atlanta United States (2017), URL <https://apps.dtic.mil/sti/pdfs/AD1096889.pdf>
- [261] S. Pucher, P. Schneeweiss, A. Rauschenbeutel and A. Dareau, “Precise Lifetime Measurement of the Cesium $5^2D_{5/2}$ State”, *Zenodo*, DOI: 10.5281/zenodo.3701332 (2020), URL <https://doi.org/10.5281/zenodo.3701332>

- [262] T. Ray, R. K. Gupta, V. Gokhroo, J. L. Everett, T. Nieddu, K. S. Rajasree and S. N. Chormaic, “Observation of the ^{87}Rb $5S_{1/2}$ to $4D_{3/2}$ electric quadrupole transition at 516.6 nm mediated via an optical nanofibre”, *New J. Phys.*, **22**, 062001 (2020), URL <https://doi.org/10.1088/1367-2630/ab8265>
- [263] M. Bajcsy, S. Hofferberth, V. Balic, T. Peyronel, M. Hafezi, A. S. Zibrov, V. Vuletic and M. D. Lukin, “Efficient All-Optical Switching Using Slow Light within a Hollow Fiber”, *Phys. Rev. Lett.*, **102**, 203902 (2009), URL <https://link.aps.org/doi/10.1103/PhysRevLett.102.203902>
- [264] G. Morigi, J. Eschner and C. H. Keitel, “Ground State Laser Cooling Using Electromagnetically Induced Transparency”, *Phys. Rev. Lett.*, **85**, 4458 (2000), URL <https://link.aps.org/doi/10.1103/PhysRevLett.85.4458>
- [265] J. Peatross and M. Ware, “Physics of Light and Optics”, (2015), URL <https://optics.byu.edu/docs/opticsbook.pdf>
- [266] F. Le Kien, A. Rauschenbeutel, P. Schneeweiss and J. Volz, “FUNDAMENTALS OF QUANTUM OPTICS: Interaction of light with atoms, Lecture notes for the fall semester of 2013”, (2013)
- [267] V. Weisskopf and E. Wigner, “Berechnung der natürlichen Linienbreite auf Grund der Diracschen Lichttheorie”, *Zeitschrift für Physik*, **63**, 54 (1930), URL <https://doi.org/10.1007/BF01336768>
- [268] A. Einstein, “Zur Quantentheorie der Strahlung”, *Phys. Z.*, **18**, 121 (1917)
- [269] D. A. Steck, “Quantum and atom optics”, (2007), URL <http://atomoptics.uoregon.edu/~dsteck/teaching/quantum-optics/>
- [270] E. Gomez, S. Aubin, L. Orozco and G. Sprouse, “Lifetime and hyperfine splitting measurements on the 7s and 6p levels in rubidium”, *J. Opt. Soc. Am. B*, **21**, 2058 (2004), URL <http://josab.osa.org/abstract.cfm?URI=josab-21-11-2058>
- [271] E. Gomez, F. Baumer, A. D. Lange, G. D. Sprouse and L. A. Orozco, “Lifetime measurement of the 6s level of rubidium”, *Phys. Rev. A*, **72**, 012502 (2005), URL <https://link.aps.org/doi/10.1103/PhysRevA.72.012502>
- [272] I. V. Hertel and C.-P. Schulz, *Atome, Moleküle und optische Physik 1: Atome und Grundlagen ihrer Spektroskopie*, Springer Spektrum (2017), URL <https://link.springer.com/book/10.1007/978-3-662-53104-4>
- [273] T. Holstein, “Imprisonment of Resonance Radiation in Gases”, *Phys. Rev.*, **72**, 1212 (1947), URL <https://link.aps.org/doi/10.1103/PhysRev.72.1212>
- [274] T. Holstein, “Imprisonment of Resonance Radiation in Gases. II”, *Phys. Rev.*, **83**, 1159 (1951), URL <https://link.aps.org/doi/10.1103/PhysRev.83.1159>
- [275] A. F. Molisch, B. P. Oehry, W. Schupita and G. Magerl, “Radiation-trapping in cylindrical and spherical geometries”, *J. Quant. Spectrosc. Radiat. Transf.*, **49**, 361 (1993), URL <https://linkinghub.elsevier.com/retrieve/pii/002240739390100V>
- [276] C. van Tright, “Analytically solvable problems in radiative transfer. IV”, *Phys. Rev. A*, **13**, 726 (1976), URL <https://link.aps.org/doi/10.1103/PhysRevA.13.726>
- [277] W. Demtröder, *Laser Spectroscopy 2: Experimental Techniques*, Springer (2015), URL <https://doi.org/10.1007/978-3-662-44641-6>

BIBLIOGRAPHY

- [278] M. P. Silverman, S. Haroche and M. Gross, “General theory of laser-induced quantum beats. I. Saturation effects of single laser excitation”, *Phys. Rev. A*, **18**, 1507 (1978), URL <https://link.aps.org/doi/10.1103/PhysRevA.18.1507>
- [279] “The Evolution of Data to Life-Critical”, *An IDC White Paper* (2017), URL <https://www.import.io/wp-content/uploads/2017/04/Seagate-WP-DataAge2025-March-2017.pdf>, last accessed on 2021-05-19
- [280] B. Aronson, “Improving Online Access to Medical Information for Low-Income Countries”, *N. Engl. J. Med.*, **350**, 966 (2004), URL <https://doi.org/10.1056/NEJMp048009>
- [281] J. Schmitt and et.al., “Paywall: The Business of Scholarship”, (2018), URL <https://paywallthemovie.com/paywall>, online; accessed 19 June 2021
- [282] M. D. Wilkinson, M. Dumontier, I. J. Aalbersberg, G. Appleton, M. Axton, A. Baak, N. Blomberg, J.-W. Boiten, L. B. da Silva Santos, P. E. Bourne *et al.*, “The FAIR Guiding Principles for scientific data management and stewardship”, *Sci. data*, **3** (2016), URL <https://doi.org/10.1038/sdata.2016.18>
- [283] S. Pucher, P. Schneeweiss, A. Rauschenbeutel and A. Dareau, “Precise Lifetime Measurement of the Cesium $5^2D_{5/2}$ State”, *arXiv preprint arXiv:1912.10089* (2019), URL <https://arxiv.org/abs/1912.10089>

Acknowledgements

I want to thank all people that supported and encouraged me in past years during the challenging task of pursuing my PhD. Without your support, this work would not have been possible.

First and foremost, I would like to thank Arno Rauschenbeutel, who gave me the opportunity to conduct my dissertation in his research group. I had many exciting discussions with him, in which his understanding of physics always impressed me. I especially remember the many hours of creative writing in which I learned so much. I am also deeply grateful to my direct supervisor Philipp Schneeweiss, who not only convinced me to do a PhD, but also taught me so much. He was always there for me with advice and support, no matter how simple or complicated the problem was or whether he was busy himself.

I would also like to thank my colleagues at the ©Old Atoms experiment. First of all, I would like to thank Yijian Meng, who introduced me to the setup and taught me a lot. Then, I was very lucky that Christian Liedl joined our team. I cannot imagine how I would have moved the lab without him from Vienna to Berlin. I especially appreciate his quick understanding and hard work, which resulted in a very productive and enjoyable time. In the last year, also Felix Tebbenjohanns joined us and brought a lot of new knowledge and an exciting atmosphere to our team. I am also very thankful to Alexandre Dareau. Without his tips at the beginning of my PhD, I would have never been so fast. Also, I am very happy that we managed to publish a paper on our lifetime results.

Thanks also to all the other group members, many of whom I have come to appreciate not only as colleagues but also as close friends. The excellent group atmosphere made the time in Vienna as well as in Berlin one I will always remember with pleasure. I have enjoyed the many hours of discussions and appreciate the unsolicited support from all group members. Especially I will miss our coffee and cake breaks.

I would also like to say a special thank you to my family and friends. I cannot thank Andrea enough for her constant support, understanding, and encouragement during the

BIBLIOGRAPHY

last years. Last but not least, I would like to thank my parents, who always believed in me and made my studies possible through their support over the years.

Selbstständigkeitserklärung

Hiermit erkläre ich, die Dissertation selbstständig und nur unter Verwendung der angegebenen Hilfen und Hilfsmittel angefertigt zu haben. Ich habe mich nicht anderwärts um einen Doktorgrad in dem Promotionsfach beworben und besitze keinen entsprechenden Doktorgrad. Die Promotionsordnung der Mathematisch-Naturwissenschaftlichen Fakultät, veröffentlicht im Amtlichen Mitteilungsblatt der Humboldt-Universität zu Berlin Nr. 42 am 11. Juli 2018, habe ich zur Kenntnis genommen.